Universität Stuttgart

# Simulation Studies on Electrodes and Electrolytes for Electric Double Layer Capacitors

Von der Fakultät für Mathematik und Physik der Universität Stuttgart
zur Erlangung der Würde eines Doktors der Naturwissenschaften (Dr. rer. nat.)
genehmigte Abhandlung

Vorgelegt von

Konrad Breitsprecher

aus Tübingen

| | |
|---|---|
| **Hauptberichter:** | Prof. Dr. Christian Holm |
| **Mitberichter:** | Prof. Dr. Johannes Kästner |
| | Prof. Dr. Mathieu Salanne |

Tag der mündlichen Prüfung: 20.12.2018

Institut für Computerphysik der Universität Stuttgart

2018

# Contents

# 1 Summary

In this dissertation, different capacitor systems are investigated by means of computer simulations, partly accompanied by results of collaborative projects. The target systems in this work are Electric Double Layer Capacitors, meant for energy storage applications and complementing current battery technology. The transition from a circuit device with capacitance values in the range of pico- to microfarads to applicable charge storage devices with hundreds of farads requires the use of advanced electrode and electrolyte materials. This motivates a simulation approach, as the involved physical processes are governed by the dynamics of highly confined molecules in conducting materials, which are difficult to describe analytically or to capture with experimental techniques. Molecular dynamics simulations are a great tool for such problems and can also be used as a digital microscope able to track the motion of atoms in full detail. However, the quality of the results obtained by these numerical solvers depends on how well the involved force fields and algorithms can model the underlying physical system. Further, the ability to actually propagate the systems in relevant time- and length scales depends on the computational efficiency of the methods used. Thus, parts of the effort in this PhD project enters as development, optimization and testing of methods used to carry out the actual research. The software behind that is ESPResSo– an “Extensible Simulation Package for Research on Soft Matter”. ESPResSo is mostly developed and maintained among the staff of the Institute for Computational Physics. Integrating the developmental work into the open source software project has the advantage that all progress is conserved for future users.

The basic aim of the simulation studies presented here is to contribute towards a better understanding of the interplay of carbon electrodes in various geometries with ionic

liquid-based electrolytes. A large focus lies on electrode modeling with an applied external voltage and the correct treatment of boundary conditions. How these models and underlying methods affect the behavior of electrolyte molecules at the solid-liquid interface as well as the performance of the systems as energy storage devices is a central question of this study.

In Chapter 3, a brief introduction on supercapacitor technology is given. This is followed by an overview of relevant theoretical concepts in Chapter 4. The simulations are realized with different levels of detail, starting with a simple parallel plate capacitor with graphene electrodes. This system is treated in Chapter 5, which focuses on two ways of simulating metallic boundaries: In the constant charge approach, the electrodes are equipped with a fixed amount of surface charges that represent the final charged state of the capacitor. In contrast to that, the constant potential approach is only given a target potential difference and the surface charges adapt to fulfill the boundary conditions for the entirety of system charges. We verify the hypothesis that both methods result in the same average surface charge and that equal results should be obtained for static observables. Additionally, Chapter 5 investigates the impact of an atomically structured versus a computationally less expensive, smooth surface. A laterally averaged interaction potential representing a graphene surface is developed and the differences of the two electrode models on the interfacial liquid structure is presented in detail.

Capacitor systems with nanoporous carbide-derived carbon electrodes and various IL-solvent mixtures are investigated in Chapter 6. The project was initiated during a research semester at the “Maison de la Simulation” in Saclay (Paris). It was a collaboration with the CIRIMAT Laboratory, Toulouse, who provided the experimental data for the interdisciplinary study. The electrolyte is gradually switched from a pure ionic liquid to a conventional organic electrolyte solution. The simulation results are in qualitative agreement with the accompanying electrochemical measurements of the same electrolyte species, concentrations and electrodes. The central result of both simula-

tions and cyclic voltammetry experiments is that the capacitance is not significantly affected by the solvent concentration. On the other hand, diffusion measurements inside the pores show that the transport dynamics of the electrolyte is drastically increased upon partial solvation. This suggests that low concentration of ionic liquids perform better in terms of charging time and show no disadvantage in the capacitance. However, diluted ionic liquids may have smaller operating voltage windows, so that an optimal electrolyte composition is a trade-off between power- and energy density.

A third electrode model treated in Chapters 7, 8 and 9 represents a abstracted, terminated slit-like nanopore with a U-shaped cross section. The simulation setup is such that the geometry parameters of the electrode can be easily adjusted, mainly used to vary the size and length of the pore. The actual electrode boundary in the simulations is made up of particles whose charge can fluctuate. The underlying charge induction algorithm allows to specify the dielectric discontinuity such that the electrodes accurately represent a conducting surrounding. With the superposition of an electric field that can be rescaled at simulation runtime, it is possible to study the effects of a time-dependent applied voltage. This setup is introduced and tested in detail in Chapter 7. A parameter sweep of the pore size, ranging from narrow pores barely accessible for the model electrolyte to large, open pores, results in an oscillating capacitance. A global maximum in capacitance is found if the pore size matches the size of the ions, which is explained by facilitated charge accumulation due to screened electrostatics for strongly confined charges in a metallic slit. Another interesting result presented in Chapter 7 is the wetting behavior of the pores depending on the permittivity and concentration of the model electrolyte.

In Chapter 8, the same slitpore setup is used and compared to Monte Carlo simulations of an infinite metallic slit. This project was a collaboration with Dr. Svyatoslav Kondrat to study the effects of finite pore size in electric double layer capacitors. A large effort went into matching and verification of the different simulation methods. The treatment of the boundary conditions based on charge induction in the molecular

dynamics simulations and the analytically derived electrostatic interactions used in the Monte Carlo scheme showed perfect agreement. Overall, the two approaches are qualitatively consistent with each other and predict similar charging behavior: The charging mechanism starts with co-ion desorption until only counterions are left in the pores. Subsequently, counterion adsorption follows and gets more and more hindered as the pore becomes fully packed. Although filling up the pores leads to noticeable density changes in the finite reservoir of the molecular dynamics simulations, this has no effect on the charging behavior, which is confirmed by maintaining the reservoir density during charging. Although the charging behavior is equal in both simulations methods, it is found that the pore entrance and closing have a strong influence on the ion density profile along the pore, whereas the density parallel to the pore is sensitive on the wall-ion force field.

Finally, in Chapter 9 the dynamical charging and discharging behavior in the slit-pore setup and the effects of different voltage protocols are discussed. For the most part, a sudden, step-like activation is compared to a linearly increasing voltage ramp. It is found that the time behavior of the step-voltage charging consists of four distinct regimes, which include a potential-driven linear regime, a square-root diffusive regime and two exponential regimes. Further, if the applied voltage is switched on in a step-like fashion, the simulations reveal the transient formation of a crowded and dilute electrolyte phase inside the pores. In this out-of-equilibrium state, parts of the co-ions can be trapped in the rear part of the pore, blocked by the crowded phase of counterions, leading to correspondingly slow charging. It is shown that this co-ion trapping can be prevented by applying a slow voltage sweep. In doing so, the overall charging process is accelerated considerably when an appropriate sweep rate is chosen. A series of simulations having pores of different length unveils the scaling law of the optimal sweep rate which allows to estimate the charging behavior of macroscopic pores. In contrast to the charging time, it is found that discharging cannot be accelerated by a linearly decreasing voltage, but is fastest when the voltage is switched off abruptly. Again, the

dependence of the discharge time on the pore length is studied. Based on these findings, strategies for optimal charge-discharge cycles are proposed that could be applied to more reliable capacitance measurements in cyclic voltammetry experiments.

# 2 Zusammenfassung

In dieser Dissertation werden verschiedene Kondensatormodelle mittels Computersimulationen untersucht. Zudem fließen Ergebnisse zweier Kooperationsprojekte mit ein, die im Rahmen der Doktorarbeit durchgeführt wurden. Die vorliegenden Systeme gehören zur Klasse elektrischer Doppelschichtkondensatoren, die unter anderem für Energiespeicheranwendungen verwendet werden. Der Ladevorgang und die Eigenschaften dieser Systeme grenzen sich von elektrochemischen Akkumulatoren ab und können als komplementär zu aktuellen Batterietechnologien betrachtet werden. Die Energiespeicherung in diesen sogenannten Superkondensatoren basiert in erster Linie nicht auf Ladungstransfer vom beteiligten Elektrolyt auf die Elektroden, sondern beruht auf Umstrukturierung der Ladungsträger im Elektrolyt an der Grenzschicht zur Elektrodenoberfläche. Dieser Prozess kann sehr schnell ablaufen und ist reversibel, daher sind Doppelschichtkondensatoren für Anwendungen geeignet, in denen große Energiemengen innerhalb kurzer Zeit gespeichert oder freigegeben werden müssen. Der Übergang von Kondensatoren als Schaltkreiselemente, die üblicherweise geringe Kapazitätswerte im Bereich von Piko- bis Mikrofarad aufweisen, zu praktisch anwendbaren Energiespeichern mit mehreren hundert Farad in vergleichbarem Volumen erfordert die Verwendung von fortschrittlichem Elektrodenmaterial und Elektrolyten.

Die beteiligten physikalischen Prozesse motivieren den Einsatz von numerischen Simulationen: Die Dynamik von Ionen in räumlich stark eingegrenzten, hochporösen Elektrodenstrukturen ist analytisch nur schwer zu beschreiben, da sie durch die atomistischen Details und die räumliche Ausdehnung der beteiligten Ladungsträger geprägt ist. Molekulardynamik-Simulationen eigenen sich gut für solche Probleme, da sie die Trajektorien der Atome in vollem Detail verfolgen können und somit oft ein wertvolles,

anschauliches Teilchenbild zu einem gegebenen Prozess liefern. Die Qualität der Ergebnisse der numerischen Löser hängt jedoch davon ab, wie gut die beteiligten Modelle und Algorithmen die zu Grunde liegenden physikalischen Systeme zu beschreiben vermögen. Ferner müssen die Berechnungen effizient genug sein, um aussagekräftige Zeit- und Längenskalen erreichen zu können. In einem nicht zu vernachlässigenden Teil dieser Arbeit floss also auch die Entwicklung, Optimierung und Verifizierung der verwendeten Methoden ein. Die hierzu verwendete Software ist ESPResSo; das Akronym steht für „Extensible Simulation Package for Research on Soft Matter“.
ESPResSo wird hauptsächlich innerhalb einer Arbeitsgruppe des Instituts für Computerphysik verwaltet und entwickelt. Die Integration der Entwicklungsarbeit in das Open-Source-Projekt hat den Vorteil, dass alle Fortschritte für zukünftige Nutzer erhalten werden.

Das grundlegende Ziel der hier vorgestellten Simulationsstudien ist es, ein besseres Verständnis über Grenzflächeneffekte von Elektrode und Elektrolyt zu erhalten. Dabei werden hauptsächlich Kohlenstoffelektroden in verschiedenen Ausprägungen und auf ionischen Flüssigkeiten basierende Elektrolyte betrachtet. Ein weiterer Fokus liegt auf Algorithmen zur Simulation von Elektroden mit angelegter externer Spannung und der korrekten Behandlung der Randbedingungen.

Kapitel 3 stellt Superkondensatoren und deren Anwendungen als Energiespeicher der Zukunft vor, Kapitel 4 erläutert für die vorliegende Arbeit relevante, theoretische Konzepte. In den folgenden Kapiteln werden Simulationen mit unterschiedlichem Detailgrad und verschiedener Komplexität der Elektroden behandelt. Die geometrisch einfachsten Modelle dieser Arbeit stellen Kondensatoren mit planaren Graphenelektroden dar. Diese Systeme werden in Kapitel 5 diskutiert, das unter anderem zwei Ansätze zur Einbindung der Oberflächenladungen an der Grenzfläche berücksichtigt: Beim Ansatz konstanter Ladung werden die Elektroden schon zu Beginn der Simulation mit der endgültigen Oberflächenladung des vollständig geladenen Kondensators aufgesetzt. Der flüssige Elektrolyt strukturiert sich in der Umgebung der Elektroden um, bis sich

das entstehende Gegenfeld und das äußere Feld der Oberflächenladungen kompensiert haben. Diese Überlegung zeigt schon, dass die Dynamik dieser Umstrukturierung bei festgehaltener Oberflächenladung nicht der physikalischen Realität entsprechen kann, da in Wirklichkeit ein Teil der Oberflächenladung erst durch elektrostatische Induktion durch den Elektrolyt zustande kommt. Im Gegensatz dazu wird beim Ansatz konstanten Potentials nur die Potentialdifferenz vorgegeben – die Oberflächenladungen passen sich entsprechend an, damit die Gesamtheit der Systemladungen die vorgegebene Randbedingung erfüllt. Auch wenn sich, wie erwähnt, der Ansatz konstanter Ladung nicht für die Untersuchung des dynamischen Ladeprozesses eignet, resultieren beide Methoden bei gleicher finaler Oberflächenladung in derselben Elektrolytstruktur, was durch Simulationen mit beiden Methoden bestätigt wird. Darüber hinaus werden in Kapitel 5 die Auswirkungen der Graphenstruktur im Vergleich zu einer glatten Oberfläche untersucht. Letztere kann durch eine eindimensionale Wechselwirkung beschrieben werden und ist somit rechnerisch einfacher zu realisieren als eine Oberfläche auf Teilchenbasis. Das Wechselwirkungspotential einer dreilagigen Graphenelektrode wird durch räumliche Mittelung genähert und die Unterschiede der beiden Elektrodenmodelle auf die Flüssigkeitsstruktur im Detail untersucht.

Kapitel 6 behandelt Kondensatorsysteme mit hochporösen Kohlenstoffelektroden mit unterschiedlichen Mischungsverhältnissen von ionischer Flüssigkeit und organischem Lösungsmittel. Das interdisziplinäre Projekt wurde im Rahmen eines Forschungssemesters im ”Maison de la Simulation“ in Saclay (Paris) initiiert. Experimentelle Vergleichsdaten zu den Simulationen wurden durch eine Kooperation mit dem CIRIMAT Laboratory (Toulouse) erhalten. In der Studie wird die Kapazität des Systems für den Übergang von einer reinen ionischen Flüssigkeit zu einer verdünnten Elektrolytlösung untersucht. Die Simulationen zeigen eine qualitative Übereinstimmung zu den elektrochemischen Messungen mittels zyklischer Voltammetrie, wobei in beiden Fällen die gleiche Elektrolytzusammensetzung und Elektrodenkonfiguration verwendet wurde. Das zentrale Ergebnis von Simulation und Messung ist, dass die Kapazität nicht

wesentlich durch die Menge des Lösungsmittels beeinflusst wird. Weiterhin zeigen Messungen innerhalb des Porenvolumens, dass partielle Solvatation den Ionentransport deutlich erhöht. Dies deutet darauf hin, dass eine geeignete Verdünnung von ionischen Flüssigkeiten von Vorteil für die Ladezeiten in Superkondensatoren sein kann, ohne sich negativ auf die Menge der gespeicherten Energie auszuwirken. Allerdings kann eine Verdünnung auch die maximal mögliche Betriebsspannung reduzieren, so dass eine optimale Elektrolytzusammensetzung einen Kompromiss zwischen Leistungs- und Energiedichte darstellt.

In den Kapiteln 7, 8 und 9 wird ein drittes Elektrodenmodell untersucht. Nach den vorangegangenen, materialspezifischen Simulationen wird nun ein eher abstrahiertes Porenmodell verwendet. Elektrode und Gegenelektrode bestehen jeweils aus einer einzelnen Pore mit U-förmigen Querschnitt. Die Computersimulationen sind so gestaltet, dass einzelne Parameter der Geometrie wie Porenlänge oder Breite der Öffnung einfach variiert werden können. Die tatsächliche Elektrodenoberfläche ist aus Teilchen mit variabler elektrischer Ladung aufgebaut. Ein iterativer Algorithmus zur Berechnung der Influenzladung passt die Ladung dieser Teilchen an und realisiert so den dielektrischen Sprung von Flüssigkeit zu leitendem Material. Die Superposition mit einem elektrischen Feld, das während der Simulation reskaliert werden kann, macht es möglich, die Auswirkung einer zeitabhängigen Potentialdifferenz auf den Ladevorgang zu untersuchen. In Kapitel 7 wird das System vorgestellt und getestet. Im gleichen Kapitel wird auch der Einfluss der Porengröße untersucht. Die Variation reicht von kleinen, für den Elektrolyten kaum zugänglichen Poren bis hin zu großen, offenen Poren. Die Änderung der Geometrie resultiert in einem oszillierenden Verhalten der Kapazität. Diese zeigt ein globales Maximum, wenn die Porengröße in etwa der Größe der Ionen entspricht. Der physikalische Ursprung dieses Maximums wird dadurch erklärt, dass die effektive Paarwechselwirkung von Ladungen durch die metallische Umgebung im Vergleich zum Vakuumfall abgeschwächt wird, was die Akkumulation von gleichnamigen Ladungen erleichtert und somit die Kapazität erhöht. Ein weiteres interessantes Ergebnis

aus Kapitel 7 ist das Benetzungsverhalten der Poren in Abhängigkeit der Permittivität und Konzentration des Modellelektrolyten.

In Kapitel 8 werden die Molekulardynamik-Simulationen der finiten Schlitzpore mit Monte-Carlo-Simulationen eines periodisch fortgesetzten, folglich infiniten metallischen Schlitzes verglichen. Dieses Projekt wurde in Zusammenarbeit mit Dr. Svyatoslav Kondrat durchgeführt, der die Ergebnisse der Monte-Carlo-Berechnungen lieferte und wesentlich an der Auswertung beteiligt war. Ein großer Teil des Vergleichs beinhaltet die Verifikation der verschiedenen Simulationsmethoden. Wie erläutert, werden die Randbedingungen in den Molekulardynamik-Simulationen durch dynamische Ladungsinduktion auf der Oberfläche erfüllt. Im Gegensatz dazu kann die Elektrostatik der Ladungen in metallischer Umgebung im Modell der infiniten Pore analytisch formuliert werden. Eine Untersuchung der beiden Ansätze mittels diverser Testfälle zeigt perfekte Übereinstimmung der elektrostatischen Wechselwirkungen. Insgesamt stimmen beide Systeme qualitativ überein und führen zu ähnlichen Ionenkonfigurationen in Abhängigkeit der angelegten Spannung. Eine Untersuchung des Lademechanismus zeigt, dass dieser im Bereich kleiner Spannungen durch die Desorption der Co-Ionen geprägt ist, bis im geladenen Zustand nur noch Gegenionen in den Poren zurückbleiben. Anschließend erfolgt die Erhöhung der Porenladung durch Adsorption weiterer Gegenionen, was durch die zunehmende Dichte in der Pore behindert wird und den Ladungszuwachs bei weiterer Erhöhung der Spannung abschwächt. Das Auffüllen der Poren führt zwar in den Molekulardynamik-Simulationen zu merklichen Dichteänderungen im Reservoir, dies hat aber nur geringen Einfluss auf das Ladeverhalten, was durch erweiterte Simulationen bestätigt wird, welche die Reservoirdichte während des Ladevorgangs aufrechterhalten. Obwohl das Ladeverhalten in beiden Methoden denselben Verlauf zeigt, wirkt sich der Poreneingang und die Terminierung stark auf das Ionendichteprofil entlang der Pore aus.

Schließlich wird in Kapitel 9 das dynamische Lade- und Entladeverhalten der Schlitzpore und die Auswirkungen von verschiedenen Spannungsprotokollen diskutiert. Für

das Aufladeverhalten wird ein plötzliches, stufenartiges Anschalten der Spannung mit einer linearen Spannungsrampe verglichen. Das Zeitverhalten der Ladung innerhalb der Pore bei abrupter Spannungszufuhr kann durch vier Regime beschrieben werden: Ein zu Beginn feldgetriebenes, lineares Regime wird zunächst gefolgt von einem diffusiven Regime, an das sich dann zwei exponentielle Regime anschließen. Weiter zeigen die Simulationen, dass sich bei abrupter Spannungszufuhr zwei Phasen in den Poren ausbilden: Im Eingangsbereich der Pore sammeln sich direkt nach dem Einschalten der Spannung vermehrt Gegenionen an und die ladungsneutrale Phase im hinteren Teil der Pore wird verdichtet. Durch diesen Nichtgleichgewichtszustand können Co-Ionen im hinteren Teil eingeschlossen werden und deren Diffusion aus der Pore wird erschwert. Dieser Effekt kann zu einer drastischen Erhöhung der Ladezeit führen. Weitere Simulationen zeigen jedoch, dass der gesamte Ladeprozess erheblich beschleunigt werden kann, wenn eine lineare Spannungsrampe mit entsprechend angepasster Steigung verwendet wird. Der Zusammenhang zwischen optimaler Steigung und Porenlänge wird durch eine erweitere Simulationsreihe mit verschiedenen Porenlängen ermittelt. Dies ermöglicht eine Vorhersage der optimalen Steigung der Spannungsrampe für makroskopische Systeme. Im Gegensatz zum Aufladeprozess zeigen Simulationen zum Entladevorgang, dass dieser durch eine linear fallende Spannung nicht beschleunigt wird. Auch hier wird die Abhängigkeit der Entladedauer von der Porenlänge untersucht. Mit den Erkenntnissen über die Ladedynamik kann schließlich ein optimaler Spannungzyklus angegeben werden, der für zuverlässigere Kapazitätsmessungen mittels zyklischer Voltammetrie verwendet werden könnte.

# Publications

The following list shows the publications I authored and contibuted to in the course of my PhD project. Content of publications 1, 4, 5, 6 and 7 is reproduced in this work.

1. A. Arnold, **K. Breitsprecher**, F. Fahrenberger, S. Kesselheim, O. Lenz and C. Holm
   "Efficient Algorithms for Electrostatic Interactions Including Dielectric Contrasts"
   *Entropy*, **2013**, 15 (11), pp 4569-4588
   URL: https://doi.org/10.3390/e15114569

2. **K. Breitsprecher**, P. Košovan and Christian Holm
   "Coarse grained simulations of an ionic liquid-based capacitor I:
   density, ion size, and valency effects"
   *Journal of Physics: Condensed Matter*, **2014**, 26 (28), p 284108
   URL: http://doi.org/10.1088/0953-8984/26/28/284108

3. **K. Breitsprecher**, P. Košovan and Christian Holm
   "Coarse grained simulations of an ionic liquid-based capacitor II:
   asymmetry in ion shape and charge localization"
   *Journal of Physics: Condensed Matter*, **2014**, 26 (28), p 284114
   URL: http://doi.org/10.1088/0953-8984/26/28/284114

4. **K. Breitsprecher**, K. Szuttor and C. Holm
   "Electrode Models for Ionic Liquid-Based Capacitors"
   *The Journal of Chemical Physics C*, **2015**, 119 (39), pp 22445-22451
   URL: https://doi.org/10.1021/acs.jpcc.5b06046

5. R. Burt, **K. Breitsprecher**, B. Daffos, P. Taberna, P. Simon, G. Birkett, X. S. Zhao, C. Holm and M. Salanne
   "Capacitance of Nanoporous Carbon-Based Supercapacitors Is a Trade-Off between the Concentration and the Separability of the Ions"
   *The Journal of Physical Chemistry Letters*, **2016**, 7 (19), pp 4015–4021
   URL: https://doi.org/10.1021/acs.jpclett.6b01787
   R. Burt and K. Breitsprecher contributed equally to this work.

6. **K. Breitsprecher**, M. Abele, S. Kondrat and C. Holm
   "The effect of finite pore length on ion structure and charging"
   *The Journal of Chemical Physics*, **2017**, 147 (10), p 104708
   URL: https://doi.org/10.1063/1.4986346

7. **K. Breitsprecher**, C. Holm and S. Kondrat
   "Charge Me Slowly, I Am in a Hurry: Optimizing Charge–Discharge Cycles in Nanoporous Supercapacitors"
   *ACS Nano*, **2018**, 12 (10), pp 9733-9741
   URL: https://doi.org/10.1021/acsnano.8b04785

8. F. Weik, R. Weeber, K. Szuttor, **K. Breitsprecher**, J. de Graaf, M. Kuron, J. Landsgesell, H. Menke, D. Sean, and C. Holm
   "ESPResSo 4.0 – An Extensible Software Package for Simulating Soft Matter Systems"
   *European Physical Journal ST*, **2018**, accepted

# 3 Introduction

The optimization of devices for electric energy storage (EES) is of great interest in the transition from carbon-based fuels to electrical drive, energy recovery or rapid-charging everyday tools. Ionic liquid (IL) based capacitors belong to a class of energy storage devices with promising properties to contribute to this transition. They are known as electric double-layer capacitors (EDLCs) , supercapacitors or ultracapacitors and consist of a liquid electrolyte confined between electrodes of various geometries and materials. In EDLCs, the energy is stored by potential-induced adsorption of counter-charges on the surface of the electrodes which requests conducting, high surface area electrode materials to maximize the energy per volume. This suggests the use of electrodes with subnanometer pores, which show anomalously high capacitance vales and stored energies [1–4]. The dominant role in this field has been played by conventional batteries, mainly due to their low production costs, high energy densities and device optimization with a research background of more than a century. In recent years however, EDLCs have become increasingly popular on the EES market, finding their applications in devices that require fast energy intake or delivery. The advance of this technology was driven by extensive research on enhancing the energy density of supercapacitors [5–12]. This involves the development and synthesization of Room Temperature Ionic Liquids (RTILs) which allow high operating voltages as well as optimizing porous electrode materials that provide high specific surface areas of more than $1000\,\mathrm{m}^2\,\mathrm{g}^{-1}$.

## 3.1 Technology overview

A widely used classification states that even though supercapacitors provide excellent power densities and cyclability, the stored energies are lower compared to competing Faradaic energy storage systems [13]. Quantitative estimations report a reduced energy density of about one order of magnitude compared to batteries [14]. The reason for this lies in the fundamentally different nature of the storage principle: In batteries, the energy is stored in the bulk, whereas in EDLCs, it is based on ion rearrangement on the surface. This difference also explains why EDLCs are superior as a high power recipient and supplier. The potential-driven accumulation of charge in supercapacitors ideally involves no chemical reactions, so the charge- and discharge processes are fast and occur in seconds. For the same reason, the cycle life is remarkably long and the charging can theoretically proceed undisturbed by electrode restructuring or accumulation of secondary products. However, there is a trade-off involved concerning cycle life and stored energy: If the applied potential is outside a certain voltage window, chemical decomposition of the electrolyte takes place, possibly reducing the amount of surface area and available charge carriers. On the other hand, the energy approximately scales quadratically with the applied potential, so it is desired to operate EDLCs at the borders of their decomposition window. Related to the chemical decomposition is the occurrence of a pseudocapacitance [15]. The charge transfer in Faradaic redox processes contributes to the capacitance of the devices and is the energy storage principle of electrochemical capacitors, also called pseudocapacitors. This effect is part of the signature in cyclic voltammetry (CV) experiments, causing spikes in the electric current if a certain voltage is applied. Possible non-reversibility of these reactions also leads to hysteresis of the CV-curves. A clearly unwanted occurrence of pseudocapacitance stems from electrolysis of residual water in the electrolyte, so preferably pure, water-free RTILs are required. As opposed to this, hybrid capacitors purposely combine the effects of double-layer- and reversible pseudocapacitance.

## 3.2 Room Temperature Ionic Liquids

Ionic liquids are solvent-free molten salts with a melting point below $100\,^{\circ}\mathrm{C}$ and are used in chemical synthesis and catalysis, separation processes and as electrolytes for electrochemistry and photovoltaics. To stress the low melting point character, they are also called Room Temperature Ionic Liquids. RTILs often contain organic, large molecules with low symmetry in molecular shape and partial charge distribution. The size and asymmetry leads to packing inefficiency and a reduced melting point compared to salts with inorganic components. A typical feature of IL cations are alkylated molecular rings with delocalized charges such as imidazole or pyrrolidin. IL anions often are fluorous like $PF_6$ or $BF_4$. Halide anions are used as well, e.g. $\mathrm{HMIM}^{+}\,\mathrm{Cl}^{-}$ (1-Hexyl-3-methylimidazolium chloride), despite of the small chloride ion, melts at $-75\,^{\circ}\mathrm{C}$ [16]. Because of the diversity of possible combinations leading to the low melting point behavior, RTILs are also called 'designer solvents', referring to their usage as dissolvers in chemical processing and the possibility to tune the composition for the target application.

Another important property of ILs is the generally low volatility [17], although careful distillation is possible [18]. Briefly explained, the predominant long-range Coulombic interaction prevents evaporation and leads to low vapor pressure, which is advantageous for many applications that pose risks of contamination and environmental release. However, ILs still can be toxic [19] and the frequently used classification as 'green' solvents can be doubted, e.g. regarding the fact that specific ILs are also used to dissolve cellulose [20]. For their application as electrolytes in EDLCs, their high viscosity and low conductivity is problematic and slows down ion exchange processes in porous electrodes. In this context, mixtures of different ILs or addition of organic solvents can be beneficial [21]. Related to this work, it was found that adding acetonitrile (ACN) "[...]boosts conductivity of imidazolium ionic liquids" [22], which poses the question if the dilution of pure RTILs has a negative effect on the capacitance in

nanoporous electrodes. In Chapter 6, this is investigated with MD simulations and accompanying experiments of the IL EMIM $BF_4$ with various concentrations of ACN in realistic nanoporous electrodes. Another IL used in this work is BMIM $PF_6$ in Chapter 5 and 9, a promising electrolyte [23] with a well tested coarse-grained model [24] applied in various simulation studies [25–28].

## 3.3 Electrode materials

Primarily, the electrode material in EDLCs should provide a high surface area accessible to the liquid electrolyte to maximize the stored energy per volume. Widely used are carbon-based porous materials in various forms such as carbide-derived carbon (CDC), carbon nanotubes (CNTs) or activated carbon (AC). The latter is largely utilized in commercial EDLCs, mainly because of the low production cost based on carbonaceous, naturally-occurring source materials like wood, nutshells or peat followed by a chemical or physical activation process. CDCs are derived from carbide precursors like silicon carbide (SiC) or titanium carbide (TiC). The transformation into a pure, highly conductive and stable carbon structure can happen e.g. via chlorine treatment. In this etching process, the temperature of the chlorine gas affects the resulting pore size distribution. In the MD simulations in Chapter 6, a small scale configuration of a CDC-800 network with a chlorination temperature of $800\,^{\circ}\mathrm{C}$ is applied.
Another promising route towards optimizing supercapacitor performance uses graphene, which is a highly conductive, atomic monolayer with a hexagonal carbon pattern that can be obtained by shear exfoliation of graphite. The specific surface area of graphene is $2630\,\mathrm{m^2\,g^{-1}}$, however a space-filling structure is needed for mechanically stable electrodes [29]. Chapter 5 investigates atomically flat graphene electrodes in a supercapacitor, the impact of the honeycomb structure on the IL structure and compares algorithms used to model the metallic boundary conditions.

## 3.4 Example applications

To arouse interest, some prominent concepts for applications of supercapacitors are listed below:

- In several countries, electrically powered buses make use of the high power density by recharging supercapacitor cells during boarding and alighting of passengers at the bus stops [30]. This concept can also be extended to other public transport systems like tramways or subways [31].
- For an acceptable energy conversion efficiency, regenerative brakes need energy buffers with high current rating and cycle stability [32]. This can be realized especially well in the locomotive sector: At track sections with high slopes, supercapacitors can buffer the breaking energy of trains going downhill to supply energy for the uphill direction [33].
- The mechanical properties of carbon-based electrodes encouraged ideas of combining chassis and energy reservoir in electric vehicles [34, 35], reducing weight and increasing the range of the cars.
- A combination of solar cells, LED lamps and supercapacitors can be used for street lighting, taking advantage of the long lifetime and thermal stability of the electrolyte [36].
- Power stabilization for consumer electronics [37] with high fluctuation loads like photographic flashes can benefit from supercapacitors.
- Flexible electrodes based on composite material combining fabric and conducting materials like nanowires [38] form wearable supercapacitors [39].

# 4 Methods and theories

Many more applications are emerging that exploit the advantages of supercapacitors. Also, the is an active scientific interest in the topic, driven by the novelty of the field, the industrial demands and the huge variety of parameters of the two main ingredients: To a large amount, the details of electrode and electrolyte determine the performance of the capacitor. Novel porous electrode materials and the possibility to 'design' an appropriate electrolyte by combining various RTILs and solvents leads to many possible electrolyte candidates. Due to this variety, generalized assumptions become useful that narrow down the choice of materials. This argument also motivates investigations on less specific model systems, mean field theories and coarse grained approaches.

## 4.1 Interface theories on the differential capacitance

A fundamental first step towards understanding and optimizing EDLCs is the investigation of the basic parallel plate capacitor setup. Theories aim for solutions of the electrostatic potential and the ion concentration profiles across the system and their dependence on a imposed electrode surface charge or potential. The difficulty of the theoretical framework in these systems can be found in the nature of the electrolyte: ILs are dense ionic substances, bulk- or interfacial properties are governed by the interplay of excluded volume and the local electrical field caused by the surrounding charges. These strong ion-ion correlations lead to oscillating charge density profiles at the solid-liquid phase boundary that deviate strongly from solutions obtained by a non-expanded Poisson-Boltzmann approach. More advanced theories split the interfacial region spatially into parts that incorporate known physical effects. The famous

Stern-model for example combines previous work by Helmholtz and Gouy-Chapman. The former realized that a charged electrode causes a layer of electrostatically attracted counterions [40], the double-layer of electrode charges and ion charges behaves like a classical plate capacitor of area $A$, surface charge $Q$, Helmholtz potential drop $\Delta\varphi_H$, relative permittivity $\epsilon_H$ of the Helmholtz layer and layer thickness $d_H$, which is given by the radius of the counterions, leading to the Helmholtz capacitance $C_H$:

$$C_H = \frac{Q}{\Delta\varphi_H} = \epsilon_0 \epsilon_H \frac{A}{d_H}. \tag{4.1}$$

The complete capacitor system with two electrodes is described by connecting two Helmholtz layers with individual thicknesses in series. Similar to the theory of Debye and Hückel [41], Gouy and Chapman [42] assumed Boltzmann distributed, one dimensional ion number densities

$$n_\pm(x) = n_0 \exp\left(\frac{-q_\pm \varphi(x)}{k_\mathrm{B} T}\right). \tag{4.2}$$

with bulk density $n_0$ and ion charges $q_\pm$ and predicted a diffuse ion layer in front of a single surface with an exponential decay of the electrostatic potential [43]. Assuming electroneutrality, the surface charge $\sigma$ is equal to the total ion charge. With the boundary conditions $\varphi(0) = U$ on the surface and $\varphi(x) = \frac{d\varphi(x)}{dx} = 0$ for $x \to \infty$, Poisson's equation can be integrated once to get Gauss's law

$$\sigma = \int_0^\infty \rho(x) dx = \int_0^\infty \frac{d^2\varphi(x)}{dx^2} dx = \epsilon_0 \epsilon_r \left.\frac{d\varphi}{dx}\right|_{x=0}. \tag{4.3}$$

This gives an expression for $\sigma(U)$ which then is used to calculate the differential capacitance

$$DC(U) = \frac{d\sigma(U)}{dU}. \tag{4.4}$$

Equation 4.2 can be expanded to the system's charge density $\rho(x) = q_+ n_+ + q_- n_-$, the differential capacitance according to Gouy-Chapman is then obtained via Equations

4.3 and 4.4 to

$$DC_{\mathrm{GC}}(U) = \frac{\epsilon_0 \epsilon_r}{\lambda_D} \cosh\left(\frac{qU}{2k_B T}\right). \tag{4.5}$$

The expression includes the characteristic (Debye) length of the diffuse layer:

$$\lambda_D = \sqrt{\frac{\epsilon_0 \epsilon_r k_B T}{2q^2 n_0}}. \tag{4.6}$$

Because of the non-physical asymptotic behavior

$$\lim_{|U|\to\infty} DC_{\mathrm{GC}}(U) = \infty \tag{4.7}$$

the Gouy-Chapman model loses it's validity for high potentials. This was resolved by the idea of Stern, who combined the two results of Equations 4.1 and 4.5 by assuming a series connection of a Helmholtz- and Gouy-Chapman layer:

$$DC_{\mathrm{S}}(U) = \frac{1}{\frac{1}{C_H(U)} + \frac{1}{DC_{\mathrm{GC}}(U)}} = \frac{\epsilon_0 \epsilon_r}{d_H + \frac{\lambda_{\mathrm{D}}}{\cosh\left(\frac{xU}{2k_B T}\right)}}. \tag{4.8}$$

In the series connection, the smaller contribution dominates the overall capacitance, so the Gouy-Chapman part only contributes to the total capacitance for small potentials $U$ in eq. 4.8, which otherwise approaches the constant Helmholtz capacitance. This behavior still remains questionable, as it means that the capacitor is constantly able to accumulate charge at increasing potential, where some form of decaying differential capacitance by saturating ion layers would be expected. So the assumptions included in the derivation of Equation 4.8 leads to a limited predictive quality of the Stern model for concentrated electrolytes or ILs. The crucial approximations and problems when applying the Stern model to EDLCs are the following:

- The mean-field character of the Poisson-Boltzmann approach by Gouy-Chapman neglects the strong electrostatic ion-ion correlations.

- Treatment of the ions as point charges without excluded volume, causing theoretically infinite ion accumulation at the interface.
- Limited validity of the Debye length for high ion concentrations: A number density of $n_0 = 1\,\mathrm{nm}^{-1}$, $q = e$ and $\epsilon_r = 80$ used in Equation 4.6 leads to a value of $\lambda_D \approx 2.8\,\text{Å}$, which is smaller than a typical ion in an IL and defies the concept of a diffuse ion layer.
- Only electrostatic interactions are included in the theories, disregarding chemical properties like specific ion adsorption onto the surface.

The neglected ion size effect was included in extensions of the Gouy-Chapman model, famous examples are theories by Bikerman [44], Freise [45] and later Eigen and Wicke [46]. The common theme is to constrain the total numbers of anions $N_-$, cations $N_+$, solvent particles $N_S$ and the volume of the layer. The mean-field character of the model persists, but the occupation of the layers is now limited by a finite number of sites, which is taken into account in the entropic term in the Helmholtz free energy

$$F = e\varphi(N_+ - N_-) - k_B T \ln(\Omega) \tag{4.9}$$

with the partition function given by

$$\Omega = \frac{N!}{N_+! N_-! N_S!}. \tag{4.10}$$

Equation 4.10 can be derived by considering the number of combinations of distributing $N_+$, $N_-$ and $N_S$ on the $N$ available sites. This splitting of the interfacial layers in lattice sites each of which can only be occupied by a single particle led to the term *lattice-gas model* for this approach. The next steps towards deriving the capacitance is to calculate the electrochemical potential of the charges species

$$\mu_\pm = \frac{\partial F}{\partial N_\pm}. \tag{4.11}$$

In equilibrium, this equals the chemical potential $\mu_\infty$ in the bulk, where zero potential $\varphi_\infty = 0$ and equal number of ions $N_+^\infty = N_-^\infty = N_\infty$ are set. So using $\mu_\infty = \mu_\pm$ leads to an expression for the particle numbers $N_\pm$ of the form

$$N_\pm = N_\infty \exp\left(\frac{-q_\pm \varphi(x)}{k_\mathrm{B}T}\right) \frac{N - N_+ - N_-}{N - 2N_\infty}. \tag{4.12}$$

This expression then again can be rewritten for ion concentrations or charge densities which via Equations 4.3 and 4.4 leads to the *Freise-Bikerman* [47] differential capacitance

$$DC_\mathrm{Fr}(U) = \frac{\frac{\epsilon_0 \epsilon_r A}{\lambda_D} \sinh\left(\frac{eU}{k_B T}\right)}{2\left(1 + 4vc_\infty \sinh^2\left(\frac{eU}{2k_B T}\right)\right)} \cdot \sqrt{\frac{4vc_\infty}{\ln\left(1 + 4vc_\infty \sinh^2\left(\frac{eU}{2k_B T}\right)\right)}} \tag{4.13}$$

with bulk concentration $c_\infty$ and ion volume $v$ (equal for all species). Note that the eq. 4.13 in this form is only valid for $U >= 0$, as the $\sinh$ in the first term would lead to a negative differential capacitance for $U < 0$, but can be rewritten to provide axial symmetry for the capacitance. Compared to the *U-shaped* Gouy-Chapman capacitance in 4.5, eq. 4.13 now also has a minimum at $U = 0$ but is followed by two local maxima and decaying asymptotic behavior. Therefore it is often called *camel-shaped* capacitance and qualitatively matches results of several experiments [48] and simulations [49]. This shows that incorporating the ion volume has the deciding effect that the diffuse layer cannot infinitely accumulate charges leading to infinite capacitance. If the ion layer becomes crowded, adding more charges of the same sign is energetically and entropically unfavorable.

On a similar theoretical foundation, another well-cited publication in the field was provided by Kornyshev [50], who transferred the theory, originally intended to describe dilute electrolytes, to ionic liquids. The model now interprets the solvent particles as voids in the lattice. The derivation and expression for the capacitance is similar to

Equation 4.13 and reads as

$$DC_{\mathrm{Kor}}(U) = \frac{\frac{\epsilon_0 \epsilon_r A}{\lambda_D} \cosh\left(\frac{eU}{2k_B T}\right)}{1 + 2\gamma \sinh^2\left(\frac{eU}{2k_B T}\right)} \cdot \sqrt{\frac{2\gamma \sinh^2\left(\frac{eU}{2k_B T}\right)}{\ln\left(1 + 2\gamma \sinh^2\left(\frac{eU}{2k_B T}\right)\right)}}. \tag{4.14}$$

It provides insight about the capacitance response for different states of initial occupation of the lattice using the packing parameter

$$\gamma = \frac{2c_\infty}{c_{max}}, \tag{4.15}$$

which is the ratio of occupied sites $c_\infty$ to maximal available sites $c_{max}$. For $\gamma = 1$, all sites are initially occupied and the differential capacitance has a *bell-shape* with a single maximum at $U = 0$. In the lattice picture, this means that the saturation is already reached for $U = 0$ and further charge accumulation, which can only proceed via ion swapping, already has an entropic penalty. Taking $\gamma = 0$ means $c_{max} \to \infty$ which implies infinite available sites. Consistently, using $\gamma = 0$, Equation 4.14 transfers into the Gouy-Chapman solution (Equation 4.5). At $\gamma > 1/3$, the DC shows the already described *camel-shape* with two local maxima, which mark the points in applied potential where the saturation of the lattice leads to a decreasing capacitance for higher potentials following approximately an inverse square-root behavior $1/\sqrt{U}$. This provides a rather important conclusion for the interpretation of the differential capacitance obtained by experiments or simulations: A local maximum in the capacitance is connected to a potential induced transition in the interface layers. In the mean-field approach, the origin of this transition is due to the saturation of the lattice sites, but also other effects like potential induced molecular rotation or adaption to the surface structure can contribute to extrema in the differential capacitance [51, 25]. The superposition of several of these effects finally results in the complex shape of the differential capacitance. There are two shortcomings of the mean-field theories described so far. First, they do not capture the effect of *oscillating charge density* in front of the electrodes which can be observed

in simulations [52] or atomic force microscopy experiments [53]. Second, ion size effects going beyond the approximation of symmetric ions are not included. In principle, the influence of local ion-ion correlations can be formulated in a expanded expression for the Helmholtz free energy [50]

$$F = e\varphi(N_+ - N_-) + L_+N_+ + L_-N_- + CN_+N_- - k_BT\ln(\Omega) \tag{4.16}$$

with expressions $L_\pm$ and $C$ for the local ion (cross-)correlations that could also include ion size effects. However, the incorporation of these terms doesn't allow a simple closed-form solution for the differential capacitance. Classical density fundamental theory (DFT) can capture these effects. In a model by Jiang and others [54], the excluded volume enters via a primitive *hard sphere* model for the electrolyte and the charged wall, ion-ion correlation are included using full electrostatic pair interaction instead of a mean-field description. The solution is found by minimizing the corresponding expression for the grand potential with respect to the ion density. The resulting ion profile shows a oscillating structure and also captures the effect of overcharged layers where the net charge in the first layer exceeds the surface charge on the electrode. The DFT approach consistently reproduces the transition from a *bell-shaped* to a *camel-shaped* differential capacitance for decreasing bulk density and also has the predicted asymptotic behavior of $DC(U) \sim 1/\sqrt{U}$ and is capable of incorporating different ion sizes (via differently sized hard spheres), which leads to an asymmetric DC.

## 4.2 Superionic state

The highest achievable capacitance values have been obtained when the average pore size matches the size of the desolvated ions [2, 1, 3]. Several MD studies [55–57] have replicated this experimentally observed capacitance peak in small slitpores. Aside from the compact filling of space, such an electrode network is also advantageous for like-

charge ion packing. This is because the effective electrostatic interaction between ions now includes the induced counter-charges in the surrounding metal, which effectively reduces the electrostatic interaction compared to the vacuum case [58–60]. This effect is termed *superionic state* [61, 62] and gives rise to an increase of the capacitance in subnanometer pores. The analytical expression for the superionic state is obtained by evaluating the electrostatic potential of a point charge confined between two infinite, grounded metal plates separated by distance $L$ in z-direction. The charge at $z_0$ now creates the potential

$$\varphi(z,R) = \frac{q}{\pi\epsilon_0\epsilon_r L}\sum_{n=1}^{\infty}\sin\left(\frac{n\pi z}{L}\right)\sin\left(\frac{n\pi z_0}{L}\right)K_0(\pi nR/L) \tag{4.17}$$

with zero order modified Bessel functions $K_0(x)$. With the asymptotic behavior of $K_0(x)$, which implies lateral distance $R$ from the point charge greater than the plate separation $R \gg L/\pi$, Equation 4.17 approximately decays exponentially in $R$. For numerical applications, this means that the sum in Equation 4.17 only has to be evaluated for small values of $n$ to reach good accuracy and the modeling is facilitated by the short-range character of the interaction. This exponential decay of the electrostatic interaction of ions in a metallic surrounding also is beneficial for charge accumulation in EDLCs.

## 4.3 Constant potential simulations

### 4.3.1 Planar electrodes: ELCIC

The 2D periodicity of a parallel plate setup with constant potential boundary conditions needs to be treated appropriately by the electrostatics solver. Here, the 3D electrostatic solver *P3M* is used alongside with an *Electrostatic Layer Correction with Image Charges* (ELCIC). ELCIC can employ metallic boundary conditions or any other dielectric contrast. [63–65]. This introduces local attraction of charged species towards

the metallic electrodes [66] contributes to the electrode surface charge and causes the electric field to vanish in the conducting material. However, there exists no reference potential and the facing electrodes are decoupled. This particular system, metallic boundaries without the following constant potential correction models *unconnected, ungrounded electrodes*. A substitute system would be unconnected metallic spheres in the limit of $r \to \infty$. Adding the constant potential correction to the algorithm models *grounded electrodes*: Considering all charges in the system, the total potential drop along the z-direction is the superposition of the fluctuating potential caused by the ions $\Delta\Phi_{ion}$ and the electrode charges $\Delta\Phi_{el}$. It should end up on the given constant potential drop $\Delta\Phi_{bat}$ of a virtual battery:

$$\Delta\Phi_{ion} + \Delta\Phi_{el} \stackrel{!}{=} \Delta\Phi_{bat}. \tag{4.18}$$

This shows that the ELCIC algorithm has to counter the ion potential and superimpose the target potential to obtain constant potential boundary conditions. $\Delta\Phi_{ion}$ is given by

$$\Delta\Phi_{ion} = \int_0^{L_z} E_z dz = \frac{1}{\epsilon L^2} P_z \tag{4.19}$$

with the global dipole moment in z-direction $P_z$ of ion charges $i$:

$$P_z = \sum_i q_i z_i. \tag{4.20}$$

$P_z$ is already calculated by the ELCIC algorithm, so the constant potential correction comes without additional computational cost. Finally, the superimposed virtual battery potential $\Delta\Phi_{bat}$ in this case simply results in the force

$$F_z = q\frac{\Delta\Phi_{bat}}{L_z}. \tag{4.21}$$

In more complex geometries beyond parallel plates, the resulting field of $\Delta\Phi_{bat}$ has to be calculated via Laplace's equation.

### 4.3.2 ICC*

The *Induced Charge Computation* (ICC*) algorithm calculates the induced charge on dielectric interfaces with arbitrary dielectric contrast [67], applied in this work to simulate curved, metallic electrodes. The interface has to be constructed by placing point charges $q_i$ (called ICC particles) that mimic discrete surface elements with area $A_i$ of the boundary. Also, a normal vector $\vec{n}_i$ is associated with the ICC particle, by convention pointing from region 1 with dielectric permittivity $\epsilon_1$ to region 2 with $\epsilon_2$. The discretization is based on the concept of a Gaussian pillbox and should be fine enough that the electric field $E_{1/2}$ through its caps can be considered homogeneous and the flux through the sides of the pillbox is negligible. This allows to evaluate the surface integral of the pillbox, the induced charge then is proportional to the discontinuity of the electric fields on the caps and can be written as

$$\sigma_i = \frac{\epsilon_1 \vec{E_1} \vec{n}_i - \epsilon_2 \vec{E_2} \vec{n}_i}{4\pi}. \tag{4.22}$$

With the requirement that region 2 is not accessible by real charges, the fields $E_{1/2}$ of a surface element $i$ can be written as the superposition of the field $E$ (generated by the real charges in region 1 and all other surface elements $j \neq i$) plus the surface charge contribution of the $i$th ICC particle $\sigma_i$:

$$E_{1/2} = \vec{E} \pm 2\pi\sigma_i \vec{n}_i / \epsilon_1. \tag{4.23}$$

Combining Equations 4.22 and 4.23 leads to the expression for $\sigma_i$

$$\sigma_i = \frac{\epsilon_1}{2\pi} \left( \frac{\epsilon_1 - \epsilon_2}{\epsilon_1 + \epsilon_2} \right) \vec{E} \vec{n}_i. \tag{4.24}$$

Because $\vec{E}$ also depends on all other $\sigma_j,\ j \neq i$, Eq. 4.24 actually is a set of coupled equations. In the implementation used in ESPResSo, the solution is obtained iteratively by a successive overrelaxation (SOR) scheme. In each iteration step $k$, $\vec{E}$ is calculated once by the electrostatic solver and all $\sigma_i^k$ are updated according to

$$\sigma_i^{k+1} = (1-\lambda)\sigma_i^k + \lambda\sigma_i. \tag{4.25}$$

In practice, $\lambda \lesssim 1$ leads to a quick convergence of the surface charges [67]. Although possible, using ICC* for planar electrodes is not recommended. It requires additional charges and includes the computationally demanding part of the recalculation of $\vec{E}$ in each iteration step. The advantage of fast 3D periodic electrostatic solvers in a constant potential setup can also be obtained by using ELCIC. ICC* is best used for advanced, non-planar electrode shapes like the slitpore geometry investigated in this work.

## 4.4 Molecular dynamics simulations with ESPResSo

All simulations except the systems in chapter 6 and the MC results of the cooperation in chapter 8 were performed with ESPResSo Version 3.3.1, an *Extensible Simulation Package for the Research on Soft matter* [68, 69, 66]. The code is maintained and further developed at the Institute for Computational Physics, University of Stuttgart and other contributors of the ESPResSo community. It is "a highly versatile software package for performing and analyzing scientific Molecular Dynamics many-particle simulations of coarse-grained bead-spring models as they are used in soft-matter research in physics, chemistry and molecular biology" (https://www.espressomd.org). The user controls the system setup, interactions, the evolution in time and eventually analysis and data processing by an external script. In version 3.3.1, the used scripting language is TCL, up from version 4.0 it has been switched to the more modern language Python. ESPResSo itself is written in C++ and allows to include desired features at compile time for optimal performance.

# 5 Electrode structures and boundary methods in parallel plate capacitors

Parts of the content in this chapter has been published in the following article. My contributions: Simulations, data analysis and writing.

> **K. Breitsprecher**, K. Szuttor and C. Holm
> "Electrode Models for Ionic Liquid-Based Capacitors"
> *The Journal of Chemical Physics C*, **2015**, 119 (39), pp 22445-22451
> URL: https://doi.org/10.1021/acs.jpcc.5b06046

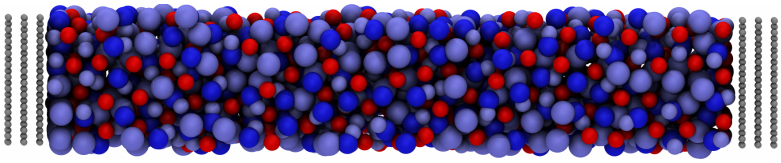

Figure 5.1: Side view of the planar plate capacitor system in the charged state showing the three graphene sheets (gray) and the coarse grained electrolyte model with the three-site BMIM cations (blue) and single-site $PF_6$ anions (red).

Understanding the very basic parallel plate capacitor setup is the starting point for investigations of more complex electrodes. In this chapter, the focus is on *two important model aspects* of capacitor simulations and their effects on the coarse grained ionic liquid BMIM $PF_6$:

1. **Electrode structure:** The particle based approach models the explicit *atomic* structure of a solid state graphite electrode. This is compared to the approxima-

tion of a continuum interface modeled by a one-dimensional interaction potential i.e. a *smooth* electrode.

2. **Boundary method:** The straightforward approach to simulate the charged state of the capacitor is to simply fix the charges $\pm Q_e$ on the electrodes. This *constant charge* approach however doesn't take into account the charge fluctuations on the electrode surface caused by local fluctuations of the ionic liquid. Also, the total potential drop between the electrodes is a result of the simulation. In the *constant potential* setup, a fixed potential between the electrodes is maintained by fluctuating surface charges.

## 5.1 Simulation setup

Choosing the canonical ensemble (NVT) for the plate capacitor setup is motivated by several aspects: Controlling the box volume in a confined system needed for the *isothermal-isobaric ensemble* (NPT) is difficult, because the periodicity of a particles based electrode can not be preserved when increasing the box in xy direction. Anisotropic box size changes only in z-direction would mean that the electrode particles exhibit position fluctuations, which are transferred on the interfacial ion layers. This might be an interesting aspect for simulations of thermal vibrations of the solid-state electrodes, but would require validation of the pressure control and adaption of the 2D electrostatic solvers involved. Using the *microcanonical ensemble* (NVE) in capacitor simulation under applied voltage results in an unwanted temperature increase due to resistive heating [70]. The friction term of the Langevin thermostat in the used NVT ensemble however dissipates this additional energy and maintains the temperature. Throughout the electrode model study in this chapter, a temperature of $400\,\mathrm{K}$ was used in the simulations, a compromise between room temperature behavior and increased ion diffusion for computational efficiency. The downside of the Langevin thermostat is that it does not preserve the particle momentum. The result is a decor-

related particle motion on timescales of $1/\gamma$. A common argument for this thermostat method is that the Brownian noise is caused by smaller solvent particles, which are actually not considered as part of the model. A deeper comparison with the momentum preserving Nosé-Hoover thermostats concerning the results and computational aspects can not be provided due to the unavailability of the method in ESPResSo.

The following protocol describes system parameters and a commonly used logical structure of setting up MD simulations, particularly for ESPResSo (version 3.3.1).

1. The box size is adjusted to obtain a molar volume of $2.247\,\mathrm{m^3\,mol^{-1}}$ for 320 ion pairs. This results in the correct IL density of $1.38\,\mathrm{g\,cm^{-3}}$ under normal pressure conditions at $400\,\mathrm{K}$ [24]. For the systems with smooth electrodes, a simulation box size of $30\,\text{Å} \times 30\,\text{Å} \times 126.7\,\text{Å}$ is used, the atomic graphene systems has a slightly adjusted box size of $27.2\,\text{Å} \times 30\,\text{Å} \times 147.83\,\text{Å}$ (including space for the 3 graphene layers on each side) to account for the periodicity of the graphene pattern in the xy-plane.

2. The particles are then randomly distributed in the box, excluding the interface regions. Several techniques of resolving the initial strong overlap are possible. It appears that force capping approaches are delicate, as particles may end up on the wrong side of the boundaries. Here, full forces are applied in the warm-up phase, but the ion diameter is gradually increased via the Lennard-Jones $\sigma$ values of the particles alongside with a strong translational friction and a smaller time step. In doing so, the particles stay close to their initial random positions and resolve the overlap with minimal translational and rotational motion.

3. With final interaction parameters set and activated Langevin thermostat, the system is equilibrated for $3\,\mathrm{ns}$.

4. For production runs with applied potential or electrode charge, the system is integrated for simulated times ranging between $12\,\mathrm{ns}$ to $18\,\mathrm{ns}$.

### 5.1.1 Electrode interaction models

The two short-range interaction models under investigation are labeled **atomic** for the explicit graphene structure and **smooth** for the unstructured planar Lennard-Jones representation. The graphene electrodes consists of three graphite sheets with 308 carbon atoms each. These are fixed in a hexagonal lattice structure with a C-C bond length of $1.42\,\text{Å}$ and plane distances of $3.35\,\text{Å}$. For the carbon short-range interactions, the common Lennard-Jones parameters $\sigma_\text{C} = 3.37\,\text{Å}$ and $\epsilon_\text{C} = 0.23\,\text{kJ/mol}$ [71] with Lorentz-Berthelot mixing rules are used.

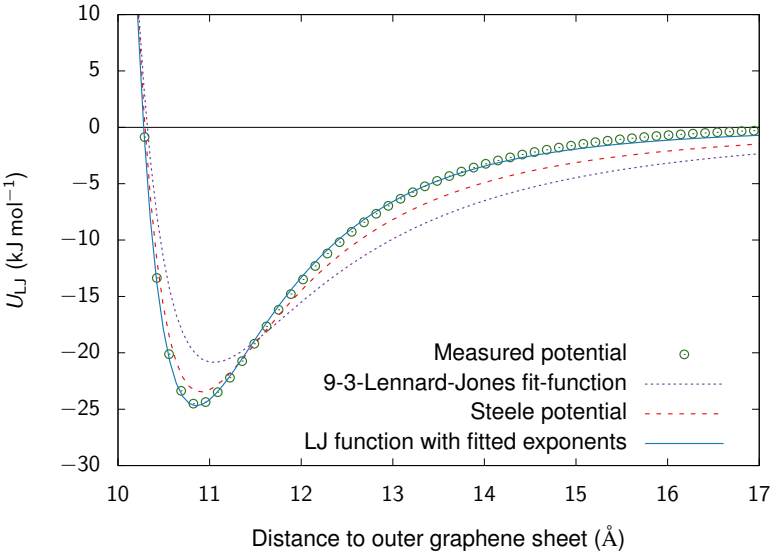


Figure 5.2: One-dimensional interaction potentials between electrode and ion. The laterally averaged graphene interaction energy (circles) is best described by a Lennard-Jones function with fitted exponents (solid line).

To obtain the smooth representation, the short-range interaction of the atomic electrode model is averaged in the xy-plane for several distances from the electrode and

fitted with different interaction potentials. Figure 5.2 shows the result of the procedure. A 9-3-Lennard-Jones function [72] fitted via $\epsilon_P$ and $\sigma_P$

$$U(z) = 4\epsilon_P \left( \left( \frac{\sigma_P}{z} \right)^9 - \left( \frac{\sigma_P}{z} \right)^3 \right) \tag{5.1}$$

shows the largest deviation from the target data. Also a Steele potential [73, 74] common for liquid-surface interactions fitted via $\epsilon_P$, $\sigma_P$ and $\rho$

$$U(z) = 2\pi\epsilon_P \rho \sigma_P^2 \Delta \left[ \frac{2}{5} \left( \frac{\sigma_P}{z} \right)^{10} - \left( \frac{\sigma_P}{z} \right)^4 - \left( \frac{\sigma_P^4}{3\Delta(z + 0.61\Delta)^3} \right) \right] \tag{5.2}$$

cannot capture the averaged atomic structure. It is found that a generic LJ-potential with non-integer exponents

$$U(z) = 4\epsilon_P \left( \left( \frac{\sigma_P}{z} \right)^{9.32} - \left( \frac{\sigma_P}{z} \right)^{4.66} \right) \tag{5.3}$$

with the parameters $\sigma_P = 3.58\,\text{Å}$ and $\epsilon_P = 24.7\,\text{kJ/mol}$ resulted in a precise representation of the graphene interaction data.

### 5.1.2 Electrostatic boundary conditions

In the constant charge setup, the electrodes possess the total surface charge density

$$\sigma_{tot}(\Delta\Phi) = \pm(\sigma_{ind} + \sigma_{bat}). \tag{5.4}$$

$\sigma_{bat}$ is the surface charge density of the capacitor in the vacuum case, $\sigma_{ind}$ is the contribution of the induced charges on the conducting electrodes due to the ions. This share depends on the actual ion configuration at the interface and is not known a priori. For a direct comparison, the average surface charge is determined at constant $\Delta\Phi$ and used as input for the constant charge simulations. For the constant charge computation, $\sigma_{ind}$ is included in the applied surface charge and no induction method is used in this setup, equivalently no dielectric contrast is set in the 2D electrostatics solvers.

The surface charge can either be modeled *explicitly* by a charge lattice on the electrodes or by a simple *homogeneous electric field* $E_z$ throughout the system. This results in the force $F_z = qE_z$ on the ions and is more efficient in case of planar electrodes, as no additional explicit charges are needed. To investigate the effect of charge discretization on the IL ordering in the close proximity of the electrodes, both *explicit* and *homogeneous* constant charge simulations are carried out. These two setups are compared against *constant potential* simulations carried out with the ELCIC method described in Section 4.3.

### 5.1.3 Ion model

The IL used in this chapter is the coarse grained model of the imidazole based BMIM $PF_6$ developed by Roy and Maroncelli [75, 24]. It has four sites with different Lennard-Jones parameters and partial charges which sum up to $\pm 0.78\, e$. The three-site 1-Butyl-3-methylimidazolium (BMIM) is modeled by Lennard Jones spheres on the central imidazole ring, the methyl and the butyl chain with a total mass of $139.23\,\mathrm{u}$. The hexafluorophosphate ($PF_6$) is modeled as a spherical particle with a mass of $144.96\,\mathrm{u}$. A sketch of the original molecule and the individual parameters is shown in Figure 5.3.

### 5.1.4 Potential contributions

With increasing applied potential, more and more distinct ion layers are forming at the electrodes. In highly concentrated electrolytes, molten salts or ionic liquids, the effect of overcharging appears, where the net charge in the first layer exceeds the charge on the electrodes surface itself. The system ends up in a state with an oscillating charge density perpendicular to the electrodes with alternating sign of the net charge per layer. The number of layers depends on the applied potential and the electrolyte. To give an estimate, atomic force microscopy experiments showed around four distinct adsorbed electrolyte layers at a gold electrodes with an applied potential of $1\,\mathrm{V}$ [76]. In these systems, the term *double-layer* might be misleading, as it describes the electrode sur-

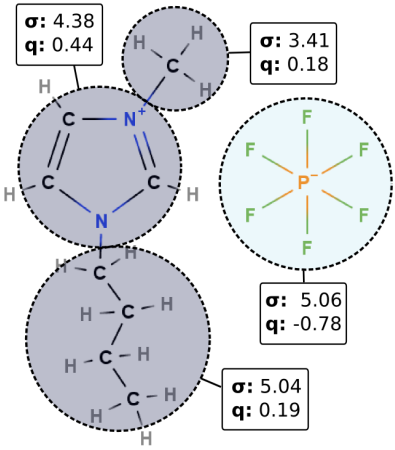


Figure 5.3: Coarse grained BMIM $PF_6$ model with partial charges and LJ parameters.

face charge on the one side and multiple interfacial layers in the electrolyte. Due to the parallel plate setup, the potential contributions of the layers involved can be derived with the one-dimensional Poisson's equation and charge neutrality arguments: Eventually, the charge density oscillations decay to zero at screening length $d$, completely screening the electrode charge $\sigma_{tot}$:

$$\sigma_{tot} = \int_0^d \rho(z) dz. \tag{5.5}$$

The value $d$ marks the onset of the electrolyte bulk, where the structuring effect of the electrodes has receded and the electrolyte is present in its liquid phase. The plate separation $L_z$ has to be large enough that a certain volume of IL bulk is retained. In the parallel plate capacitor setup,

$$L > d_a + d_c \tag{5.6}$$

with screening lengths $d_a$ and $d_c$ of anode and cathode due to the asymmetry of the ion species must be fulfilled to avoid overlap of the interfacial structures. In the simulation,

each applied potential then yields two potential drops $\varphi_1$ and $\varphi_2$ from electrode to the box center. These can be obtained by integrating twice over Poisson's equation:

$$\begin{aligned} -\epsilon_0\epsilon_r\nabla\varphi_{\text{ions}}(z) &= \int_0^z \rho(z')dz' \\ -\epsilon_0\epsilon_r\varphi_{\text{ions}}(z) &= \int_0^z \int_0^{z'} \rho(z'')dz''dz' \\ -\epsilon_0\epsilon_r\varphi_{\text{ions}}(z) &= z\int_0^z \rho(z')dz' - \int_0^z z'\rho(z')dz' \\ &= \int_0^z \rho(z')(z-z')dz'. \end{aligned} \tag{5.7}$$

The total potential also includes the contribution of the surface charge on the electrodes:

$$\varphi_{\text{el}}(z) = \int_0^z E_p dz' = \frac{z\sigma_{tot}}{\epsilon_0\epsilon_r} \tag{5.8}$$

which leads to the expression

$$\begin{aligned} \varphi_{\text{tot}}(z) &= \varphi_{\text{ion}}(z) + \varphi_{\text{el}}(z) \\ &= -\frac{1}{\epsilon_0\epsilon_r}\int_0^z \rho(z')(z-z')dz' + \frac{z\sigma}{\epsilon_0\epsilon_r} \\ &= -\frac{1}{\epsilon_0\epsilon_r}\left(z\int_0^z \rho(z')dz' - \int_0^z z'\rho(z')dz' - z\sigma\right). \end{aligned} \tag{5.9}$$

Now, the individual potential drops $U_1$ and $U_2$ can be evaluated:

$$\begin{aligned} U_1 &= \underbrace{\varphi_{\text{tot}}(0)}_{=0} - \varphi_{\text{tot}}\left(\frac{L}{2}\right) = \frac{1}{\epsilon_0\epsilon_r}\left(\frac{L}{2}\underbrace{\int_0^{\frac{L}{2}}\rho(z')dz'}_{=\sigma} - \int_0^{\frac{L}{2}} z'\rho(z')dz' - \frac{L}{2}\sigma\right) \\ &= -\frac{1}{\epsilon_0\epsilon_r}\int_0^{\frac{L}{2}} z\rho(z)dz \end{aligned} \tag{5.10}$$

$$U_2 = \varphi_{\text{tot}}\left(\frac{L}{2}\right) - \varphi_{\text{tot}}(L) = -\frac{1}{\epsilon_0\epsilon_r}\left(L\sigma + \int_{\frac{L}{2}}^L z\rho(z)dz\right). \tag{5.11}$$

Note that the electrode at $z = 0$ was put on a zero reference potential and charge neutrality in the bulk as in eq. 5.5 was assumed. The total potential drop throughout the system reads as

$$\varphi_{\mathrm{tot}}(L) = \frac{1}{\epsilon_0 \epsilon_r} \left( \int_0^L z\rho(z)dz + L\sigma \right) \tag{5.12}$$

where the first term is the potential due to the polarization $P_z$ of the dielectric i.e. the rearrangement of ions and the second term is the potential caused by the electrode surface charge. With averaged charge densities from the simulations, Equation 5.12 can now be used to match the constant charge approach with a given $\sigma$ and the constant potential approach with given $\varphi_{\mathrm{tot}}(L)$.

## 5.2 Results

### 5.2.1 Capacitance response

A series of simulations in the *constant potential* setup with different applied potentials in the range of $0\,\mathrm{V}$ to $6\,\mathrm{V}$ is carried out. The differential capacitance (see eq. 4.4) expressed how the system reacts on the applied potential. It also contains the nonlinearity of the electrolyte response. In a *linear* capacitor, e.g. with a solid dielectric, the polarization of the individual atoms can be considered linear and the capacitance is constant. Eventually, this approximation will break down at high voltages, but in an EDLC the nonlinearity is present at working voltage. $DC(U)$ also includes the asymmetry of the IL behavior at anode and cathode. Each simulation at a certain initial ("battery") surface charge now results in the two pairs $+\sigma, U_1$ and $-\sigma, U_2$ determined by equation 5.10 and 5.11. The differential capacitance is then obtained by numerical differentiation of $\sigma(U)$. Here, a noise robust differentiation scheme is used [77]. A maximum in $DC(U)$ corresponds to the situation, where the polarization response of the IL is the strongest.

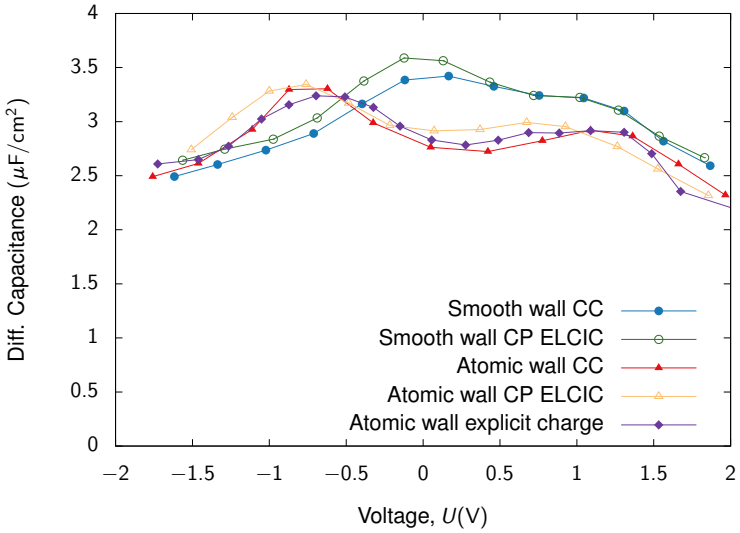


Figure 5.4: Comparison of the differential capacitance for the various electrode models. The DC curves match for the electrode boundary conditions used, but differ for the electrode structure models.

Figure 5.4 compares the resulting $DC(U)$ curves of five electrode models. For the *constant charge* and *constant potential* method, similar results are observed. This is expected when sampling the ion distribution over sufficient simulation times, as the differential capacitance is a static quantity. A large difference in $DC(U)$ between those system classes would indicate that the simulations show non-equilibrium behavior in the timescale reached by the simulation. In the constant charge setup, the field caused by the fixed surface charge density is homogeneous, whereas in the constant potential setup, the induced charges are calculated locally via image charges by the ELCIC method. However, this discretization in the surface charge should not play a role in the xy-averaged charge density which is used to calculate $DC(U)$, but it does enforce increased sampling in the constant potential setup as it introduces local potential minima via the discretized surface charges instead of a smooth charge distribution.

A more significant difference can be observed comparing the *smooth* and *atomic* electrode structures around $0\,\mathrm{V}$ with a deviation of about $1\,\mu\mathrm{F\,cm^{-2}}$. At higher voltages $|U| > 1.5\,\mathrm{V}$, all curves start to align. This indicates that the influence of the atomic structure is most pronounced at low voltages. The texturing influence by the graphene electrodes on the arrangement of the adsorbed ions is less important than the structure imposed by the applied potential in the high voltage regime both for anode and cathode. However, the differential capacitance for the two system classes differs in location of maxima and saddle points in the intermediate and low voltage regime. To relate these characteristic points to voltage induced structural transitions, charge- and mass density profiles as well as orientation effects are analyzed in the following sections.

### 5.2.2 Structural effects

In simulations, one can exploit the symmetry of the planar electrode geometry. For the analysis of the ion structure, it is convenient to use laterally averaged density profiles $\rho(z)$ with the single remaining dimension $z$ denoting the perpendicular direction from the electrodes. This kind of data averages over the *in-plane* ion structure, which is addressed in section 5.2.3. The focus here lies on structural differences of the *atomic* and *smooth* electrode models. The following Figures 5.5, 5.6 and 5.7 compare profiles at the interface for three applied potentials $0\,\mathrm{V}$, $2.4\,\mathrm{V}$ and $4.8\,\mathrm{V}$. The charge density in Figure 5.5 and also the mass density in Figure 5.6 show that already at zero potential, the boundary induces a distinct structure in the IL. Both anode and cathode have a positively charged first layer at $0\,\mathrm{V}$, which is attributed to the to the larger size of the BMIM cation and the depletion of the smaller anion. With increasing voltage, more and more pronounced oscillations in the charge density appear.

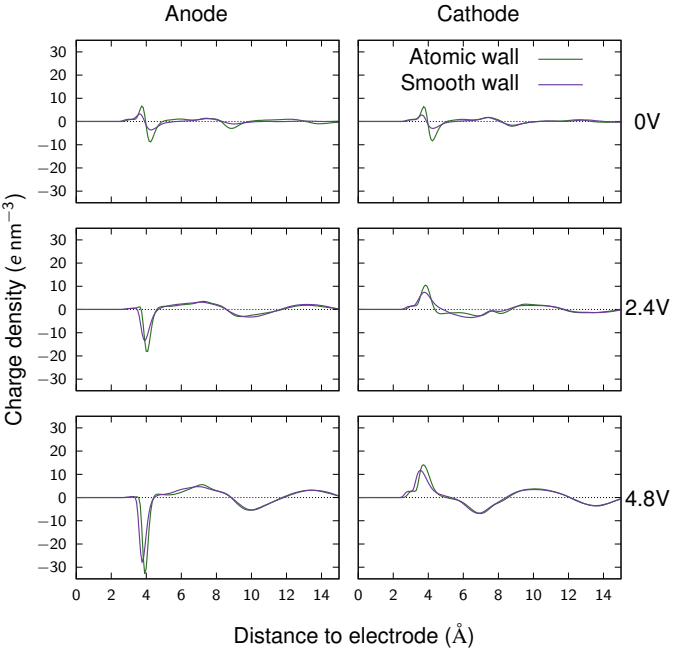


Figure 5.5: Charge densities at the electrode interface for the structural models at different applied potentials. The adsorbed first layer is slightly more pronounced in case of explicit graphene electrodes.

An important observation is that the first peak, referred to as the *first layer*, increases the most if a potential is applied. This means that the majority of the ion restructuring takes place directly at the electrodes. The effect of the *smooth* and *atomic* electrode structures on the charge density is twofold: (i) In case of the atomic electrode, the first layer is more pronounced. This enhanced ion adsorption on the structured surface is attributed to the larger surface area of the structured electrode. (ii) The peaks of the primary layers slightly do not match for the two models. On the smooth surface, the ion layer is shifted towards the electrode for both BMIM and $PF_6$ by about $0.3$ Å at $4.8$ V. The shift gets larger for higher potentials and is also visible in the mass densities in Figure 5.6.

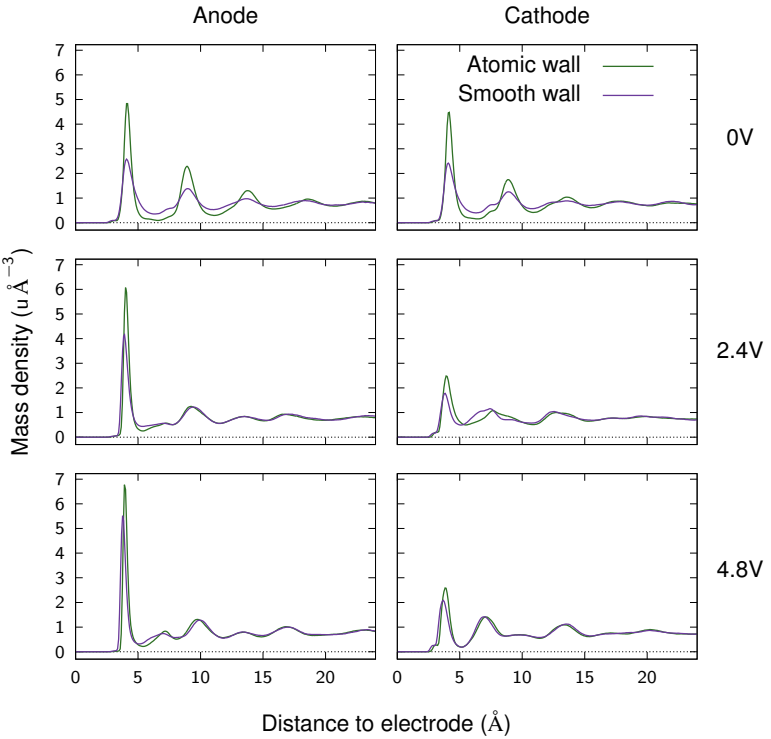


Figure 5.6: Mass densities at the electrode interface for the structural models. Again, the plot shows increased adsorption at the atomic wall. The ions can approach the boundaries more closely in case of the smooth electrodes.

Away from the electrodes, the curves approach the bulk density of $1.38\,\mathrm{g\,cm^{-3}}$ = $0.8311\,\mathrm{u\,Å^{-3}}$. At the cathode, the separation of charges in the interface region appears as a reduction - and at the anode as an increase of the first peak in the total mass density going towards higher potential. This is because the BMIM cation has a similar molar mass than the anion but increased excluded volume, so swapping of anions and cations in the first layer reduces the mass density.

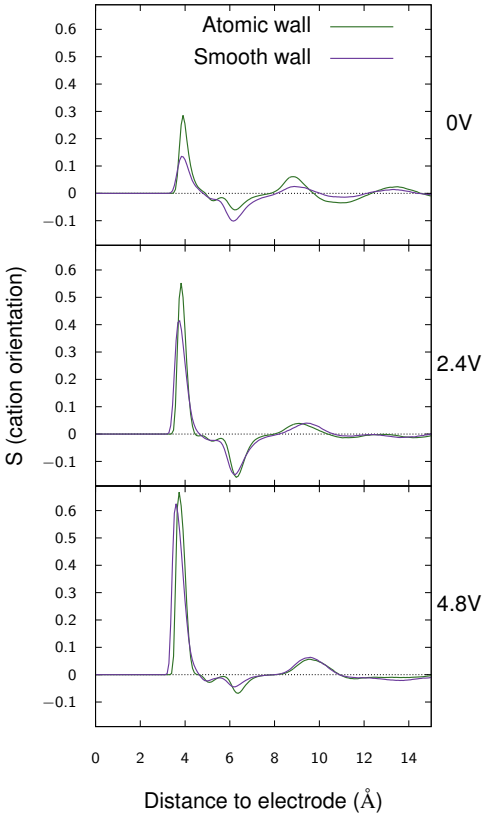


Figure 5.7: Cation orientation comparison at the cathode for the structural models. For higher applied potentials, the cations more and more show flat alignment. Also, the difference between the models tends to decrease for increasing voltage.

In Figure 5.7, the averaged lateral cation orientation is compared between the LJ-walls and graphene electrodes at different voltages. This is characterized by the *Second Legendre polynomial*

$$S = \frac{3}{2}\cos^2\alpha - \frac{1}{2} \tag{5.13}$$

with $\alpha$ being the angle between the z-axis and the normal vector of the plane defined by the three cation beads. A value of $S = 1$ corresponds to parallel (flat) cation alignment, perpendicular (upright) orientation results in $S = -0.5$. Overall, the difference again is most pronounced in the first layer, where an enhanced flat alignment on the structured surface is observed. In the more diffuse, negatively charged second layer, the cations are more likely to be found perpendicular. At $4.8\,\mathrm{V}$, the local minimum in $S$ at $z = 6.2\,\text{Å}$ is significantly reduced, showing a potential induced reorientation from upright to flat cation alignment.

### 5.2.3 In-plane radial distribution

The two-dimensional radial distribution functions $g(r)$, evaluated in the first ion layer in front of the electrodes gives an insight about the in-plane ordering of the adsorbed ionic liquid. The distributions of counterions around counterions ($g_{AA}(r)$ at the anode and $g_{CC}(r)$ at the cathode) for three different voltages and all electrode models are shown in Figure 5.8. Additionally, the plot includes the bulk radial distribution of the counterion species. The first layer is here defined as the range in z-direction from the electrode to the first global minimum of the counterion density. In the analysis of $g_{CC}(r)$, the center of mass of the BMIM cation is used, including adsorbed molecules with a tilted orientation in the first layer. Comparing the different distributions, the following qualitative observations can be made:

- The *electrode charge method* has no significantly impact on the in-plane radial distribution functions (Figure 5.8 *a* vs *c*, *b* vs *d*, *e* vs *g* and *f* vs *h*).

- When comparing atomic and smooth walls (in *a* vs *e* and *b* vs *f* within the constant charge results, *c* vs *g* and *d* vs *h* within the constant potential results), the position of extrema does not change significantly. The graphene systems shows additional features at distinct positions in the radial distribution functions which persist through all voltages for the anions at the anode (*a*, $r = 8\,\text{Å} - 10\,\text{Å}$),

whereas cations only show significant deviations at low voltages (*b*, $r = 11\,\text{Å}$). This can be explained by the ion models: The impact of the hexagonal graphene structure is stronger on the spherical anions, which can be patterned more easily than the anisotropic cations.

- The comparison between anode and cathode shows that the voltage transition is much more distinct at the anode. In Figure 5.8 *a*, the average distance between the anions drops when the voltage is increased, which is the result of anion accumulation during charging.

- The cation behavior in *b* is related to the cation reorientation with increased voltage: instead of pushing additional cations in the first layer, the system reacts with the reorientation of tilted cations towards parallel alignment which has a smaller effect on the in-plane cation pattern than ion exchange and results in the potential independence of $g_{CC}(r)$ and a robust position of the main peak with increasing voltage.

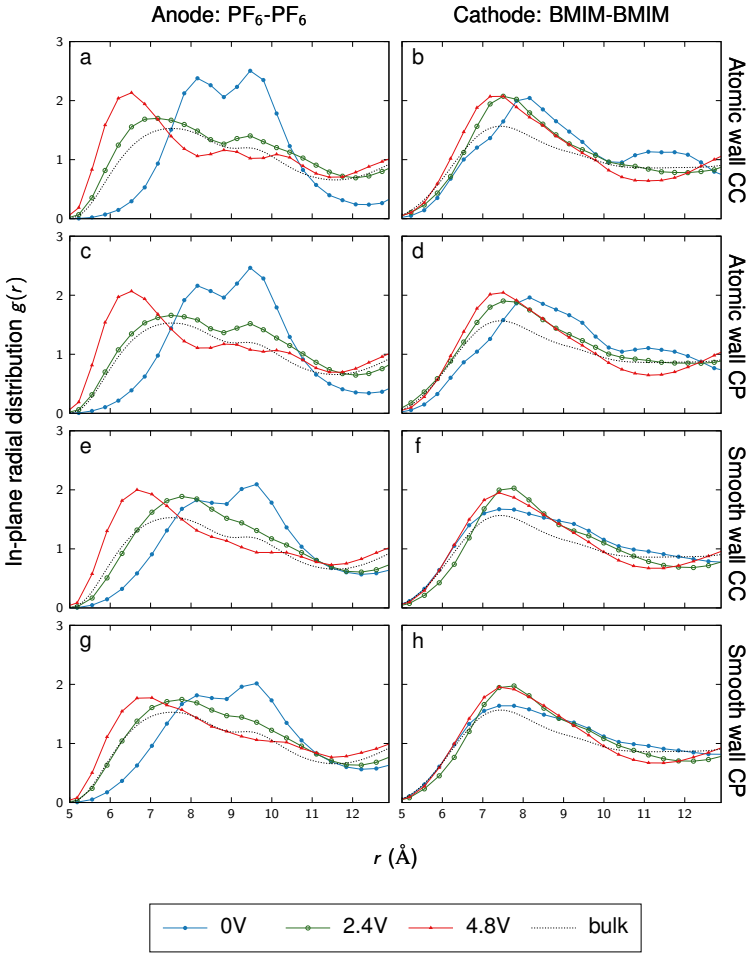


Figure 5.8: The in-plane radial distribution function of the first layer, including particles up to the first local minimum of the counterion density. Data is provided for counterion-counterion distributions at the respective electrode for different voltages. Additionally, the dashed lines show the bulk distributions.

### 5.2.4 First layer analysis

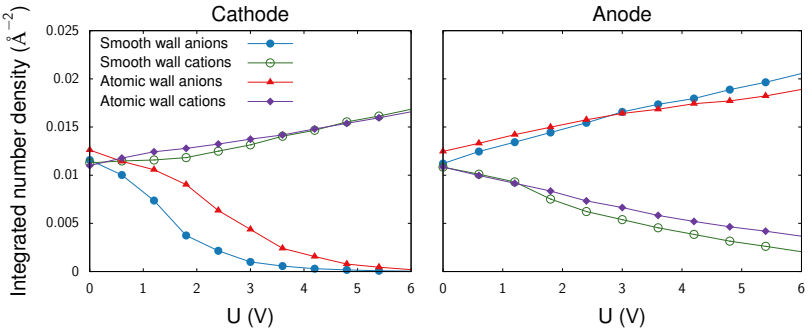


Figure 5.9: Voltage dependence of the number of ions in the first ion layer for smooth and atomic walls. In the case of structured electrodes, the migration of co-ions is shifted to higher potentials. This effect is more pronounced for the spherical anion.

Figure 5.9 shows integrated ion number densities in the first layer for the two electrode structure models. Here, the first layer is defined as the range from the electrode to the first local minimum in the *mass density* $\rho_{an}(z) + \rho_{cat}(z)$ (see Figure 5.6). Both adsorption and desorption, measured by the absolute slope of the data in Figure 5.9, is higher for the anions than for the cations. This shows that the migration of the spherical anions is favored over the more bulky cations. Further, anion desorption (left subplot, lower curves) has a strong nonlinear potential behavior compared to cation desorption (right subplot, lower curves). The transfer of ions is similar for the *atomic and smooth* electrodes, with the largest deviation to be found for anions at the cathode. There, co-ion desorption is shifted significantly to higher potential in case of *atomic* electrodes. The particles can become slightly trapped by the hexagonal rings and the structured graphene surface will contribute to the binding of the ions. This increased ion adsorption for the graphene electrode is also reflected in the differential capacitance. Similar to the voltage induced reorientation, the applied potential has to reach a certain level to

overcome the additional adsorption in case of an *atomic* structure. This delayed desorption contributes to the double-hump like shape of the differential capacitance of the graphene systems.

## 5.3 Conclusions

The two different electrode charge models showed no significant influence on the capacitance, density behavior or the first layer in-plane structure. It has been shown previously [78, 79] that at higher voltage, local charge induction can have an effect on the ion structure. With charge induction methods, the local energy gain of an adsorbed ion may break local particle structures like favorable ion orientations or weak ion coordination. However, the results here show that within the simulated voltage range, the constant charge approach yields similar behavior compared to the constant potential method. Obtaining dynamical properties like charging time or using a time-dependent voltage protocol however requires that the electrode surface charge is adaptive. An *atomic* or *flat* surface structure of the graphene electrode leads to subtle differences in both the lateral behavior in density and orientation, as well as the in-plane structure. The interfacial ions adapt to the local structure of the electrode and the subsequent layers will transfer this influence. The in-plane radial distributions revealed that the spherical anions are more affected by the electrode structure than the three-bead cation model. The resulting ion pattern emerges from the interplay between layer composition (set by the applied potential) and the entropic contributions of the wall-ion and ion-ion interactions. In a more densely packed layer (at higher voltages), the difference between anions and cations has a greater impact on the in-plane structure than the electrode model. Consequently, the effect of the *atomic* wall is more visible in the lower voltage regime and for the spherical anions. Further, the $PF_6$ anions showed a voltage-delayed desorption out of the first layer of the cathode compared to the desorption of the BMIM cations at the anode. This leads to the slight mismatch of the differential capacitance for the different electrode structures.

# 6 Effects of solvent concentration in nanoporous electrodes

Parts of the content in this chapter has been published in the following article. My contributions: Production simulations with "metalwalls", data analysis of the MD part, figures and snapshots and parts of the writing.

> R. Burt, **K. Breitsprecher**, B. Daffos, P. Taberna, P. Simon, G. Birkett, X. S. Zhao, C. Holm and M. Salanne
> "Capacitance of Nanoporous Carbon-Based Supercapacitors Is a Trade-Off between the Concentration and the Separability of the Ions"
> *The Journal of Physical Chemistry Letters*, **2016**, 7 (19), pp 4015–4021
> URL: https://doi.org/10.1021/acs.jpclett.6b01787

Although planar capacitor layouts are helpful to study a clean electric double layer without electrode geometry perturbations, high energy densities for storage devices can only be achieved with high surface area electrode material. In this chapter, the behavior of pure 1-ethyl-3-methylimidazolium tertafluoroborate (EMIM $BF_4$) and mixtures with acetonitrile (ACN, $CH_3CN$) is studied in nanoporous carbide-derived carbon (CDC) electrodes. The results from coarse grained MD-simulations are compared to cyclic voltammetry experiments with matching ACN concentrations and electrodes. Mixing RTILs with organic solvents is motivated by the high viscosity of pure RTILs, reducing the power density in highly porous carbon electrodes. The question arises if the use of these mixtures will affect the capacitance or energy density of EDLC devices. Ad-

ditionally, the quantitative comparison to electrochemistry experiments highlights the validity and limits of the MD setup. To be comparable, the simulations use a realistic CDC electrode geometry and constant potential boundary conditions. The average pore size and the particle diameters are close, which requires long trajectories to reach the final molecular composition in the pores. To obtain feasible particle numbers and simulation time, the system can only represent the very surface of the electrode-electrolyte interface. In application, the CDC network extends to macroscopic length scales (e.g. $120\,\mu\mathrm{m}$ in [80]) which is out of scope for detailed atomistic simulations. Preceding work on similar systems gave valuable insight from a simulation point of view on the storage mechanisms taking place in this setup [81, 82, 70, 83]. From experiments it was found that similar values of pore size and ion diameter can lead to a peak in capacitance [3]. The choice of EMIM $BF_4$ and CDC-800 electrodes [84] aims towards this size ratio.

## 6.1 Simulation Setup

### 6.1.1 MD setup

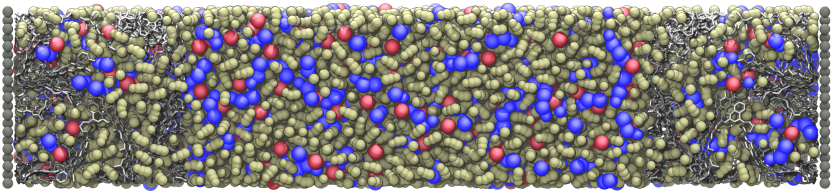

Figure 6.1: Simulation snapshot of the CDC capacitor setup. On the left and right, the box is terminated with a particle boundary (gray). The carbon structure is shown with virtual bonds to the next neighbors (silver). The electrolyte composed of acetonitrile (beige), EMIM cations (blue) and $BF_4$ anions (red). The snapshot shows the highest amount of solvent ($67\,\mathrm{wt}\,\%$ ACN) in the investigated concentration range.

An exemplary snapshot of the simulation cell can be seen in Figure 6.1. The electrodes represent a nanoporous CDC structure with an average pore size of $0.75\,\mathrm{nm}$ obtained by quenching a sample of liquid carbon [84]. The cubic electrode sample with side length $l_c = 43.4\,\text{Å}$ contains $3821$ carbon atoms, which are fixed in the simulation box. The CDC structure is used for both electrodes and mirrored at the box center. Bulk volume and electrolyte particle numbers vary for the different solvent concentrations.

| ACN mass wt % | 0 (pure IL) | 10 | 20 | 40 | 67 |
|---|---|---|---|---|---|
| Ion conc. (mol/L at 298.15 K) | 6.40 | 5.28 | 4.58 | 3.01 | 1.51 |
| Ion pairs | 600 | 601 | 608 | 326 | 324 |
| ACN molecules | 0 | 322 | 733 | 1048 | 3172 |

Table 6.1: Electrolyte compositions

Table 6.1 gives an overview of the ACN mass % and the corresponding ion concentration and MD particle numbers, spanning the range from pure IL to $67\,\mathrm{wt}\,\%$ acetonitrile. As in all MD studies, compromises in favor of computational efficiency have to be made, which are the limited CDC sample volume and a temperature of $340\,\mathrm{K}$ to increase the ion mobility and reduce the required simulation time. Another simplification is the use of coarse grained models for the employed electrolyte, which is a three-bead representation of the imidazolium-based cation and a single spherical bead for the $BF_4$ anion. The force-field was developed and tested in [85]. The acetonitrile is a linear three-bead model [86], intramolecular constraints are calculated with the RATTLE/SHAKE algorithm [87] and Lorentz-Berthelot mixing rules were employed for non-bonded interactions. The underlying simulation software with the working title *metalwalls* is a custom Fortran code used and developed at the MDLS in Saclay, specialized on molecular dynamics simulations of capacitors. The outstanding feature is the charge induction method for the constant potential ensemble, described by Siepmann and Sprink [88] and later Reed et al. [89]. The method is similar to the ICC* algorithm - according to the current ion configuration, it iteratively deter-

mines the induced surface charge with a minimization routine and maintains the applied potential between the electrodes. To account for smeared out charges on the curved graphene network, electrostatic interaction between Gaussian charges on the carbons and point charges on the moving particles is possible. The computationally expensive iterative calculation is the bottleneck of the simulation and significantly reduces the performance of the runs. For all Coulombic interaction calculations, 2D Ewald summation[90, 91] with a short range cut-off distance of $22\,\text{Å}$ was used, which is approximately half the box length in the shorter x and y cell dimensions.

### 6.1.2 MD equilibration scheme

Due to the size of the system, a deliberate equilibration scheme is used before the full setup with polarizable electrodes is applied. One can save simulation time by first relaxing the electrolyte without the numerous carbon atoms. To this purpose, NPT simulations at the target temperature of $340\,\text{K}$ and normal pressure were performed with the simulation package *Gromacs* for all ACN concentrations . These pre-equilibrated particle boxes were then placed between the CDC electrodes, followed by further relaxation in the NVT ensemble. To speed up the initial pore filling (still without applied potential), a fixed charge of $\pm 0.01\,e$ was set on all carbon atoms of the anode/cathode. The sign of these charges was flipped for 10 iterations, followed by another $500\,\text{ps}$ of equilibration with zero charge. After that, the second stage of equilibration continues in *metalwalls*. A problem that arises after the preceding equilibration procedure is that the bulk density is slightly too low and the precise amount of adsorbed electrolyte is unknown a priori. To reach the correct concentration in the bulk (obtained by the NPT simulations), the gap size was reduced by careful position rescaling until the density matched. From this stage, two charging schemes were applied. For dynamic charging, the electrode polarization was switched on, the half cell potential of $\pm 0.5\,\text{V}$ was applied and finally the system was propagated until the electrode charge sufficiently converged. Similar setups reported charging times of about $18\,\text{ns}$ [70], so the dynamic

charging only was applied to the pure IL and the highest ACN concentration of $67\,\mathrm{wt}\,\%$ ACN. For the other systems, a top-down charging (tdc) approach was used, where the charge of the carbon atoms was set to an initial guess of $0.01\,e$, the system was run with constant charges and only then the electrode polarization and applied potential was turned on. The initial guess exceeded the final electrode charge, hence the name top-down charging. This allowed to obtain the capacitance with much less simulation time, but also skipped the actual charging process. To motivate this approach, it is anticipated here that the computation time needed for approximately $18\,\mathrm{ns}$ simulation time was $816\,\mathrm{h}$ on 480 cores on the Hornet compute cluster. The computation was spread among the project partners at the MDLS in Saclay, resources were located at the Institut Henri Poincaré (Paris), the HLRS cluster Hornet (Stuttgart) and in the University of Queensland (Brisbane).

### 6.1.3 Electrochemistry experiments

The corresponding experiments were performed by the group of P. Simon in the *CIRIMAT Laboratory, Université Toulouse III - Paul Sabatier*. The EMIM $BF_4$ was purchased from *Solvionic* (France), the ACN from *Acros organic* (France). The electrolyte mixtures with ion concentrations listed in Table 6.1 were prepared at room temperature. The CDC powder was synthesized via high-temperature etching of titanium carbide (TiC) powder with chlorine gas following $TiC + 2\,Cl_2 \longrightarrow TiCl_4 + C$. With this procedure, highly porous CDC is obtained, the pore distribution is affected by the choice of the carbide precursor and etching temperature. Here, the applied temperature of $800\,^{\circ}\mathrm{C}$ corresponds to a maximum in pore size distribution at $0.77\,\mathrm{nm}$ [2, 3], which is very close to the value of $0.74\,\mathrm{nm}$ of the CDC sample used in the simulations. The CDC power was mixed with $5\,\mathrm{wt}\,\%$ polytetrafluoroethylene (PTFE) binder and laminated onto aluminum current collectors [92] with an active film thickness of $300\,\mu\mathrm{m}$. Two layers of $25\,\mu\mathrm{m}$ thick PTFE were used to separate the electrodes.

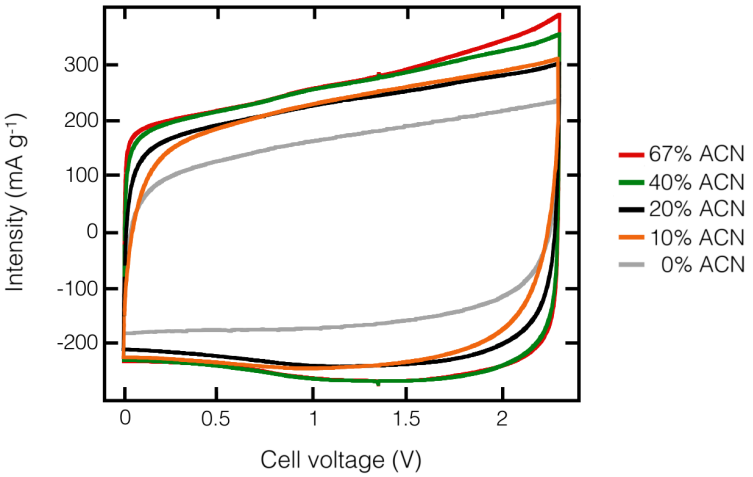


Figure 6.2: Cyclic voltammetry diagrams for the specific ACN concentrations also used in the simulations. With the CV data, the (integral) capacitance can be calculated and compared to the MD results. This plot and the underlying data was produced in the CIRIMAT Laboratory, Toulouse.

For the cyclic voltammetry, a silver wire reference electrode is placed in the cell center allowing to monitor anode and cathode separately. The cell was assembled under argon atmosphere with less than $1\,\mathrm{ppm}$ of $O_2$ and $H_2O$ content. Finally, cyclic voltammetry experiments at scan rates of $5\,\mathrm{mV\,s^{-1}}$ were carried out between $0\,\mathrm{V}$ to $2.3\,\mathrm{V}$ at room temperature for all ACN concentrations. Additionally, a lower scan rate of $1\,\mathrm{mV\,s^{-1}}$ and increased temperature of $373\,^{\circ}\mathrm{C}$ was applied for the pure IL case.

## 6.2 Results

### 6.2.1 Integral capacitance

In CV experiments, an ideal capacitor would result in a rectangular $I(U)$ curve with the specific capacitance given by

$$C_{ideal} = \frac{\frac{dQ}{dt}}{\frac{dV}{dt}} = \frac{I}{k} \tag{6.1}$$

with scan rate $k$ and measured current $I$. However, EDLC cells often behave far from ideality, caused by several effects. This makes $I(U)$ curves of CV experiments more difficult to interpret and compare, as influences of the cell setup, material properties and inherent effects of supercapacitors all come together. Some of these influences can be captured by an element in an appropriate equivalent circuit. In the following, issues related to the interpretation of CV data are listed:

- A non-zero series resistance of the real system rounds up the corners of the ideal CV rectangle. This can be associated with the finite conductivity of the electrodes and losses in the dielectric.
- Leaking current in the measuring cell gives rise to a superimposed linear behavior in $I(U)$ due to Ohm's law. The equivalent circuit element is a large resistance in parallel. In a sandwich-like cell setup with two electrodes and a isolation layer in between, leakage can appear through small currents through the isolation or the enclosing frame.
- Above certain cell voltages, electrolysis takes place at the electrode interface. The accompanied electron transfer causes *faradaic peaks* in the CV curve and contribute to the pseudocapacitance of the cell. These reactions are likely to be non-reversible and cause concentration changes in the electrolyte, molecular decomposition of the IL, electrode surface reconstruction or reactions of unwanted

residual substances.

- If the applied scan rates is too high and the cycle period exceeds the characteristic charging time of the capacitor, the charging process is not complete at the reverse point of the cycles and the measured capacitance is underestimated.

- Asymmetry of the $I(U)$ curve in forward and backward scan direction indicates charge-discharge asymmetry. A possible reason for this asymmetry are the already mentioned non-reversible redox reactions or non-equilibrium states due to incomplete charging.

The nonlinearity of the capacitance, i.e. its dependence on the applied potential is reflected in the CV curves but cannot be distinguished easily from the previously mentioned points. Also, temperature dependence of the faradaic processes or solvent evaporation introduces even another level of complexity. This complicates capacitance measurements and result in different values for the capacitance depending on the local current when simply using equation 6.1. A more reliable way of processing the CV data is to restrict the analysis interval to a range where the behavior is more close to the ideal capacitor. In application, that means to use the integral area of the CV curve following

$$C_{CV} = \int_{U_1}^{U_2} \frac{I(U)dU}{2k(U_2 - U_1)m_{el}}. \tag{6.2}$$

The experimental capacitance values obtained from the CV data shown in Figure 6.2 follow this approach and are calculated using equation 6.2 in the potential window between $0.5\,\mathrm{V}$ to $2.0\,\mathrm{V}$. Note that by doing so, a possible voltage dependent behavior of the capacitance is averaged over the range of the potential window. However, simulations where only performed at $1\,\mathrm{V}$ and $2.4\,\mathrm{V}$ which does not allow meaningful numerical differentiation of $Q(U)$ and analysis of the differential capacitance.

In the computer experiments, the integral capacitance at a given voltage $V$ is calculated using the mean charge of anode $Q_{anode}$ and cathode $Q_{cathode}$ directly measured in the simulations by summing over the charge of the electrode carbon atoms and averaging over the final time interval where the charging process is considered to be complete. The error is calculated by the standard deviation of $Q(t)$ in this interval. Further, the specific capacitance is normalized by the electrode weight $m_{el}$, which is simply given by the number of carbons in the pore geometry times the atomic mass of carbon $m_C = 12.0107\,\mathrm{u}$. The capacitance then is $C_{sim} = \frac{|\langle Q_{anode}\rangle|+|\langle Q_{cathode}\rangle|}{2m_{el}V^{\pm}}$.

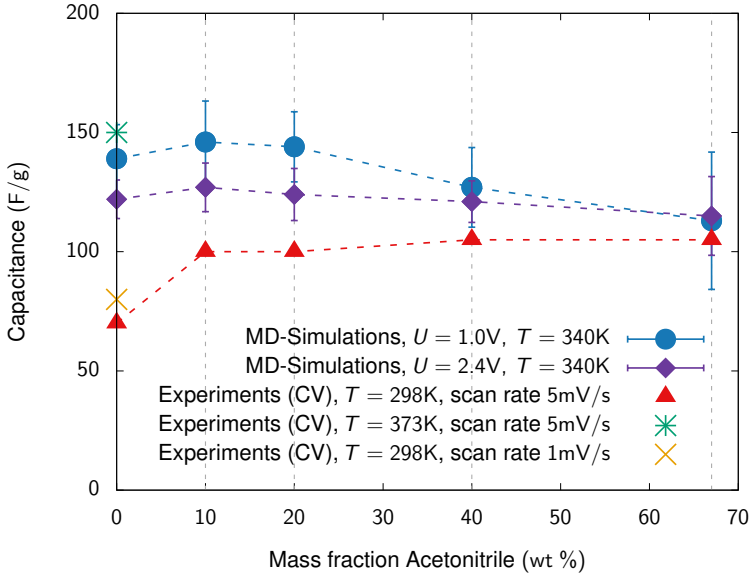


Figure 6.3: Integral capacitance from experiments and simulations (red triangles for varying ACN concentration, single stars at $0\,\mathrm{wt}\,\%$ ACN for temperature and scan rate tests; simulation data points at two voltages in blue and purple).

Figure 6.3 compares the specific capacitance obtained from simulations and CV experiments. The simulation data includes capacitance values for simulation runs at applied potentials of $1\,\mathrm{V}$ and $2.4\,\mathrm{V}$. CV results where obtained at $T = 298\,\mathrm{K}$, $k = 5\,\mathrm{mV\,s^{-1}}$ for the whole range of ACN mass fraction and two reference measurements with the pure IL at increased temperature $T = 373\,\mathrm{K}$, $k = 5\,\mathrm{mV\,s^{-1}}$ and reduced scan rate $T = 298\,\mathrm{K}$, $k = 1\,\mathrm{mV\,s^{-1}}$.

The overall trend from both simulations and experiments show no common systematic dependence of the capacitance on the amount of ACN. The simulation data exceeds the measured capacitance in all points, except the increased temperature run of the pure IL of $150\,\mathrm{F\,g^{-1}}$, which matches the simulation results but also doubles the measurement at room temperature. This strong dependence of the CV result on temperature, which is expected to be small [93], points in the direction of incomplete charging in the CV period due to the high viscosity of the pure IL [94]. The slightly increased measured capacitance at room temperature from $70\,\mathrm{F\,g^{-1}}$ at $5\,\mathrm{mV\,s^{-1}}$ to $80\,\mathrm{F\,g^{-1}}$ at a reduced scan rate of $1\,\mathrm{mV\,s^{-1}}$ supports this assumption. Unfortunately, more measurements at different temperatures and scan rates as well as extended simulations at room temperature where out of scope of the collaboration. Other sources of error in the simulations are the simplified models of the coarse-grained molecules, the limited CDC sample size and the treatment of the electrode as an ideal conductor [95]. However, the data is consistent with previous results using BMIM $PF_6$ and CDC electrodes with slightly larger pores [26]. The main result of the comparison in Figure 6.3 is that the capacitance is not strongly affected by the amount of acetonitrile solvent. From this one can infer that increasing the concentration of the IL is not an efficient way to increase the capacitance.

### 6.2.2 Pore composition

To further analyze how the solvent affects the system, the pore composition of IL and solvent for the difference ACN mass fractions are shown in Figure 6.4 for anode and cathode respectively. Additionally, the plots include the number of ion pairs in case of an uncharged electrode (purple line) and the difference between anion and cation numbers at applied potential (dashed green line). The data is taken from the simulation runs at applied voltage of $1\ \mathrm{V}$ and averaged over the last nanoseconds of the trajectories.

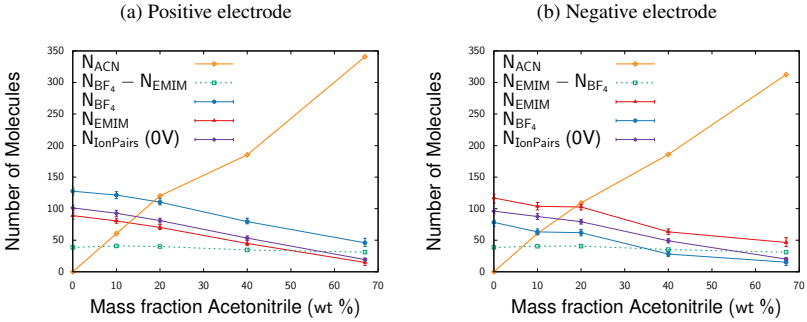


Figure 6.4: Particle counts within the pore volume as a function of ACN concentration.

A possible explanation of a constant capacitance is that the system has reached a saturated regime, where the number of adsorbed ions remains constant with varying solvent concentration. The simulations can rule out such a behavior, showing that the amount of IL molecules decreases and the pores get more and more filled with ACN. Instead, it is observed that the difference between EMIM and $BF_4$ particles, which is the net ion charge, is almost constant and follows the capacitance measured via the induced charge of the CDC electrodes. This coupling of ion- and electrode charge is demanded by charge neutrality arguments. Strictly, the induced charge is caused by the ions inside the pore and the interfacial ion layers reaching in the bulk region up to the point

of electroneutrality. In Figure 6.4, the number of molecules is calculated only in the pore volume excluding these interfacial ion layers, which explains the small difference between net ion charge $Q_{ion} = q(N_{BF_4} - N_{EMIM})$ and electrode charge $Q_{CDC}$. With applied voltage, differences in particle numbers between anode and cathode emerge, caused by the different roles of the IL species in anode and cathode. The smaller size of $BF_4$ compared to EMIM results in an increased amount of counterions in the anode and a decreased amount of co-ions in the cathode. However, this ion size effect vanishes at the highest ACN mass fraction, where there is little to no difference between the pore composition of anode and cathode. It can be concluded that the solvent balances ion size effects and leads to a more symmetric behavior of anode and cathode.

### 6.2.3 Charging mechanism

The comparison of pore compositions at zero and applied voltage in Figure 6.4 contains information about how many ions entered of left the pore during the charging process. In a simplified picture, three mechanisms are considered to increase the net ion charge in the pore volume: (i) Counter-ion adsorption, (ii) co-ion desorption and (iii) ion exchange. This can be captured by a single parameter $X$ (introduced by Forse et al.,[12]) that basically measures the change in particle numbers relative to the change in net ion charge and is defined as

$$X = \frac{N(\Psi) - N(0)}{(|Q(\Psi)| - |Q(0)|)/e} \tag{6.3}$$

with the total number of in-pore ions $N(\Psi)$ and net ion charge $Q(\Psi)$ at a given voltage $\Psi$. Figure 6.5 plots $X$ as a function of the ACN mass fraction. The charging parameter takes a value of 1 for counterion adsorption, 0 for ion exchange and -1 for co-ion desorption.

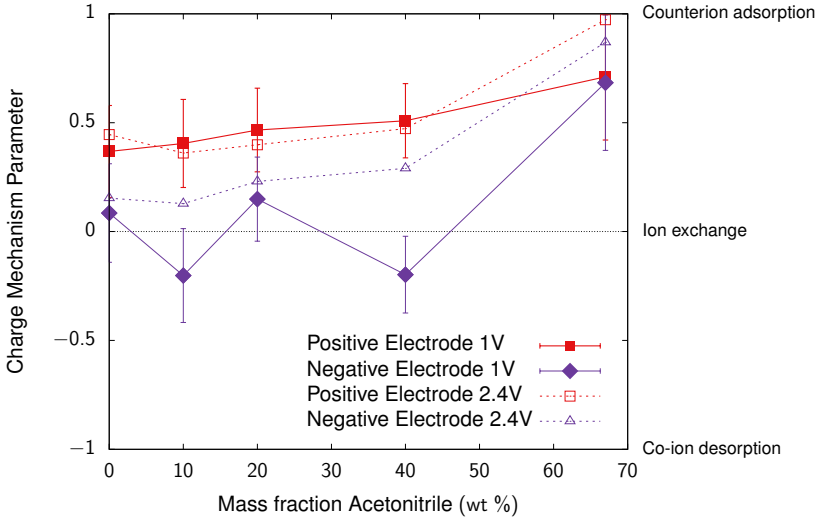


Figure 6.5: Variation of the charging mechanism parameter with the ACN mass fraction for the positive and negative electrodes at $1\,\mathrm{V}$ and $2.4\,\mathrm{V}$.

The plot includes data for the individual electrodes at $1\,\mathrm{V}$ (full lines and symbols) and $2.4\,\mathrm{V}$ (dashed lines and open symbols) for the full range of ACN concentration. In the positive electrode (anode), the charging is driven by counterion adsorption, progressively increasing with ACN concentration and is very similar for the two voltages. In the negative electrode (cathode), for $1\,\mathrm{V}$ adsorption and desorption balance out, classified as ion exchange by the charging parameter. Note that the fluctuations of $X$ for $0\,\mathrm{wt}\,\%$ to $40\,\mathrm{wt}\,\%$ ACN in the negative electrode at $1\,\mathrm{V}$ versus the rather smooth increase of $X$ in the positive electrode indicate that the ion configuration inside the cathode might not be converged and averaging over several independent simulation would be desired. For the increased voltage of $2.4\,\mathrm{V}$, the behavior of the positive electrode shifts towards stronger counterion adsorption. At $67\,\mathrm{wt}\,\%$ ACN, the results for both electrodes and voltages align and show the highest degree of adsorption. Again, the differences between the electrodes originate from the molecular shape of the ion

species: The spherical $BF_4$ molecule is smaller and more mobile than the bulky EMIM cation, thus both desorption and adsorption is favored for the anion. At the highest ACN concentration, this ion specific effect gets less important. Aside from electrode asymmetry effects, the data shows a global trend towards counterion adsorption with increasing ACN concentrations. If the pore is considered to be saturated, adsorption has to be accompanied with replacement of either solvent or co-ions. If the pore is predominantly occupied by ACN, it gets more likely to just replace solvent molecules, shifting $X$ away from the ion-exchange regime.

### 6.2.4 In-pore structure

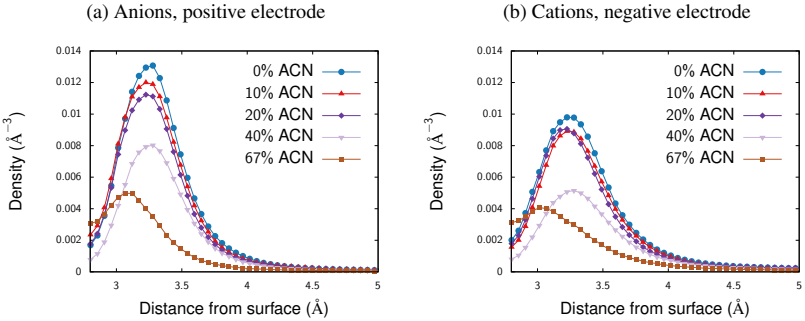


Figure 6.6: Counterion distance from the internal surface of the CDC network at 1 V.

Figure 6.6 shows a series of in-pore counterion densities as a function of the distance from the internal electrode surface for different fractions of ACN. The internal surface is determined by using reference simulations to probe the pore with an argon atom and keeping track of the accessible volume and the closest surface. Then the distance of a particle to the nearest carbon atom can be calculated and averaged over particle species and time.

The data in Figure 6.6 reveals several features of the in-pore ion structure for varying

ACN concentration:

- The shape of the distribution reflects the narrow pore size distribution close to the ion size allowing effectively only a single layer of counterions inside the network.

- Alongside with more ACN in the system, the peak height is reduced and consistently follows the number of counterions from Figure 6.4.

- The peak position for both electrodes resides robustly around $3.3$ Å again related to the small pore size.

- An exception of the last point is the surface distance in simulations with the highest ACN concentration, where the particles are slightly closer to the surface with am average distance of about $3.1$ Å. Possible explanations are that the reduced ion density leads to a tighter packing of ions and only the very narrow parts of the CDC pores are dominantly occupied by counterions for a high amount of ACN.

To further analyze the ion coordination inside the electrodes, the radial distribution functions $g(r)$ of the electrolyte species in the pore volume is shown in Figure 6.7 (a) and (b). As a reference, Figure 6.7 (c) contains the bulk data. In the plots, the amount of ACN is increasing from light to dark colors. For the three-bead cation model, the central particle modeling the imidazole ring is used for the calculation. As expected, oppositely charged species are strongly coordinated around distances in the range of $4$ Å to $5.5$ Å, which is close the diameter of the involved ions. Like-charge ion coordination then peaks in a broader region of $5.5$ Å to $9$ Å, followed by a third shell with almost vanishing magnitude. The most striking observation however is that the distributions within one electrode are almost unaffected by the amount of solvent in the system. The local maxima in $g(r)$ keep their positions and only slightly change in magnitude.

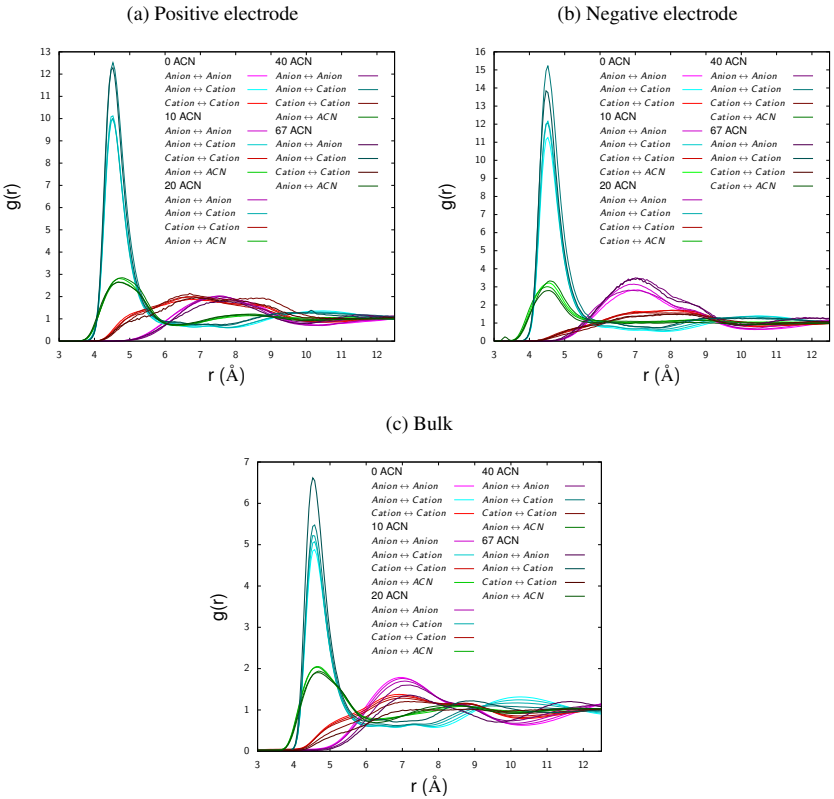


Figure 6.7: Radial distribution functions in the different regions of the simulation box. Color encoding shifts from light to dark colors for increasing concentration of ACN.

The latter effect is more pronounced in the negative electrode with $EMIM^+$ counterions, where the first maximum in the distributions between $Anion \leftrightarrow Cation$ and $Anion \leftrightarrow Anion$ is increased. The similar feature can be found in the positive electrode: There, the first peak of the $Anion \leftrightarrow Cation$ distribution in case of $0\,\mathrm{wt}\,\%$, $10\,\mathrm{wt}\,\%$ and $20\,\mathrm{wt}\,\%$ ACN collapses on a single line, as well as the curves for $40\,\mathrm{wt}\,\%$

and $67\,\mathrm{wt}\,\%$ ACN, with increased magnitude. This sudden change in distribution suggests that the observed differences in $g(r)$ are likely to be an geometry effect of the CDC structure. With less ions in the system, different regions in the electrode are preferably occupied and strongly overlay possible transitions in the solvation behavior. Such transitions can be found in the bulk (Figure 6.7 (c)): Only the first peak in $Anion \leftrightarrow Cation$ gets more pronounced, all other oscillations are damped and show slightly shifted maxima with growing amount of solvent. This can be summarized as a reduction in like-charge ion coupling and a complementary increase in oppositely charged ion coupling.

### 6.2.5 Ion coordination

The next set of Figures in 6.8 shows the coordination numbers of different combinations of particle species in both electrodes as a function of ACN concentration. It is calculated by simply counting the number of particles of species $j$ in a spherical volume around species $i$. The cutoff radii are chosen individually for a given pair of species such that they includes the first peak in the radial distribution and reach until the subsequent minimum. The detailed values of the cutoff radii are given in table 6.2.

| Species pair | $r_{cut}(\text{Å})$ |
|---|---|
| $Anion \leftrightarrow Cation$ | 7.3 |
| $Anion \leftrightarrow ACN$ | 6.4 |
| $Cation \leftrightarrow ACN$ | 7.7 |
| $Anion \leftrightarrow Anion$ | 10.2 |
| $Cation \leftrightarrow Cation$ | 10.5 |

Table 6.2: Cutoff radii for ion coordination numbers

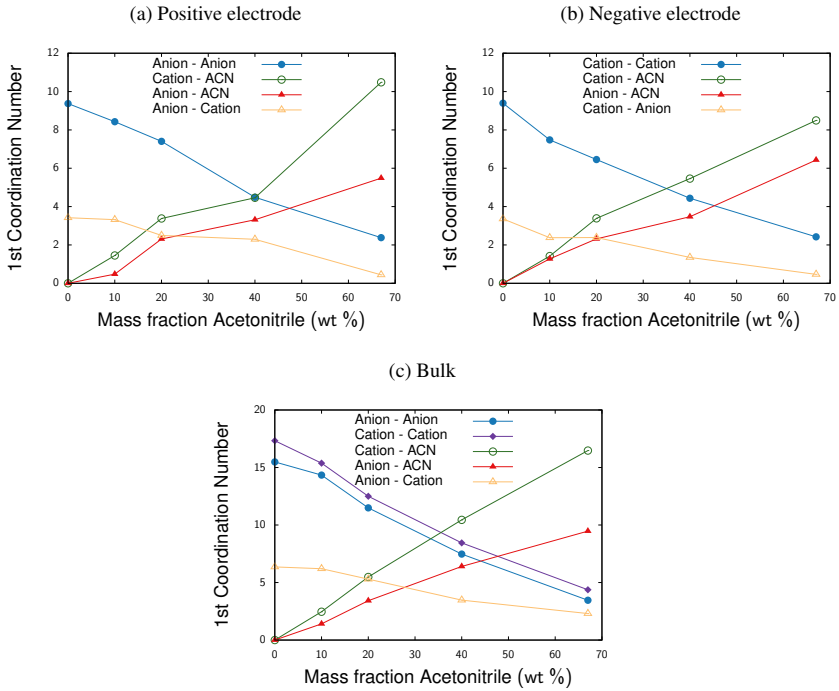


Figure 6.8: Coordination numbers in the different regions of the simulation box for an applied potential of 1 V as functions of the ACN concentration.

The coordination numbers in Figure 6.8 give a quantitative picture of the particle distribution and shows that in opposition to the robust radial probability distribution in Figure 6.7, the absolute numbers of neighbors does change and ions get more and more surrounded by solvent molecules with increasing ACN concentration. Further, EMIM-ACN coordination is favored over $BF_4$-ACN coordination in both electrodes. To answer how the electrodes affect the particle coordination, the data inside the electrodes is compared to the coordination numbers in the bulk, shown in Figure 6.8 (c). The comparison reveals that although the carbon particles occupy some of the accessible volume and scale down the overall coordination numbers, the solvation inside

the CDC electrodes is not drastically different from the bulk behavior. It is insightful to compare these results to the picture of completely dissociated electrolytes, where ions carry a solvation shell with elongated dipoles of the polar solvent that screen the central ion and effectively reduce ion-ion coupling. However, the $g(r)$ bulk data in Figure 6.7 (c) and the bulk coordination numbers in Figure 6.8 reveal that in the range of simulated solvent concentration from pure IL to $1.51\,\mathrm{mol\,L^{-1}}$, this simplified picture of solvated, isolated ions does not apply. The first maximum of the $Anion \leftrightarrow Cation$ radial distribution remains robustly at around $4.6\,\text{Å}$ and increases with the ACN concentration. The $Anion \leftrightarrow Cation$ coordination number in the bulk does drop from $\sim 6.3$ to $\sim 2.4$, which suggests a chain-like arrangement of alternating anions and cations. Corresponding to this observation, the configuration in the simulation snapshot in Figure 6.1 shows no tendency towards sole ions. More accurately, it could be described as a network of ions embedded in clusters of acetonitrile.

### 6.2.6 Charging dynamics

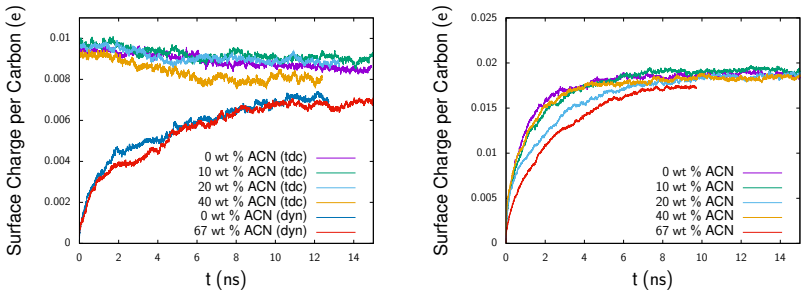


(a) Dynamic charging curves for top-down (tdc) and dynamic (dyn) charging at 1 V for various wt % ACN.

(b) Dynamic charging curves at 2.4 V for various wt % ACN.

Figure 6.9: Time evolution of the electrode charge.

Figure 6.9 shows the time evolution of the CDC surface charge per area obtained by the simulations. The data includes dynamic runs for 0 and $67\,\mathrm{wt}\,\%$ ACN and top-down charging runs for $0\,\mathrm{wt}\,\%$ to $40\,\mathrm{wt}\,\%$ ACN for $1.0\,\mathrm{V}$ in (a) and dynamic charging at a higher applied potential of $2.4\,\mathrm{V}$ in (b), which is a realistic voltage value for applied EDLCs on the border of the electrochemical window of EMIM $BF_4$ [96]. Both plots already reveal two main findings of the study: Firstly, no clear trend is observed for the different ACN concentrations. For both voltages considered, the surface charge ends at values between $0.007\,e$ to $0.009\,e$ per carbon for the simulations at $1\,\mathrm{V}$ and $0.017\,e$ to $0.019\,e$ per carbon for $2.4\,\mathrm{V}$. Secondly, the dynamic runs cannot support the assumption of reduced charging times when adding the organic solvent. The comparison between the most extreme cases, pure IL versus $67\,\mathrm{wt}\,\%$ ACN shows no acceleration of the charging process, which takes around $10\,\mathrm{ns}$ in all dynamic runs in Figure 6.9 (b).

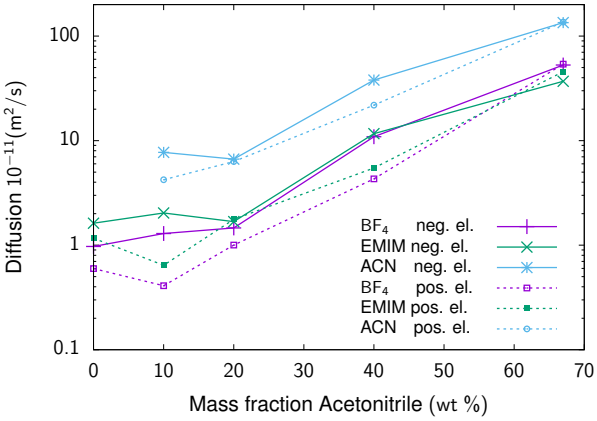


Figure 6.10: The in-pore diffusion for the positive (dashed lines) and negative (solid lines) electrode as a function of ACN concentration for the different particle species. More ACN solvent results in a large increase in diffusion.

What suggest a speedup of the charging process for macroscopic pores is the enhanced diffusivity in the pores with higher amounts of solvent, which is found in the

simulations. Figure 6.10 shows the in-pore diffusion coefficients with varying ACN concentration. The plot includes data from both electrodes and all involved molecules and is calculated from the charge-saturated part of the trajectories after $10\,\mathrm{ns}$ simulation time. Only particles inside the CDC volume are taken into account in the calculation. Due to the finite pore in z-direction, the mean squared displacement in xy-direction is used in the calculation of the diffusion coefficients via

$$D = \frac{\langle R(t)^2 \rangle}{2dt} \tag{6.4}$$

with dimensionality $d = 2$. Going from 0 to $67\,\mathrm{wt}\,\%$ ACN, a rise in diffusion from $1 \times 10^{-11}\,\mathrm{m^2\,s^{-1}}$ to $30 \times 10^{-11}\,\mathrm{m^2\,s^{-1}}$ for the ions is found. However, a significant gain in ion diffusion is only reached above an ACN mass fraction of $20\,\mathrm{wt}\,\%$. For lower concentrations, the amount of ACN appears to be too low to decrease ion-ion correlations and enhance the ion mobility. The diffusion coefficient of acetonitrile also follows this trend and rises from $6 \times 10^{-11}\,\mathrm{m^2\,s^{-1}}$ at $20\,\mathrm{wt}\,\%$ ACN to $100 \times 10^{-11}\,\mathrm{m^2\,s^{-1}}$ at $67\,\mathrm{wt}\,\%$ ACN.

## 6.3 Conclusions

In this chapter, mixtures of the ionic liquid EMIM $BF_4$ with different concentrations of acetonitrile in contact with nanoporous electrodes were investigated with MD simulations and accompanying CV experiments. This study should help to elucidate the role of the organic solvent on capacitance, pore composition and charging dynamics. Figure 6.11 displays snapshots of the pore region in the charge state at 1 V to accompany the following conclusions.

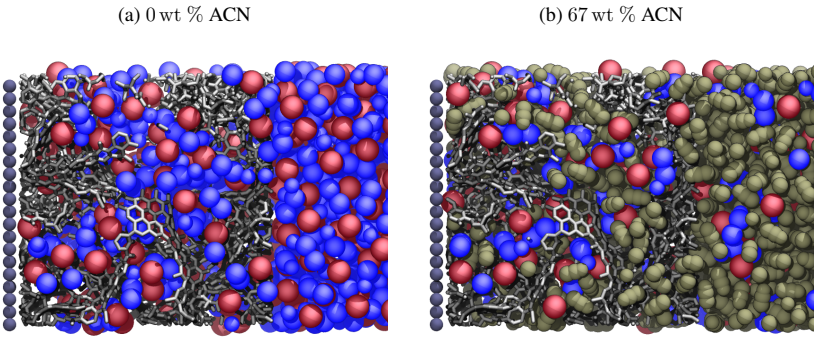


Figure 6.11: Pore snapshots of the positive electrode at 1 V, captured at the end of the simulation runs.

The simulation results showed that the capacitance (Fig. 6.3), the in-pore radial distribution functions (Fig. 6.7) and the charging time (Fig. 6.9) are only weakly affected by the change in acetonitrile concentration. However, number of in-pore ions (Fig. 6.4), charging mechanism (Fig. 6.5), particle coordination (Fig. 6.8) and diffusion coefficients (Fig. 6.10) clearly depend on the amount of ACN.

For the comparison of simulation and experimental data (Fig. 6.3), qualitative agreement for the integral capacitance was found, with an slight overestimation by the simulations, which is probably due to uncertainties of the CV experiments (shown by the

variation of the capacitance at different temperatures or cycle rates) and due to several necessary simplifications introduced in the particle models. In both methods, only small changes of the capacitance despite the large variation of ionic concentration was found. The robustness of the $g(r)$ data (Fig. 6.7) gives a starting point for the explanation of this concentration behavior. It shows that concerning the ions, no impactful structural transition is happening in the examined acetonitrile concentration range, either in the bulk or in the pore volume. This can be linked to the capacitance if the same is described as the interplay of ion separation and applied potential. To charge up the pore by a net difference in anion and cation numbers, ions have to break out of the prevailing ion structure. This means that the potential difference must overcome the energy change caused by the new, less favored structure. In time, the applied potential is negated by the arising excess charge in the pore until a final charged state is reached. The simulation data now shows that although absolute particle numbers change, the ion difference in the charged state of the pore remains constant for all acetonitrile concentrations. A possible facilitation of ion separation due to the solvent is not visible in the concentration behavior of the capacitance, because the potential difference is always sufficient to result in charge separation.

The diffusion analysis (Fig. 6.10) raises the question why the increased diffusion coefficients do not lead to an speed-up in charging time for higher solvent concentrations. Three aspects provide insight on this apparent contradiction: First, the diffusion is not calculated by particle paths directed into the pore (and therefore in direction of the charge migration). As the mean squared displacements only can give meaningful results for diffusion analysis in the periodic plane orthogonal to the migration direction, its influence on the charging time is limited to migration paths where the pore geometry requests this orthogonal translation. Second, it is unclear if diffusion even is the main factor that determines the charging time of the simulated system. At the interface between bulk and CDC pore, the dynamics are greatly affected by the electrical field caused by the electrode surface charge of the applied potential. Deep inside the

pores, the field is screened and ion migration is driven by self-diffusion. The size of the CDC sample in z-direction of $43.4\,\text{Å}$ (or about 7 times the ion diameter) might just be too small for a diffusion increase in migration direction to show its influence.

The charging mechanism (Fig. 6.5 undergoes a transition from ion exchange towards increased counterion adsorption for higher amounts of ACN. The case of pure RTIL is characterized by a large ionic density close to the carbon surface (Fig. 6.6). In this case, adding a counterion can be achieved by exchanging a co-ion, which requires to break the Coulombic cation-anion associations. The constant capacitance showed that there is no sign of an effect, where the change in solvent concentration reduces this associations such that the applied potential is now sufficient to break it and effectively increases the capacitance at a certain concentration. However, a reduction in ion coupling upon adding ACN still is expected and fits to the transition of the charging mechanism, which tends to be dominated by counterion adsorption at high ACN concentrations.

These results can be put into perspective of choosing an optimal ionic liquid based electrolyte for a EDLC with nanoporous electrodes. It has been showed that the ionic concentration of the EMIM $BF_4$ acetonitrile mixture does not affect much the capacitance up to the examined range of $67\,\text{wt}\,\%$ ACN or $1.51\,\text{mol}\,\text{L}^{-1}$. The choice of organic solvent and its concentration also affects two other important properties of the device, namely internal resistance (determined by the ionic conductivity) and the allowed operating voltage set by the chemical window of the substances. Using organic solvents allows for higher voltages ($\sim 2.7\,\text{V}$) than aqueous electrolytes ($\sim 1\,\text{V}$) [97], but the conductivity is reduced [98]. Going from a pure RTIL to a mixture with organic solvents increases the conductivity, but narrows the electrochemical stability window [99]. Therefore, the optimal choice of concentration will be a trade-off between conductivity and voltage limits [100, 101].

# 7 Simulating IL-based EDLCs with slitpore electrodes

Since MD simulations of models featuring complex pore networks like the CDC electrodes analyzed in Chapter 6 are computationally demanding, they are necessarily reduced in size compared to their experimental counterparts [85, 10]. For instance, the pore length in a typical simulation is tens of nanometers at best, while in the experimental systems the pores can be in the range of micrometers [102, 103]. Likewise, the size of the region between the electrodes is of the order of nanometers in simulations, but it is hundreds of micrometers or millimeters in real supercapacitors. The finite slitpore setup introduced in this chapter provides a good link between theoretical approaches and more material specific capacitor models like the CDC system. Because the complexity of amorphous pores is missing, it can be used to study the effect of ion confinement within a closed metallic pore under well defined conditions, neglecting any possible curvature and network character.

In MD simulations, the slitpores have to be connected to an electrolyte reservoir to study ion transfer and charging effects. In principle there are two possibilities to model such a system: In open pore geometries, both ends of the pores are connected to reservoirs, resulting in a dual-chamber setup for two electrodes. This setup has been studies by simulations for various interconnecting shapes like cylindrical tubes [95, 104–106] or slit systems [61, 107–109, 54, 110]. In contrast to that, the geometry used here is a closed system with radial terminations at the pore ends and a single reservoir between the pair of electrodes. To motivate the closed pore scenario, it is recalled that

nanoporous material benefits from narrow channels, where ion size and pore size are comparable [2]. Apart from the increase in specific surface area of the electrode material, reasons for this are packing effects and favorable electrostatic screening. The details of these effects are studied by altering the pore size in the electrode geometry. It should be noted that realistic pores are characterized by a pore size distribution and the advantages of small pores will be attenuated by partially inaccessible volume in the porous network.

## 7.1 Simulation setup

The simulation setup can be divided into the three components *pore geometry*, *ion model* and *applied potential*. Setting up the components involves many parameter choices, implementation of algorithms, utilizing external tools and validations. This will be described in detail in the following sections. Concerning the simulation output, most of the results like pore charge, capacitance, density profiles or charging mechanisms are calculated from time dependent densities $\rho_i(\vec{r}, t)$ of ion species $i$ obtained by the particle trajectories. The dependence of these observables on geometry parameters and applied voltage is key for the characterization of the systems.

### 7.1.1 Pore geometry

The pore parameters and geometry is displayed in Figure 7.1. In the following, the choice of fixed and variable parameters are motivated. In the simulations, a particle representation of fixed carbon atoms is used to build up the pore geometry, the centers of the carbon atoms are placed on the surface. This provides an atomic roughness of the surface as is necessary for the constant potential solver used in ESPResSo. A general rule for the parameter choices is to design the simulation cell as small as possible to gain computational efficiency and as large as necessary to avoid finite size effects.

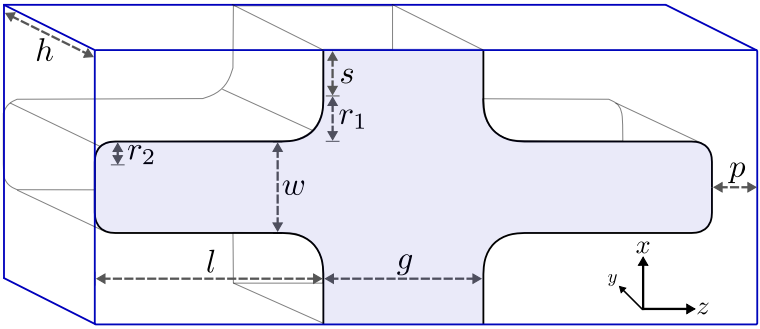


Figure 7.1: Schematic of the slitpore geometry with all relevant parameters.

Overall, the system consist of two mirrored, unconnected electrodes separated by a gap $g = 8\,\mathrm{nm}$. An additional gap $p = 0.15 \cdot L_z$ relative to the overall box size $L_z$ separates the pore tips of the periodic images in z-direction. Apart from the atomic carbon structure, the geometry is translationally invariant along the y-axis with box size $L_y = h = 2.5\,\mathrm{nm}$. The pore entrance and -bottom introduce two radii $r_1 = 4\,\text{Å}$ and $r_2 = 2\,\text{Å}$. These curvatures are used to avoid sharp angles which lead to spikes in the electric field. The rim size $s = 1\,\mathrm{nm}$ models the distance between the periodic images of the pore in x-direction. The parameters $g, p, r_1, r_2, s$ introduced so far are of minor importance and only part of the geometry validation in Section 7.2. The more interesting parameters are the pore length $l$ and width $w$ (sometimes referred to as the pore size). Reasonable values here are chosen with a fixed ion diameter $\sigma_{WCA} = 5\,\text{Å}$ in mind. Different values $l = 8\,\mathrm{nm}, 12\,\mathrm{nm}, 16\,\mathrm{nm}, 20\,\mathrm{nm}$ are used in various parts of the investigation so that a range of $16$ to $40$ particle diameters is covered. A value of $w = 9.37\,\text{Å}$ is used for all simulations targeting a narrow pore and values from $5.37\,\text{Å}$ to $30.37\,\text{Å}$ for the pore size parameter study. After subtracting the carbon diameter $\sigma_C = 3.37\,\text{Å}$, this covers the range from non-accessible pores to bulk-like pore sizes. Including all parameters, the total simulation volume is calculated as follows:

$$V_{tot} = h(gL_x + 4(lw/2 + (r_1 - \pi r_1^2/4) - (r_2 - \pi r_2^2/4))). \tag{7.1}$$

### 7.1.2 Ion model

For the most part, a primitive electrolyte model of symmetric, monovalent ions with WCA interaction is used. The full parameter list can be found in table 7.1. Although soft potentials are employed in the MD simulations, $\sigma_{WCA}$ is referred to as ion *size* or *diameter*.

| | $\sigma_{WCA}$ (Å) | $\epsilon_{WCA}$ (kJ mol$^{-1}$) | $r_{cut}$ (Å) | charge (e) |
|---|---|---|---|---|
| Cation | 5 | 1 | $2^{1/6}\sigma_{WCA} \approx 5.6$ | 1 |
| Anion | 5 | 1 | $2^{1/6}\sigma_{WCA} \approx 5.6$ | -1 |

Table 7.1: Interaction parameters used for the primitive ion model.

This choice is motivated by the following considerations: First, the simplicity of the model speeds up the simulations series which is important due to the huge set of parameters given by the pore geometry and applied potential range. Second, it is not trivial to distinguish between excluded volume effects due to the geometry confinement and effects resulting from ion asymmetry. This is helpful for later studies with more detailed ion models. Furthermore, in Chapter 8 the results of the MD simulations are compared to MC simulations using the same ions. It it known that asymmetry in charge and shape is one of the main criteria in the classification of ionic liquids. What is left in the model to still consider the electrolyte an ionic liquid are the size and the strong electrostatic interaction. In the simulation, this is controlled by the Bjerrum length $l_b = \frac{e^2}{4\pi\epsilon_0\epsilon_r k_B T}$, set by the relative permittivity $\epsilon_r$ and system temperature $T$. It combines two physical aspects which both appear as a factor in the Coulomb forces between the charges: Atomic and dipolar (orientation) polarization, which is not included in the model, leads to reduced Coulombic interaction. The same accounts for the addition of polar solvent molecules. In that sense, $\epsilon_r$ can also be used to model an *implicit solvent*. This leaves a rather broad range of meaningful values for the permittivity, resulting in different interpretations of the coarse grained electrolyte model. Reference

simulations with varying $\epsilon_r$ were analyzed in Section 7.3.1 and $\epsilon_r = 4$ was chosen for further simulations, motivated by the fact that lower values lead to reduced pore wetting without applied potential (see Section 7.3.1).

### 7.1.3 Canonical ensemble setup

For the NVT simulations and a given pore geometry with total volume $V_{tot}$, the volume fraction $\eta = \frac{V_{ion}}{V_{pore}}$ sets the number of particles in the system. However, the total volume of the system $V_{tot}$ differs from the accessible volume $V_{acc}$ which is unknown prior to the simulation and will depend on $\eta$ itself, the applied potential and pore geometry parameters. For example, if the pore width is too small for the ions to enter, a large portion of the total volume is no longer accessible, but may become available at a certain applied potential. Also, the volume fraction of the bulk liquid between the electrodes $\eta_{bulk}$ and that inside the slitpore $\eta_{pore}$ will both be different from $\eta$. It should be noted here that the region $z < l \cup z > l + g$ is referred to as *inside* of the pore. Again, a large range of values from $\eta = 0.15$ to $0.55$ was investigated in a first set of simulations at zero applied potential in Section 7.3.1. For further simulations, reduced sets of $\eta$ within this range are used.

Especially for nanopore charging dynamics, the temperature becomes important because of the diffusive nature of the co-ion desorption. However, we exclude the temperature $T$ and relaxation time $\gamma$ of the Langevin thermostat from the already large list of changing parameters and use fixed values of $T = 400\,\mathrm{K}$ and $\gamma = 10\,\mathrm{ps}^{-1}$.

### 7.1.4 Applied potential

A realistic setting of the capacitor system requires the modeling of an external, ideal voltage source. The ICC*-algorithm is employed to fulfill the boundary conditions of a fixed potential drop $U$ between the metal electrodes. This leads to time-dependent induced charges $q_i(t)$ on the discretized surface of carbon atom with index $i$. In Section 4.3.2, it was shown that ICC* actually only accounts for maintaining zero potential

difference between the electrode. To reach the target potential difference $U$, a time independent electric field $\vec{E}_{vac}(\vec{r})$ is superimposed that only has to be calculated once by solving the Laplace equation on a lattice for the given pore geometry.

### 7.1.5 Geometry generation

To avoid mismatch between the carbon particle positions and the lattice representation of $\vec{E}_{vac}(\vec{r})$, the following scheme is used to set up the system: First, the geometry is generated using *gmsh*, "a three-dimensional finite element mesh generator with built-in pre- and post-processing facilities" [111]. The surface is parametrized by its outline and extruded by $h$ in y-direction (see Fig. 7.1). Out of this surface, *gmsh* uses a "frontal" algorithm [112] to generate a mesh of triangles with side lengths close to a given value $c_l$. Later, the carbon atoms are placed in the centers of these triangles, so the choice of $c_l = 2.9\,\text{Å}$ will lead to a carbon-carbon distance of $a_{CC} = c_l/\sqrt{3} \approx 1.67\,\text{Å}$ considering equilateral triangles. The output of *gmsh* is a stl-file, which is a set of $N_T$ triangles $T_i$, given by three vertices in clockwise orientation and the corresponding normal vector. This data is imported into ESPResSo, which now has two tasks: First, placing the fixed carbon particles in the triangle centers and assigning the triangle area and normal vector to the particle, needed for the ICC* algorithm. Second, the vacuum field $\vec{E}_{vac}(\vec{r})$ is pre-calculated by solving Laplace's equation in the whole volume of the system (see Section 7.1.7).

### 7.1.6 Surface distance calculation

For a straightforward implementation of the Laplace solver with a volume grid, it has to be known if a finite volume element belongs to vacuum or the electrode boundary. This can be done by the distance criteria

$$|d_S(\vec{r})| < \epsilon_b \tag{7.2}$$

given the distance $d_S$ to the surface from any point $\vec{r}$ in space and a threshold $\epsilon_b = 0.25$ Å in a lattice with a resolution of 10 bins per Å. $d_S$ is found in by simply calculating the distance $d_{T_i}$ to each triangle and using $d_S = min(d_{T_i}), i \in N_T$. It is worthwhile to outline the implementation of the distance calculation [113]: First, the closest feature has to be determined. This feature can be one of the three edges ($E_1$, $E_2$, $E_3$), vertices ($A$, $B$, $C$) or the face $F$ of the triangle (see Fig. 7.2).

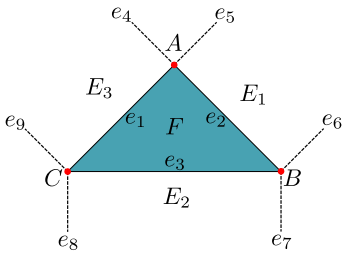


Figure 7.2: Triangle features and edge equations in 2D.

This is most easily done in 2D, so two matrices $T_s$ and $T_r$ for translation and rotation for each triangle are used that it ends up on the yz-plane with one vertex in the origin of the coordinate system. The same transformations applied to the test point leads to the transformed point $\vec{t} = T_r T_s \vec{r}$ and the projected point $p = (t_z, t_y)$. The nine edge equations

$$e_i(p) = (p_x - X) \cdot dY - (p_y - Y) \cdot dX \tag{7.3}$$

with gradient $dX/dY$ and a point $(X, Y)$ on $e_i$ can be used to test a given point $p$. The cases

$$e_i(p) \begin{cases} > 0 & p \text{ is left of } e_i \\ < 0 & p \text{ is right of } e_i \\ = 0 & p \text{ is on } e_i \end{cases} \tag{7.4}$$

determine the location of $p$ relative to the edge. With a minimal set of evaluations of the edge equations, the closest feature of the test point can be determined and the distance

to that feature is calculated. Single pre-calculations of the transformation matrices and edge equations parameters for each triangle further speed up the implementation.

### 7.1.7 Laplace solver

The preceding distance calculations is required to determine the boundary nodes for the Laplace solver. A 7-point stencil successive overrelaxation scheme is used to converge to the solution $\Phi(\vec{r})$ of the Dirichlet problem

$$\begin{aligned} \Delta\Phi(\vec{r}) &= 0 \text{ in } \Omega \\ \Phi(\vec{r}) &= \phi_1 \text{ on } \partial\Omega_L \\ \Phi(\vec{r}) &= \phi_2 \text{ on } \partial\Omega_R \end{aligned} \tag{7.5}$$

in the accessible domain $\Omega$ with the electrode surfaces $\partial\Omega_L$ and $\partial\Omega_R$. In the discrete solver, the box $L_x, L_y, L_z$ is divided into an irregular lattice with a given number of bins $b_x, b_y, b_z$ and lattice spacing $\Delta x = \frac{L_x}{b_x}, \Delta y = \frac{L_y}{b_y}, \Delta z = \frac{L_z}{b_z}$. The iteration rule runs over all bins $(i, j, k)$ and reads as

$$\begin{aligned} \Phi_{ijk} = (1-\alpha)\cdot\Phi_{ijk} + \frac{\alpha}{2\cdot(\Delta y^2\Delta z^2 + \Delta x^2\Delta z^2 + \Delta x^2\Delta y^2)}\cdot \\ (\Delta y^2\Delta z^2\cdot(\Phi_{i+1jk} + \Phi_{i-1jk}) + \\ \Delta x^2\Delta z^2\cdot(\Phi_{ij+1k} + \Phi_{ij-1k}) + \\ \Delta x^2\Delta y^2\cdot(\Phi_{ijk+1} + \Phi_{ijk-1})) \end{aligned} \tag{7.6}$$

Note that the updated values are already used during one iteration step, the boundary nodes are excluded and periodic boundary conditions are applied for neighbor bins at the box borders. Fast convergence is obtained for a relaxation parameter $\alpha = 1.9$. The stopping criterion is fulfilled if the maximal absolute change of any $\Phi_{ijk}$ between two iteration steps is below $10^{-7}$.

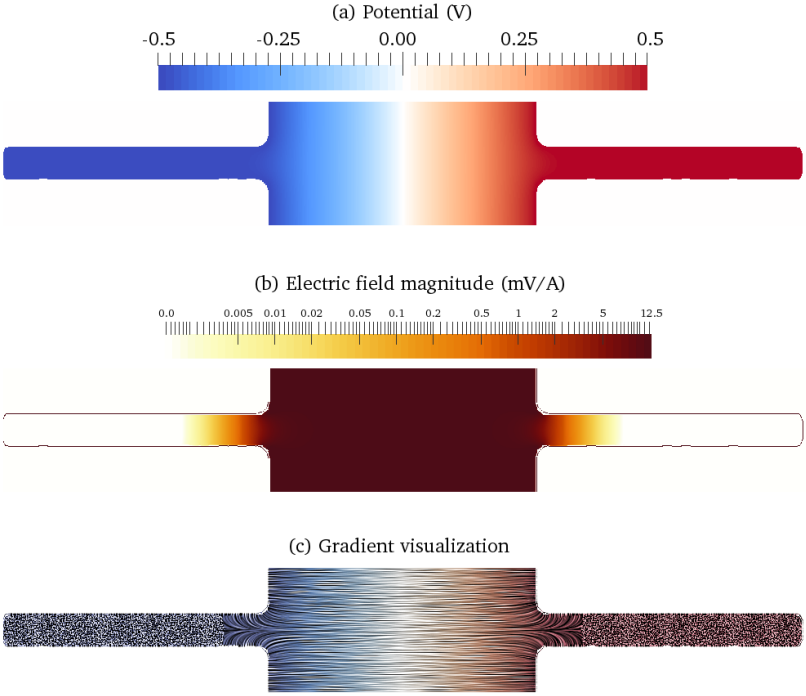


Figure 7.3: Exemplary potential map, electric field magnitude and gradient visualization of the slitpore geometry.

An exemplary electric potential map, electric field magnitude and gradient visualization is shown in Figure 7.3 for a potential $U = 1.0\,\mathrm{V}$. An important observation here is that the potential in Fig. 7.3 (a) inside the pores is almost constant and the potential drop appears in the reservoir between the electrodes. This is also visible in the magnitude of the electric field Fig 7.3 (b), where the values approach zero in the pore entrance region and have a constant value of $E = U/g = 12.5\,\mathrm{mV\,\AA^{-1}}$ between the electrodes. The field lines in Fig. 7.3 (c) are visualized with a *Line Integral Convolution* available in Paraview. In the regions of constant potential inside the pores, the visualization is no longer possible because the magnitude of local field vectors drops

below the precision of the gradient visualization, resulting in noise data in the rear part of the slitpore in Figure 7.3 (c). As expected, the field lines end up perpendicular to the surface and follow the curvature of the geometry. The potential data only has to be calculated once per geometry, any applied potential drop can be achieved by rescaling the existing data. It is used in ESPResSo as a *tabulated potential* with linear interpolation for the potential values at the actual particle positions. The gradient and resulting force $\vec{F}_E = q_i \cdot \vec{E}_{vac}(\vec{r})$ on the charge $q_i$ is computed on the fly during the simulation.

### 7.1.8 Testing the applied potential method

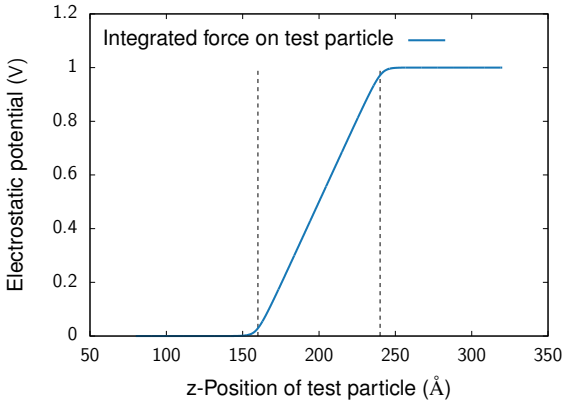


Figure 7.4: Electric potential of a test charge dragged along the z-axis from one electrode to another.

In order to test the applied potential scheme, a charged particle is dragged from one pore center to the other with activated ICC* and a superimposed potential of $1\,\mathrm{V}$. The resulting potential along the z-direction

$$\Phi(z) = -\int_{z_1}^{z_2} F_z dz$$

is shown in Figure 7.4. The pore entrance positions at $z = 160\,\text{Å}$ and $z = 240\,\text{Å}$ are marked by dashed lines. As expected, the potential inside the pores is constant and the drop occurs in the reservoir between the electrodes. This confirms the validity of the superimposed potential and the resulting forces.

## 7.2 Finite size test

Too small system sizes may lead to results that are affected or even dominated by finite size effects. However, excessive testing of how the results converge for all geometry parameters is out of scope. Nevertheless, some of the critical parameters are checked for altered results. In particular, discretization of ICC* particles, gap size $g$ and side length $h$ (see Fig. 7.1), which also set the reservoir volume, are tested. Also related to the number of particles in the reservoir is the rim size $s$. It determines the distance of the periodic images of the pore in x-direction and one edge of the plane which embeds the pore. Ions and induced charges total in a neutral pore, so the influence of the periodic replica of the pore in x-direction is expected to be minor.

### 7.2.1 ICC* discretization

Considering a test charge approaching a metal plane, the attractive force of the induced charges acts only in the normal direction of the plane. This changes when going from the continuum picture to a discretized surface. There, the off-normal contributions increase with closer approach of the test charge. In the CDC electrode model, the smeared-out character of the induced charge in a metal surface was taken into account by using Gaussian charge distributions for the induced charges on the carbon atoms. In ESPResSo, electrostatic interaction between point charges and Gaussian charges is not possible. However, comparing the ion size of $5\,\text{Å}$ with the carbon-carbon distance of $1.67\,\text{Å}$, the effect is expected to be negligible.

The surface discretization is tested in several ways: First, we perpendicularly approach the surface with a test charge and measure the attractive force that appears due to charge induction. We compare the cases where the test charge is (i) moved directly towards a carbon atom or (ii) towards the center of a carbon ring.

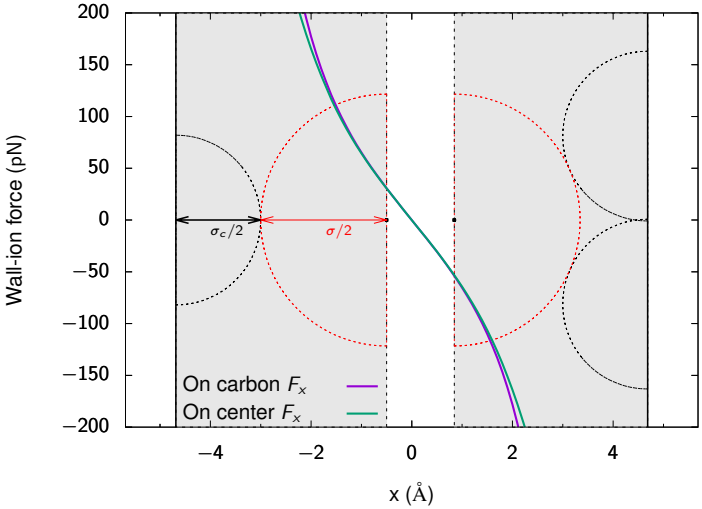


Figure 7.5: Wall-particle forces of the discretized surface, probed at the two representative positions (on carbon and on center) of the slitpore carbon structure.

Figure 7.5 shows the force component $F_x$ of the image charge attraction perpendicular to the surface in both cases. The curves are very similar and only deviate significantly about $1\,\text{Å}$ away from the pore center. This has to be put into perspective to the *accessible* region of the ions. This is denoted by the semicircles and gray areas, showing the onset of the WCA potential between ions and carbon atoms. In case (i), the WCA interaction starts at $\frac{w}{2} - \frac{\sigma_c+\sigma_{ion}}{2} = 0.505\,\text{Å}$ away from the pore center, whereas in case (ii), WCA begins at $\frac{w}{2} - \sqrt{(\frac{\sigma_c+\sigma_{ion}}{2})^2 + a_{CC}^2} \approx 0.845\,\text{Å}$ for all six particles of the hexagon. Note that in these force tests, the particle is moved symmetrically between carbon centers or ring centers on both sides of the pore, the asymmetry in the

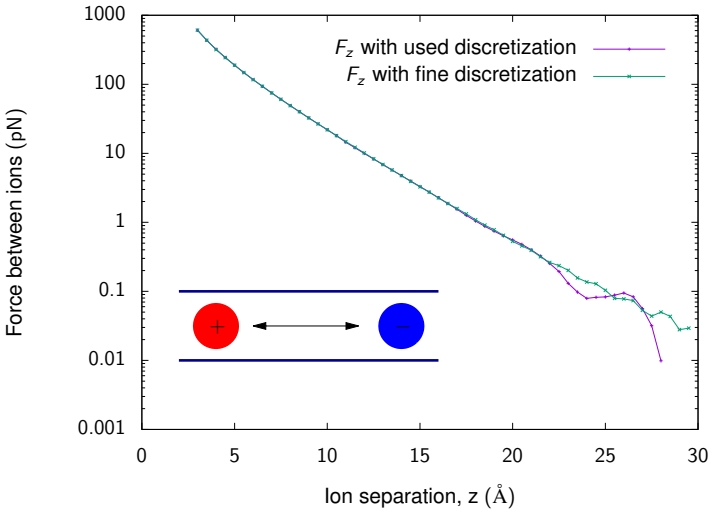


Figure 7.6: Force on an ion pair with refined and applied ICC discretization.

illustration is for direct comparison of (i) and (ii). From this test it can be concluded that the discretization level is sufficient to resolve correct normal forces by the induced charges. However, it also shows that in the graphene ring centers, the image charge attraction is slightly increased compared to the on-carbon position.

It is further tested how the ICC* discretization affects the electrostatic interaction of an ion pair inside the pore. Therefore, a refined carbon mesh of half the size of the lattice vectors is generated resulting in a carbon-carbon distance of $a_{CC} \approx 0.84\,\text{Å}$. The electrostatic forces on a pair of test charges separated by $z$ for the refined and applied (more coarse) discretization are compared in Figure 7.6. In both cases, the forces are slightly affected by the relative position of the ions to the carbon structure. The oscillatory contribution to $F_z$ by the induced charges starts to overcome the ion-ion coulomb force after $21\,\text{Å}$ for the coarser carbon structure. In case of a filled pore, this contribution will be small regarding average distances and number of ions.

### 7.2.2 Gap size

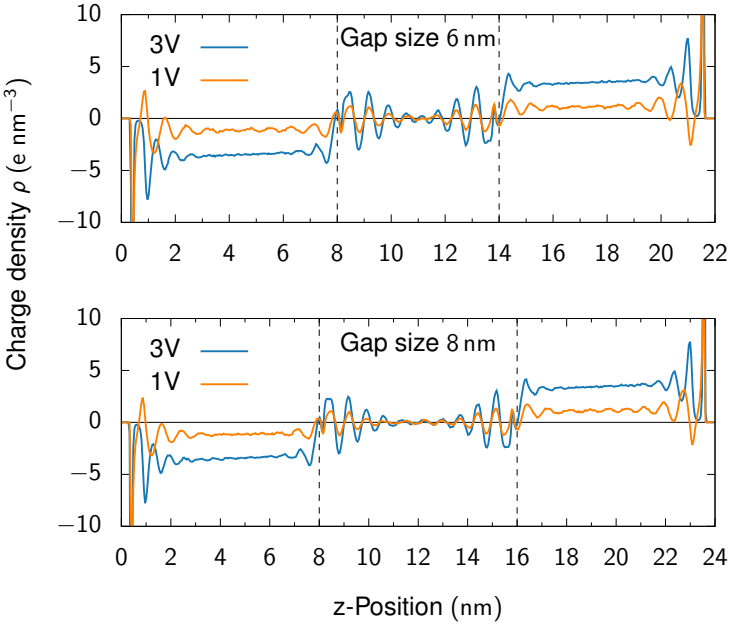


Figure 7.7: Total number density for reduced and applied gap sizes $6$ and $8\,\mathrm{nm}$.

For the production runs, the system is simulated with a gap size $g = 8\,\mathrm{nm}$ between the two pores. This region models the bulk electrolyte in EDLCs and extends to $\mu\mathrm{m}$ or $\mathrm{cm}$ in real capacitor applications. These distances are necessary to avoid possible short circuits in case of mechanical deformations. For the same reason, a permeable separator is embedded between the electrodes in the center of the reservoir. In the simulations, the bulk region is kept as small as possible to minimize the computational effort. The electrode separation should be chosen such that the charge density oscillations at the electrodes have decayed and there is no interference of the interfacial ion layers. The amplitude of these oscillations and the number of layers $N_l$ depends on the ion model

and the applied voltage. Based on previous simulations, $N_l < 6$ holds also for high applied voltages. This gives an estimate for the lower limit of the gap size for $N_l = 6$ and $\sigma_{ion} = 5$ Å, assuming that each layer width is equal to the ion diameter:

$$g > 2N_l\sigma_{ion} = 6\,\mathrm{nm}. \tag{7.7}$$

The influence of $g$ on the ion structure is tested in a series of simulation with an applied voltage range of $0\,\mathrm{V}$ to $5\,\mathrm{V}$. Exemplary, Figure 7.7 shows the ion charge density profiles along the z-direction for the lower limit of the gap size, $g = 6\,\mathrm{nm}$ and the applied gap size $g = 8\,\mathrm{nm}$, for $1$ and $3\,\mathrm{V}$ respectively. In between the electrodes, marked by the vertical dashed lines in Fig. 7.7, the charge density shows pronounced oscillations for both applied voltages. In case of the smaller gap size $g = 6\,\mathrm{nm}$, the oscillation cannot be considered as decayed in the bulk. With the increased value of $g = 8\,\mathrm{nm}$, there is almost no structure left in the center of the system. Also, the subsequent simulations for different initial volume fractions, which strongly affect the situation in the bulk, will show that the pore charge is unexpectedly decoupled from the bulk configuration.

### 7.2.3 Side length

In the periodic y-direction of size $h$, the ion layers may not be able to decorrelate over $h$ and the resulting structure will be affected by the choice of the side length and the ratio $\frac{h}{\sigma_{ion}}$. The ion arrangement along the z-direction inside the pore exhibits structural changes from strongly confined at the pore ends to a less dense, homogeneous ion distribution in the pore center. The influence of the side length $h$ is expected to be smaller in the latter case, where the thermal noise will decorrelate the ions in y-direction also for small values of $h$. Test simulations with side lengths $h = 2.5\,\mathrm{nm}, 5\,\mathrm{nm}, 10\,\mathrm{nm}$ at $1\,\mathrm{V}$ were set up to rule out a major influence on global system observables, in this case the time dependent capacitance per area.

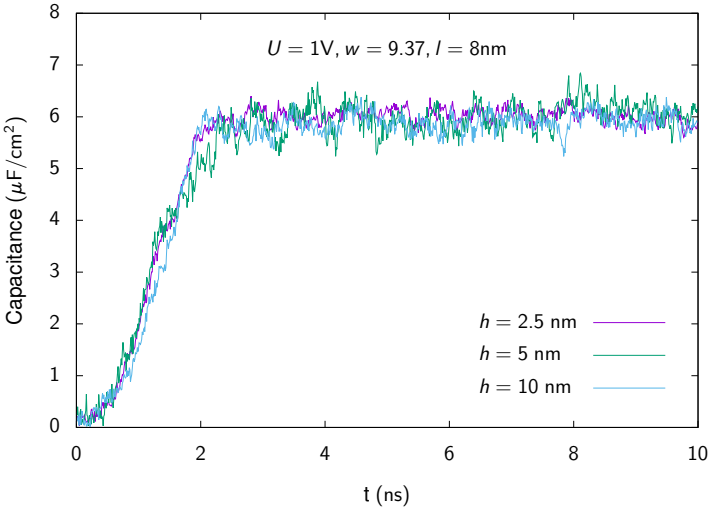


Figure 7.8: Time evolution of the specific capacitance for various side lengths.

Figure 7.8 shows $C(t)$ for the different side lengths $h$ and common parameters stated at the top of the plot. A detailed discussion of the charging dynamics in the slitpore setup will be discussed in Chapter 9 in more detail.

For the finite size analysis, the influence of $h$ on the final charged state of the capacitor is evaluated. The test simulations show that the saturated capacitance, averaged from $4\,\text{ns}$ to $10\,\text{ns}$ is not affected by the side length:

$$h = 2.5\,\text{nm} : \langle C \rangle = (6.36 \pm 0.31)\,\mu\text{F}\,\text{cm}^{-2}$$
$$h = 5\,\text{nm} : \langle C \rangle = (6.27 \pm 0.21)\,\mu\text{F}\,\text{cm}^{-2}$$
$$h = 10\,\text{nm} : \langle C \rangle = (6.38 \pm 0.17)\,\mu\text{F}\,\text{cm}^{-2}$$

Because $h$ is also directly proportional to the number of particles in the bulk, the smallest value $h = 2.5\,\text{nm}$ of the parameter series is most convenient for comprehensive simulations with a large number of parameters.

## 7.3 Results

Any applied voltage between the electrodes induces charge and mass transport. This changes the balance between bulk, anode and cathode and leads to a distinct ion distribution across the system. The simulations show that relaxation times towards a charged state can be slow and that the bulk density will change during the charging process. This section starts with an investigation of the initial pore wetting at $0\,\mathrm{V}$ (Sec. 7.3.1), discusses how the bulk density affects the pore charge (Sec. 7.3.2) and how to avoid out of equilibrium states during charging (Sec. 7.3.3). These issues can be seen as part of the equilibration process but also reveal interesting aspects of the system. With the charging process well under control, the systematic influence of the pore width on the integral capacitance is discussed in Section 7.3.4.

### 7.3.1 Pore wetting

Two important parameters of the electrolyte model are the permittivity $\epsilon_r$ and initial electrolyte volume fraction $\eta$, which are well defined in simulations: The permittivity enters in the Bjerrum length and inversely scales the strength of the coulomb interactions in the system. In experiments, it is accessible as the zero-frequency relative permittivity. $\eta$ sets the number of particles in the system of a given volume and corresponds to the pressure inside the capacitor. Because $\epsilon_r$ and $\eta$ can be tuned by the composition of the electrolyte and the ambient conditions of the EDLC cell, simulations for $\epsilon_r$ from $2$ to $10$ and for $\eta$ from $0.24$ to $0.5$ at zero voltage were performed. By inspection of the density profiles $\rho(z)$ across the simulation box, the system is characterized by one of the four states (a) *non-wetting*, (b) *incomplete wetting*, (c) *full wetting* and (d) *bulk crystal* depending on the values of $\epsilon_r$ and $\eta$. Figure 7.9 shows snapshots of typical configurations for the different states.

Within the described simulation setup, several other factors can influence the initial pore wetting behavior. Due to the large parameter space, these effects were not simu-

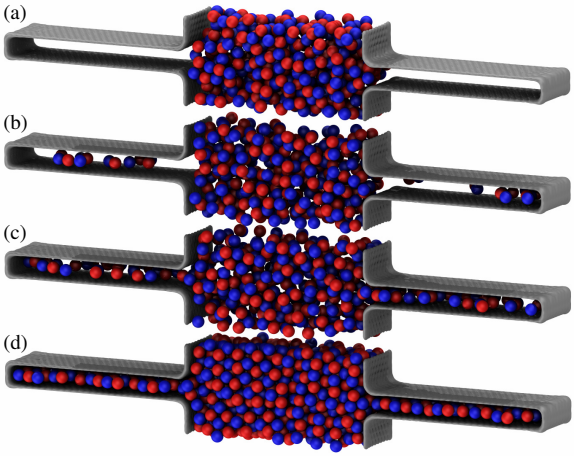


Figure 7.9: Exemplary snapshots of the different pore wetting classes: (a) non-wetting, (b) incomplete wetting, (c) full wetting and (d) bulk crystal.

lated systematically, but are only briefly discussed below:

- Additional short-range attraction via Van-der-Waals interaction between the ions and the electrode particles locally binds the ions on the surface. Note that this effect is neglected here and the purely repulsive WCA interaction is applied. This approach can be used to simulate ionophilic pores.
- The temperature of the canonical ensemble controls the aggregate state of the IL. Meaningful values for simulations should be well above the melting point of the electrolyte, but in applicable range considering the use of EDLC cells in electromobility applications.
- Unstructured (i.e. smooth) electrodes reduce the friction and increase the ion mobility in the confined parts of the system. This variation of the electrode model is investigated in Section 5.2.2 for parallel plate capacitors.

- Larger pores (in terms of pore width $w$) lead to an improved pore accessibility, but also negatively affect the capacitance as shown later in section 7.3.4.
- The capacitive response of the system is the pore occupation as a function of the applied voltage. The question how the voltage behavior is affected by the initial volume fraction is further discussed in Section 8.4

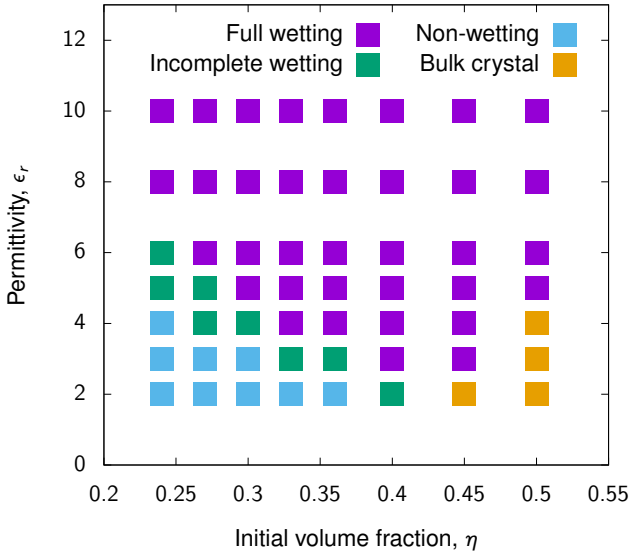


Figure 7.10: Classification of the pore wetting behavior depending on initial volume fraction and electrolyte permittivity.

56 pairs of values of $\eta$ and $\epsilon_r$ are simulated and categorized in the states (a) to (d). The result is condensed in the phase diagram in Figure 7.10. The data shows that the parameters are influencing the pore filling behavior in a similar fashion: For low values of $\epsilon_r$ in the range of $2$ to $6$ (i.e. increased electrostatic interaction) and a large range of volume fractions from $0.24$ to $0.4$, the particles tend to leave the pore unfilled. This resembles the low vapor pressure character of RTILs, where the strong ionic bonding

prevents the transition into the gas phase at the IL surface. Accordingly, high values for the permittivity reduce the electrostatic ion-ion correlation and improve the pore wetting. The pore filling can also be enhanced by increasing the initial volume fraction which expands the IL drop in the bulk and pushes the ions into the pores. The data shows that for $\eta > 0.4$, the pore is either in the fully wetted or bulk crystal configuration. At high values of $\eta$ and low $\epsilon_r$, the systems freezes and forms a highly ordered salt crystal in the bulk. In this configuration, the immobility of the ions will lead to a poor performance of the capacitor, which relies on particle transport into and out of the pores.

### 7.3.2 Bulk calibration

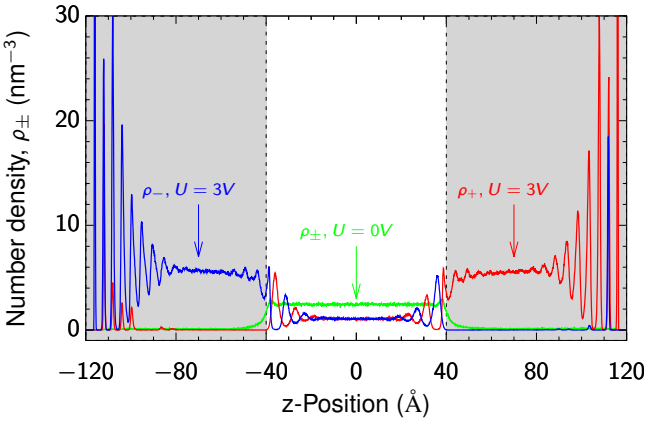


Figure 7.11: Pore ion structure showing co-ion trapping and density reduction in the bulk with applied voltage.

With applied voltage, ion migration leads to a change in density in the reservoir and the pores. This is demonstrated in Figure 7.11, showing the particle number density along the z-direction of the system with *incomplete wetting* initial conditions for $0\,\mathrm{V}$ (green)

and 3 V (blue, red) for a total concentration of $c_{\mathrm{IL}} \approx 1.1$M corresponding to the initial volume fraction $\eta = 0.24$. The gray areas denote the location of the pores. Leaving aside the discussion of structural features for now, it is observed that the density of ions in the bulk electrolyte between the electrodes strongly depends on the applied voltage. Quantitatively, the bulk density drops almost twofold upon charging.

Depending on the initial configuration at zero voltage and the dominating charging mechanism, the bulk density will increase for co-ion desorption or decrease for counterion adsorption when a voltage is applied. A detailed analysis of the charging mechanism follows in Section 8.5.

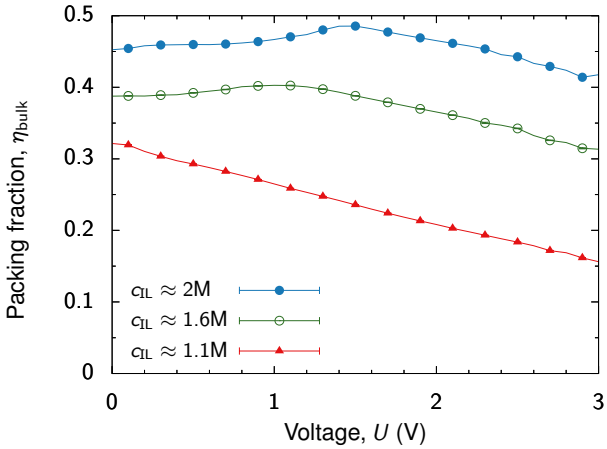


Figure 7.12: Bulk packing fraction upon charging for different initial concentrations.

Figure 7.12 shows the described behavior of the bulk packing fraction as a function of voltage. Each data point represents an individual simulation at the given applied voltage where the bulk density has been sampled after completion of the charging process. The packing fraction curve for $c_{IL} = 1.1\,\mathrm{M}$, for which Fig. 7.11 showed the density profile, drops twofold in a linear fashion from $\eta_{bulk} = 0.32$ at 0 V to $\eta_{bulk} = 0.16$ at 3 V. To test if this effect affects the pore charge, a simulation approach that main-

tains the density in the bulk is used. Dynamically moving the pore constraints conflicts with the constant potential simulation scheme, as the applied field would have to be recalculated with every translation of the boundaries. Using a larger bulk region would increase the computational cost. Here, a Monte- Carlo like approach is applied, where ion pairs are dynamically inserted and deleted in the bulk to maintain the density until the charging process has finished. This correction move is executed every $0.1\,\mathrm{ns}$ and disabled after the pore charge has converged. Also, an insertion move is rejected if the change in total energy exceeds $10\,\mathrm{kJ\,mol^{-1}}$ to avoid strong particle overlap. This approach is considered as part of the equilibration process and can't be employed to obtain dynamical properties. The data acquisition happens after the bulk correction is switched of in the charged state.

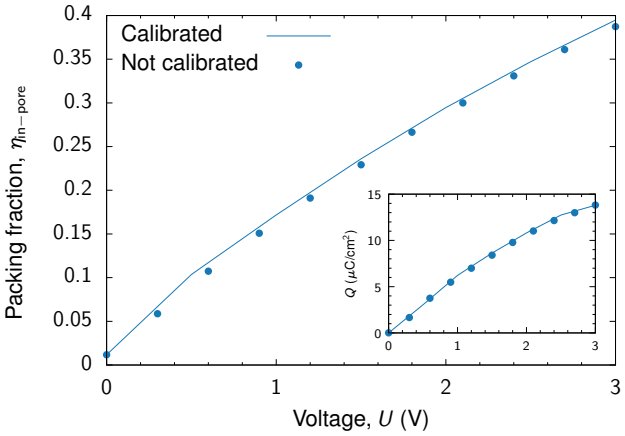


Figure 7.13: Pore packing fraction and charge density (inset) with and without bulk calibration.

Figure 7.13 compares the pore packing fraction and charge (inset Fig. 7.13) with and without bulk calibration. It reveals that although the packing fraction in the pore is slightly altered by the bulk calibration, it has practically no effect on the charge storage.

This is likely because a change in the chemical potential $\Delta\mu_{\pm}$ due to the change in the ion density is small compared to the energy of the applied potential, i.e., $\Delta\mu_{\pm} << eU$.

### 7.3.3 Ramp charging

The voltage in constant potential simulations is usually switched on after a certain time of system equilibration at $0\,\mathrm{V}$. For higher applied potentials, this approach led to irregularities in measurements of the pore charge, where repeated simulation runs with same system parameters resulted in different pore charges.

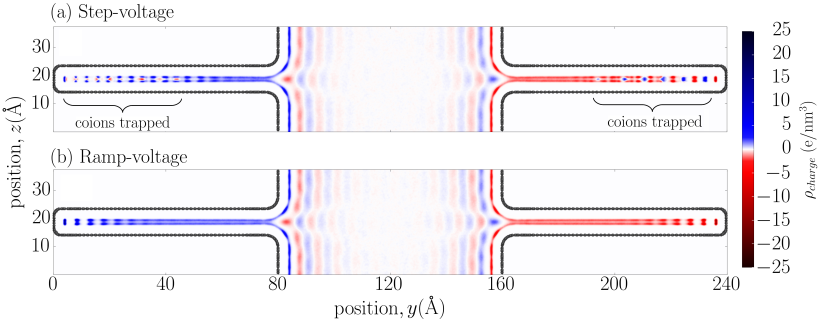


Figure 7.14: Charge density heatmaps for the sudden application of an applied voltage (a) and a linear voltage ramp (b). The same final voltage of $3\,\mathrm{V}$ is applied in both cases, averages for the heatmap generation were obtained for the last $5\,\mathrm{ns}$ simulation time. The difference in final ion configuration indicate that the step-voltage approach has not reached a steady state yet.

The density profiles in Figure 7.11 as well as the charge heatmap in Figure 7.14 (a) show that with larger applied voltages ($\sim 3\,\mathrm{V}$), co-ions in the pore can temporarily become trapped near the pore end on time scales reached with the MD simulations ($\sim 100\,\mathrm{ns}$). Such a co-ion trapping leads to a decreased charge storage and slowed down dynamics. A way to avoid ion trapping is to use a linear voltage ramp $U(t) = kt$ to charge the system until the target voltage is reached, instead of applying the final voltage in a step-like fashion. Figure 7.14 (b) demonstrates that this strategy avoids co-

ion trapping and leads to a charge equilibrated pore configuration on computationally accessible time scales. The detailed analysis of this approach and extended simulations with various sweep rates $k$ will be addressed in Chapter 9.

### 7.3.4 Oscillating capacitance

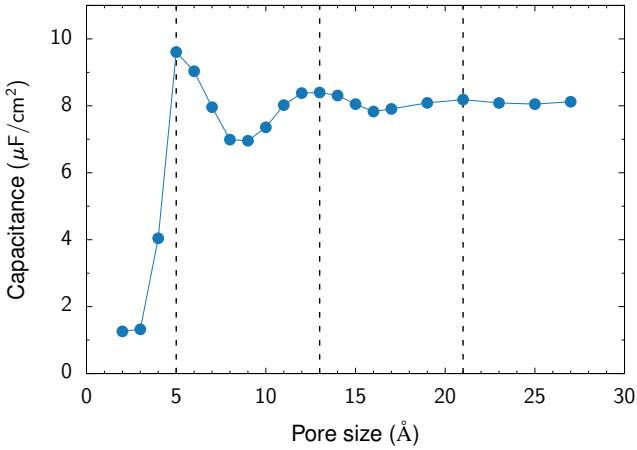


Figure 7.15: The integral capacitance exhibits oscillating behavior for increasing pore size. The dashed vertical lines indicate pore sizes that lead to local maxima in the capacitance. A global maximum is found if the pore size matches the ion size.

In this simulation series, the pore size $w$ is varied in a range from $3\,\text{Å}$ to $27\,\text{Å}$. With ions of diameter $5\,\text{Å}$, the lower limit covers the situation of too narrow pores. In the upper limit, the system converges towards a setup with completely flat electrodes. The pore size $w$ is of interest for EDLCs, as available technology allows to fabricate high surface area electrode material with a narrow pore size distributions [11]. The data in the following Figures 7.15, 7.16 and 7.17 was simulated with $\eta = 0.27$, $\epsilon_r = 4$ and an applied voltage of $1\,\text{V}$ without bulk calibration. Figure 7.15 shows the pore size

dependence of the integral capacitance

$$C(w) = \frac{1}{AU}\left\langle \sum_i q_i \right\rangle \tag{7.8}$$

per (single) electrode surface area $A$ calculated from the sum over all ICC particles $q_i$ and averaged over both electrodes in the charge state of the capacitor. For narrow pores smaller than the ion size, the capacitance still has a small contribution from the rim of the pore that offsets the complete data set by $1.3\,\mu\mathrm{F\,cm^{-2}}$. For $w >= \sigma_{ion}$, the capacitance exhibits three distinguishable oscillations in the simulated range of pore sizes. In this range, the capacitance ranges from the global maximum of $C(w) \approx 9.6\,\mu\mathrm{F\,cm^{-2}}$ at $w = 5\,\text{Å}$ to the local minimum of $C(w) \approx 6.9\,\mu\mathrm{F\,cm^{-2}}$ at $w = 7\,\text{Å}$. The capacitance oscillations are often explained with the analogon of constructive and destructive interference of ion layers [54]. It is true that one layer of co- and counterions each would result in a neutral pore, leading to zero capacitance. The interference picture however neglects that the true configuration is found in the free energy minimum governed by excluded volume, electrostatics and driving forces into the confined region, which cannot be captured by simple additive superposition of densities of single-wall solutions.

Another important observation is that the global maximum in capacitance can be found if the pore size is equal to the ion size (at $5\,\text{Å}$). This can be explained by the *superionic state*, described in Section 4.2: If ions are surrounded by metallic boundaries, the interaction between themselves is screened exponentially considering the unity of an ion and its image charges. This effect gets weaker if the pore size increases. As a result, it is possible to pack more like-charged ions inside the narrow slitpore up to the point, where the pore is to small for the ions to fit in.

### 7.3.5 Ion structure with varying pore size

The series of density profiles in Figure 7.16 shows the development of the ion configuration across the pore width. The configurations associated with the local maxima

of the capacitance are highlighted with bold colors. If the pore is filled with a single counterion layer at $w = 5\,\text{Å}$, the capacitance has a global maximum. As the pore becomes wider, charge oscillating ion layers are emerging comparable to ILs at planar electrodes. Figure 7.16 also shows that the outermost layers are always made up of counterions. This leads to the rule that the maxima in capacitance appear if the number of internal layers $n$ in x-direction is an odd number, for the pore size this suggests $w_n^{opt} \leq n \cdot \sigma_{ion}$ for $n = \{1, 3, 5, \ldots\}$. Shifted stacking of the spherical ions undermines this rule, generally the characteristic width of ion layers has to fit into the given pore geometry. This structure results in maximal packing of ions and thus maximal induced charge, any disturbance reduces the capacitance.

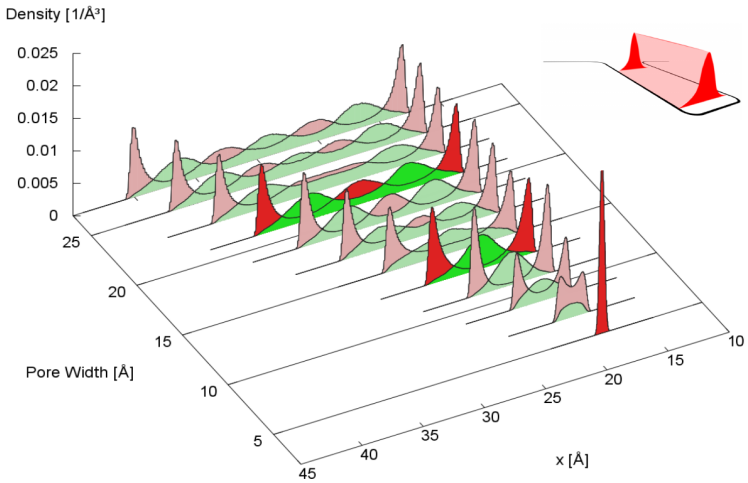


Figure 7.16: Ion number density profiles for various pore sizes across the pore (red: counterions; green: co-ions). The bold slices are the configurations at local capacitance maxima.

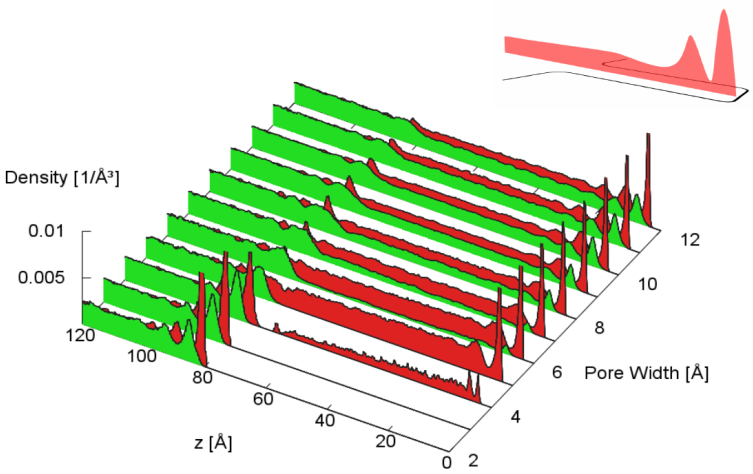


Figure 7.17: Ion number density profiles for various pore sizes along the pore (red: counterions; green: co-ions).

In the density along the pore in Figure 7.17, ions at the bottom of the pore also show charge density oscillations like ILs at planar interfaces, although highly confined. For wider pores, the oscillations become more pronounced. After the ion layers at the pore ends, the density in z-direction appears homogeneous up to the pore entrance, where another layered structure emerges due to the pore cover. At a pore size of $4\,$Å, some counterions are still able to squeeze inside the pore because of the soft interaction potential. For values $w < 4\,$Å, the pore becomes inaccessible for the ions.

## 7.4 Conclusions

Concerning the geometry parameters of the slitpore electrode system, tests for the degree of discretization of the carbon particles, the size of the reservoir and the side length of the slitpore show no signs off finite size effects for the chosen parameters used in subsequent simulations. However, the parameters of the model electrolyte strongly affect the system: The pore wetting analysis shows that the initial configuration and density in the pore at zero volt is highly determined by the permittivity and initial volume fraction of the electrolyte. These parameters contribute to the overall ionophobicity of the pores.

The ion density $\rho_{\mathrm{bulk}}$ between the electrodes of a supercapacitor can vary appreciably with the applied voltage. This can be corrected by calibrating $\rho_{\mathrm{bulk}}$ during equilibration runs to keep it constant. However, this change in the bulk density only has a minor effect on the charging behavior. This result means that it is safe to consider relatively small electrode-electrode separations in supercapacitor models, also the computationally expansive bulk calibration only has a small impact on the pore charge. Another important issue that appeared in the validation of the setup is that at intermediate and high voltages, co-ions can become trapped in the pores on typical simulation time scales, producing non-equilibrium states. This difficulty is resolved by charging the capacitor using a linear voltage-ramp instead of an abrupt step-voltage.

For varying pore size, the capacitance exhibits oscillations with a global maximum when ion diameter and pore sizes match. This clearly shows that it is important to choose an adapted combination of electrolyte and electrode material, preferably with a narrow pore size distribution close to the ion size. Usually, the anion and cations in ILs are different in molecular structure and extent, so that the pore size has to be tuned with respect to the larger ion for symmetric electrodes. If the polarity of the capacitor is fixed, asymmetric electrodes could be used, individually optimized for the respective counterion.

# 8 Finite pore length effects

Parts of the content in this chapter has been published in the following article. My contributions: Performed MD simulations, figures and snapshots, data analysis and parts of the writing. The Monte-Carlo results of this chapter were produced by Dr. Svyatoslav Kondrat.

**K. Breitsprecher**, M. Abele, S. Kondrat and C. Holm
"The effect of finite pore length on ion structure and charging"
*The Journal of Chemical Physics*, **2017**, 147 (10), p 104708
URL: https://doi.org/10.1063/1.4986346

The finite slitpore simulation model (hereafter called *MD model*) introduced in Chapter 7 represents a simplified building block of a macroscopic nanoporous network such as CDCs, which consist of interconnected networks of different pores [114]. Although such a network can be described as a collection of shorter pores, the ionic liquid is nevertheless mainly present deeply in the porous carbons and far from the contact with the bulk electrolyte or pore closings. In this sense, infinitely extended pores can still be considered as good models for these porous materials. The deficiency of infinite pores is that the effects related to the pore closing and opening are completely ignored and the charging dynamics are not straightforward to study.

For the infinite slitpore model, a Monte-Carlo simulation approach is used, (hereafter called *MC model*). The MC data was produced by Dr. Svyatoslav Kondrat in the context of the collaborative project presented in this chapter. The MC model consists

of a single nanopore with an ionic liquid confined between two parallel metal plates, which are infinitely extended in xy-directions modeled by applying periodic boundary conditions in these directions (see Figure 8.1 b).

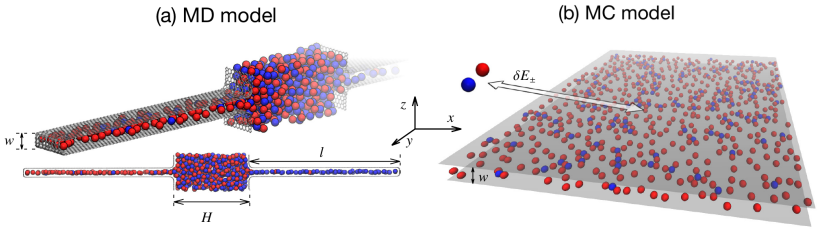


Figure 8.1: Schematics of the finite slitpore model of the MD simulations and the infinite slit used in the MC model. Here, the pore can exchange particles with an implicit reservoir, implied by the arrow between slit and the outside ion pair.

The IL reservoir is taken into account by the transfer energy $\delta E_{pm}$ of an ion from the bulk into the pore, which is assumed to be equal for anions and cations. In this chapter, these two types of models are compared to study the effects of finite and infinite pore lengths on the ion structure and charging.

## 8.1 The MC framework

The interaction potentials were implemented in the *towhee simulation package* [115]. Grand canonical Monte-Carlo simulations were performed using Widom insertion-deletion moves [116], translational moves, and molecular-type swap moves [61]. After $5 \times 10^6$ equilibration steps, up to $10^7$ production steps at temperature $T = 400$K were performed. In both models and all results presented in this chapter, the same pore width $w = 9.37$ Å is used, corresponding to a accessible pore width of $6$ Å. Also, the primitive ion model of charged WCA particles described in Section 7.1.2 was used throughout the comparison.

## 8.2 Matching MC/MD

### 8.2.1 Ion-ion electrostatics

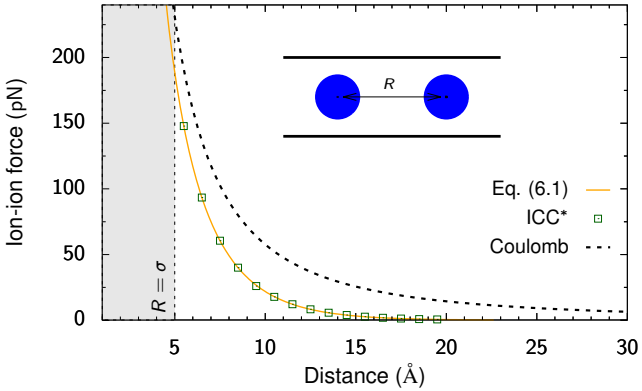


Figure 8.2: Electrostatic force between a pair of like-charged ions for the analytical solution (solid line), the induced charge approach (points) and the vacuum case (dashed line).

The electrostatic potential $U$ at the plates of the MC model by symmetry corresponds to the applied potential $2U$ between the two electrodes of the MD model. $U$ enters the Monte-Carlo scheme by setting the electrochemical potential to $\mu_\pm = \pm eU + \delta E_\pm$. The electrostatic interaction energy between two ions confined in a metal slit pore similar to Eq. 4.17 reads [61]

$$v_{\alpha\beta}(z_1, z_2, R) = \frac{4q_\alpha q_\beta}{\varepsilon w} \times \sum_{n=1}^{\infty} K_0\left(\frac{\pi n R}{w}\right) \sin\left(\frac{\pi n}{w}(z_1 + 0.5)\right) \sin\left(\frac{\pi n}{w}(z_2 + 0.5)\right) \tag{8.1}$$

where $q_\alpha$ and $q_\beta$ are the ion charges ($\pm e$), $R$ is the lateral distance between the ions, $z_1, z_2 \in [-w/2, w/2]$ are their positions across the pore, and $\varepsilon$ is the dielectric constant (taken $\varepsilon = 4$ in this chapter). To test how the superionic state emerges within the ICC* approach, the force between two ions in the pore middle has been calculated and compared with the force obtained from Eq. (8.1) as $f_{\alpha\beta} = -dv_{\alpha\beta}/dR$ (note that $f_{++} = f_{--} = -f_{+-} \equiv f$). Figure 8.2 demonstrates the excellent agreement between the MC and MD methods. Compared to the Coulomb force (dash line) of free ions, the confined interaction is much weaker.

### 8.2.2 Image charge attraction

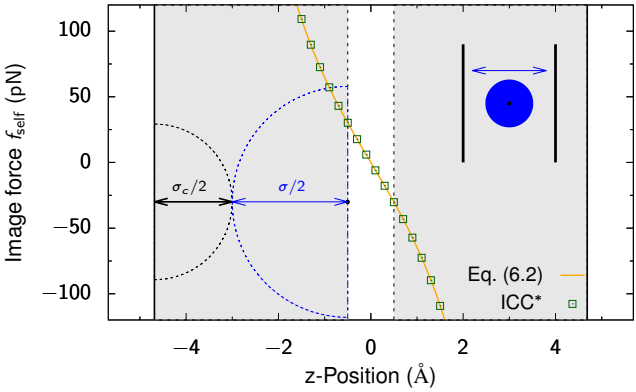


Figure 8.3: Good agreement is found for the attractive image charge force of a single ion approaching the metallic pore boundary comparing the analytical solution (solid line) and the ICC* case (points).

An ion confined in a narrow conducting nanopore experiences an image-force attraction to the pore walls. For a slit metallic pore, infinitely extended in the lateral direc-

tions, this interaction energy can be calculated analytically via [61]

$$E_{\text{self}}^{(\alpha)}(z) = -\frac{q_\alpha^2}{\varepsilon w}\int_0^\infty \left[\frac{1}{2} - \frac{\sinh\big(k(1/2 - z/w)\big)\sinh\big(k(1/2 + z/w)\big)}{\sinh(k)}\right] dk, \tag{8.2}$$

where $z$ is the position across the pore. The interaction potentials in Eq. 8.1 and Eq. 8.2 constitute the superionic state. The image forces acting between an ion and the pore walls obtained by the ICC* approach and from Eq. (8.2) as $f_{\text{self}} = -E_{\text{self}}/dz$ are compared in Figure 8.3 with excellent agreement. Note that the corresponding potential acquires an additional contribution due to periodicity, which can be corrected by considering larger systems. However, this shift in $E_{\text{self}}$ does not influence the ion-pore walls forces, therefore the results of the MD simulations remain the same.

### 8.2.3 Wall potentials

In the MD model, the electrodes have been constructed as described in Section 7.1.1 with fixed pore width of $9.37\,\text{Å}$ and a pore length of $8\,\text{nm}$. The MC model neglects the pore wall structure and consider flat soft walls instead, using the 10-4 Lennard-Jones (LJ) interaction potential

$$\phi_{\text{wall-ion}}^{\text{MC}}(z) = 2\pi\epsilon_{\text{wall-ion}}\sigma_{\text{wall-ion}}^2\rho_{\text{wall}}\left[\frac{2}{5}\left(\frac{\sigma_{\text{wall-ion}}}{z - z_0}\right)^{10} - \left(\frac{\sigma_{\text{wall-ion}}}{z - z_0}\right)^{4}\right] \tag{8.3}$$

where $\epsilon_{\text{wall-ion}}$ and $\sigma_{\text{wall-ion}}$ are the wall-ion energy and diameter parameters, $\rho_{\text{wall}}$ is the two-dimensional number density of carbon atoms, and $z_0$ is the location of the wall. This potential is obtained by integrating the LJ inter-particle interaction potential over a surface of LJ particles, where the surface is infinitely extended in the xy-directions. In order to match the MC and MD models, the interaction potential (Eq. 8.3) is fitted to the averaged potential that an ion experiences when approaching the atomistic wall.

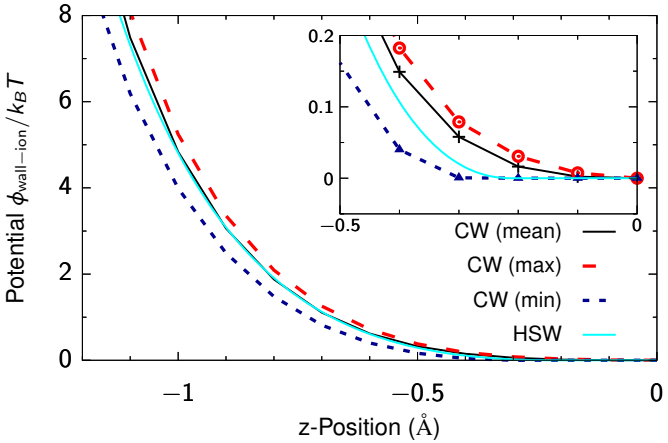


Figure 8.4: Matching the ion-wall interaction potential of explicit carbon atoms with 10-4 LJ wall potential for MD. The inset shows a zoom to the onset of the interaction in the pore center.

Potential curves of this fitting procedure are shown in figure 8.4, the inset highlights the region close to the pore center ($z = 0$). It is difficult to accurately match the interaction of the carbon walls (CW) used in the MD model in the whole range of the wall-ion distances. Also the atomistic wall-ion potential is not homogeneous in the lateral directions, shown by CW (max) and CW (min) curves. For an optimal match of the homogeneous soft wall potential (HSW), the fitting procedure targets the mean potential. The resulting fitted parameters of the interaction potential given in Eq. 8.3 are $\sigma_{\mathrm{wall-ion}} = 4.472\,\text{Å}$ and $\rho_{\mathrm{wall}} = 0.106\,\text{Å}^{-2}$. In addition to the soft pore walls which interact with the ions via Eq. 8.3, a model of hard walls common for MC simulations was tested. [61, 107–109, 54, 117].

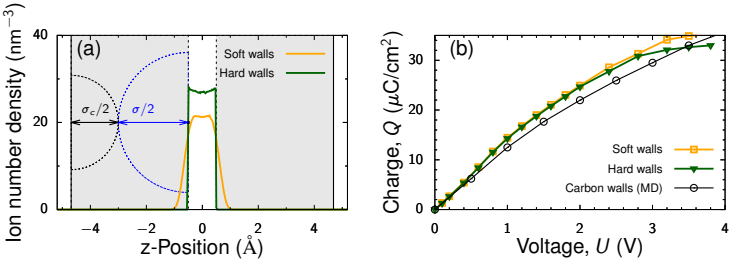


Figure 8.5: Ion density profile (left) and pore charge (right) comparisons between carbon electrodes (MD) and hard/soft wall interaction potentials (MC).

Figure 8.5 (a) shows that the hard walls strongly influence the ionic liquid structure inside a pore, but their effect on the charge storage in Fig. 8.5 (b) is moderate. For low voltages, the accumulated charge in both systems practically coincides and the only significant differences arise at high applied potentials, where the pore with hard walls saturates while the soft-wall pore can accommodate more charge. Although fine details of the non-electrostatic wall-ion interactions are important for the ion structure, their impact on charging is minor, at least at low and intermediates voltages.

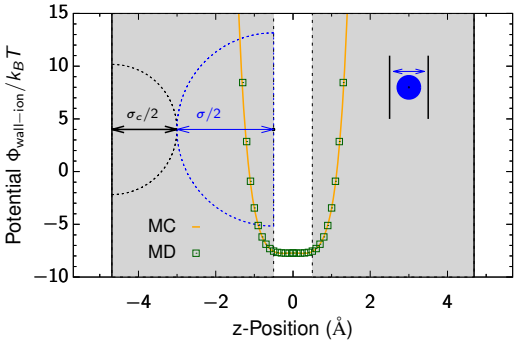


Figure 8.6: MCMD comparison of the total (image charge attraction + wall repulsion) wall-ion potential.

The final test for the total wall-ion interaction potential $\Phi_{\mathrm{wall-ion}}$ as a function of the position $z$ across the pore is shown in figure 8.6 shows. $\Phi_{\mathrm{wall-ion}}$ consists of the image-force potential (Fig. 8.3) and the 10-4 LJ interaction (Fig. 8.4) and compares average ion-wall potential used in the MD model (open squares) to the total potential used in the MC model (solid line). The shift in self-energy due to the 3D periodicity enforced by the ICC* algorithm vanished, as the 2D periodic electrostatic solver ICMMM2D [118] was used to calculate the image-force contribution to $\Phi_{\mathrm{wall-ion}}$.

### 8.2.4 Matching the pore density

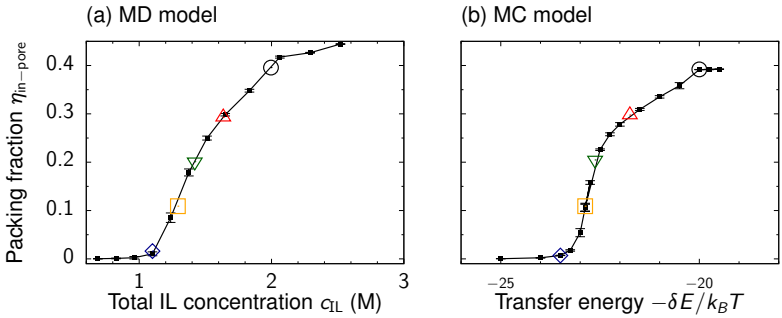


Figure 8.7: Matching transfer energy (MC) and IL concentration (MD) to result in similar pore density at 0V.

The in-pore packing fraction at zero potential $U = 0$ should match for both models to further compare the systems in the charged state. We calculated this packing fraction as $\eta_{\mathrm{in-pore}} = \pi\sigma^3/(6V_{pore})$, where $\sigma = \sigma_{\pm} = 5$ Å is the ion diameter and $V_{pore} = Sw_{\mathrm{acc}}$ is the volume of a pore. $S$ is the lateral area and $w_{\mathrm{acc}}$ the accessible pore width. In the MD model, unless otherwise specified, only the middle parts of the pores were taken into account when calculating $\eta_{\mathrm{in-pore}}$ and the entrance and the closing of the pores were excluded. Since $w_{\mathrm{acc}}$ is not known exactly *a priori* and is expected to vary with

the applied potential, $w_{\mathrm{acc}} = w - \sigma_c$ is used where $\sigma_c = 3.37\,\text{Å}$ is the diameter of the carbon atom. The pore width $w = 9.37\,\text{Å}$ gives $w_{\mathrm{acc}} = 6\,\text{Å}$. Note that this is the accessible pore width for a system with hard pore walls. In the MD model, the in-pore ion packing fraction can be controlled by changing the total concentration of ions in the supercapacitor, $c_{\mathrm{IL}}$. Physically this can be realized by varying the pressure in the case of pure ionic liquids or by varying the salt concentration in the case of electrolyte solutions.

Figure 8.7 (a) demonstrates that the pore becomes less populated as $c_{\mathrm{IL}}$ decreases. However, at extremely low concentrations the MD simulations predict the formation of an IL cluster between the electrodes, which prevents ions from entering the pore at $U = 0\,\mathrm{V}$. In the MC model, the pore occupation is controlled by the ion transfer energy $\delta E$. Figure 8.7 (b) shows that the in-pore packing fraction decreases as $\delta E$ increases, and the pore becomes more ionophobic [119, 120]. The pore saturates for both systems around $\eta_{\mathrm{in-pore}} \approx 0.4$. The less strict saturation in the MD model is attributed to the atomic structure of the electrode wall, allowing increased maximal packing at high densities. After having matched the pore occupancies at no applied potential, voltage-dependent MC and MD simulations were conducted for the systems shown by large symbols in Figure 8.7, where initial concentration and transfer energy leads to the same in-pore packing fraction.

## 8.3 Ion structure

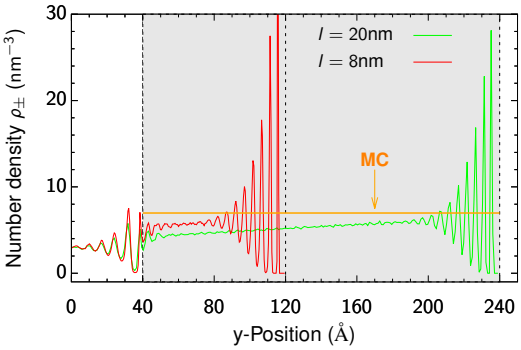


Figure 8.8: In-pore ion structure: The MD model shows a heavily layered pore structure, whereas the MC model produces homogeneous pore densities.

There are two important features in the MD model that are not present in the MC system, the finite pore length $l$ and explicit simulation of the IL reservoir between the electrodes. In order to better understand the impact of the different modeling aspects, the IL structure along the pore is compared. Figure 8.8 shows the ion density profiles for the MD models for two pore lengths $8\,\mathrm{nm}$ and $20\,\mathrm{nm}$. The orange line denotes the density of the MC system. As already shown in Section 7.3.2, the average ion density in the bulk electrolyte depends on the applied voltage. This implies that the chemical potential of the bulk ionic liquid changes with voltage, while it is taken constant in the MC model. In Figure 8.8, the ions exhibit a clear layering near the pore closings and openings, while they seem to form a nearly homogeneous structure in the middle of a pore. However, for non-zero potentials the density is not constant along the pore and increases from the pore entrance to the pore end. Clearly, in the MC model the average ion densities are position independent and a quantitative comparison between the MC and MD model is ambiguous.

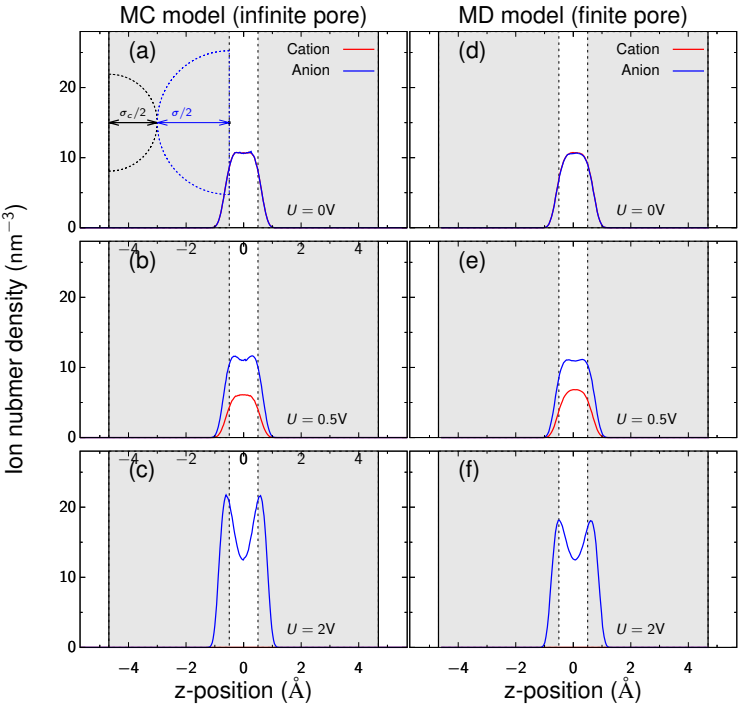


Figure 8.9: Lateral in-pore structure comparison

Figure 8.10: Ion packing in narrow pores from MC simulations with $\delta E_{\pm} = 21.75\ k_B T$ (a-c) and MD simulations with $c_{IL} = 1.6\,\mathrm{mol}$ (d-f).

The ion structure for different voltages across the pore is shown in Figure 8.10. At zero voltage, anions and cations are distributed equally in the pore and collapse on a single density profile. At high applied potentials, the co-ions have left the pore and the counterions prefer to locate themselves at the pore walls due to the image charge attraction towards the metallic boundary. The arising mismatch between the MC and MD model at $2\,\mathrm{V}$ again is attributed to the increasing influence of the atomic electrode structure in the MD simulations, inducing additional ordering in the counterion layers.

## 8.4 Voltage dependence of the pore charge

Figure 8.11 compares the accumulate charge $Q(U)$ from MC and MD simulations for pores with matched occupancies at zero voltage. The data demonstrates that the charging proceeds similarly in the MC and MD models. Interestingly, $Q(U)$ is practically independent of the transfer energies $\delta E$ (MC simulations) and ionic liquid concentrations $c_{\mathrm{IL}}$ (MD simulations). Again, this is because the electrostatic contribution ($\pm eU$) to the total electrochemical potential dominates the contribution due to $\delta E$ and $c_{\mathrm{IL}}$, respectively.

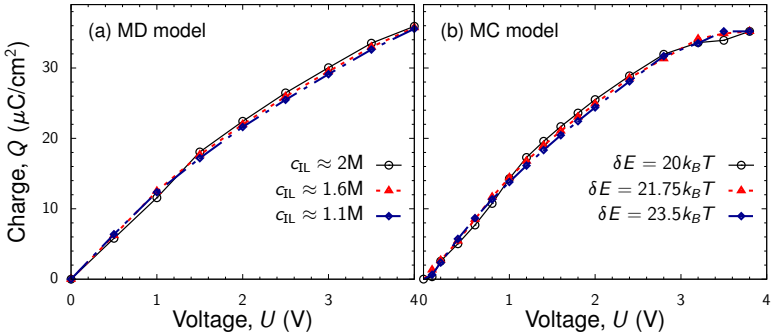


Figure 8.11: Charging from MC and MD simulations. (a) Accumulated charge $Q$ as a function of applied potential $U$ from MD simulations for a few values of the total ionic liquid concentration $c_{\mathrm{IL}}$ in a supercapacitor. (b) $Q$ from MC simulations for a few values of the transfer energy $\delta E$.

The direct comparison of the charge curves in Figure 8.12 highlights the quantitative differences of the two simulation approaches. For applied potentials $U > 1\,\mathrm{V}$, the difference becomes more apparent until the data aligns again when the pores start to saturate at high voltages $U \approx 4\,\mathrm{V}$. This comparison shows that the finiteness of the pore in the MD model has its greatest impact in that intermediate voltage regime.

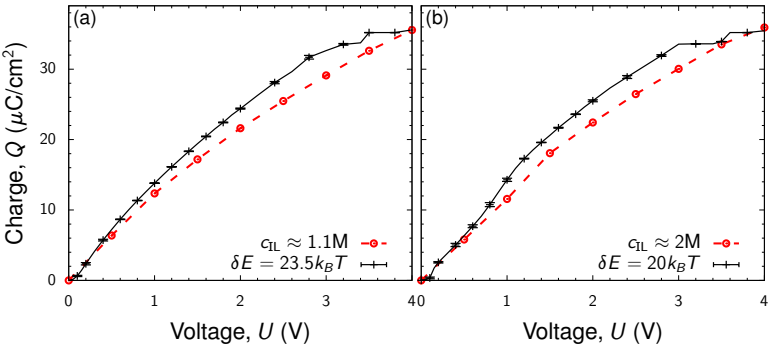


Figure 8.12: Direct comparison of the pore charge in the MC and MD model for two different concentrations / transfer energies.

## 8.5 Charging mechanism

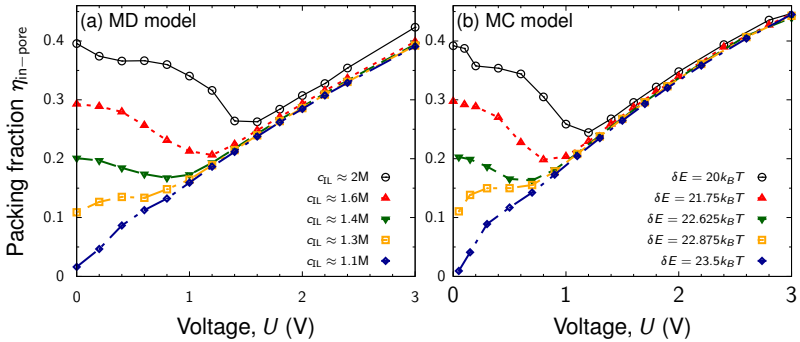


Figure 8.13: Total packing fraction $\eta_{\mathrm{in-pore}}$ of ions in a pore and charging parameter $X_D$ from (a) MD and (b) MC simulations. MC and MD models predict similar behaviors of $\eta_{\mathrm{in-pore}}$ at low and intermediate voltages. Small discrepancies appear only at higher potentials likely due to the differences in the pore wall structures in the MD and MC models.

Figure 8.13 depicts the ion packing fraction in the pore $\eta_{\mathrm{in-pore}}$ as a function of the applied potential. In all cases of strongly ionophilic pores, i.e. pores with a substantial amount of an ionic liquid at no voltage, $\eta_{\mathrm{in-pore}}$ first decreases for increasing voltage, and starts to increase only when there are no co-ions left in the pore. In other words, at low voltages charging is dominated by co-ion desorption, while it is counterion adsorption that drives charging at higher applied potentials [61, 6, 7, 119]. This is consistent with previous observations [119], showing that desorption (and swapping) are thermodynamically preferable over adsorption in most cases, except of a narrow window of parameters in which desorption and swapping are unfeasible due to the lack of co-ions.

To characterize charging mechanisms in more detail, the charging parameter $X_D(U)$ is calculated from the voltage dependent pore occupation of both ion species via

$$X_D(U) = \frac{e}{C(U)} \frac{dN}{dU}, \tag{8.4}$$

where $e$ is the elementary charge, $C(U) = dQ/dU$ the differential capacitance, $Q$ denotes the accumulated charge and $N$ the total number of ions. $X_D$ expresses how charging is related to pore filling or de-filling and describes which charging mechanism takes place. If charging is driven solely by swapping of co-ions for counter-ions, then the total ion density does not change, $N = \mathrm{const}$, and hence $X_D = 0$. For pure adsorption we have $edN/dU = dQ/dU$ and thus $X_D = 1$, while for desorption $dQ/dU = -edN/dU$ and so $X_D = -1$. The parameter $X$ of [12] is related to $X_D$ in a similar fashion as the integral capacitance is related to the differential capacitance:

$$X(U) = \frac{1}{Q} \int_0^U X_D(u) C(u) du, \tag{8.5}$$

which can be seen as a voltage-averaged $X_D$ with the weight $C(u)$, where $Q = \int_0^U C(u)du$ is a normalization constant.

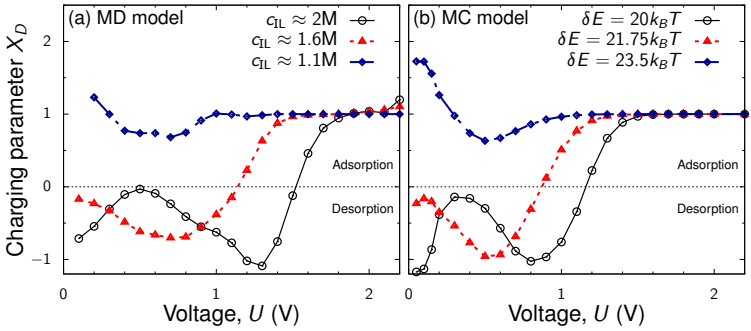


Figure 8.14: Charging parameter $X_D$ from MD (a) and MC (b) simulations showing the regions where charging is dominated by adsorption ($X_D > 0$) and desorption ($X_D < 0$). $X_D = 0$ corresponds to swapping of co-ions for counterions.

The charging parameter $X_D$ obtained from MD and MC simulations is presented in Figure 8.14. It shows that at high voltages charging is solely due to counter-ion adsorption ($X_D \approx 1$), but at low voltages it can be either co-ion desorption or counter-ion adsorption, depending on the initial conditions given by $c_{\mathrm{IL}}$ or $\delta E$. Interestingly, for highly ionophobic pores when the pore is nearly empty at no applied potential, the parameter $X_D$ is significantly greater unity, which means that *both* counter and co-ions are adsorbed into the pore at low voltages. This is likely because at low densities the entropic cost of ion insertion is low and the low voltage allows the ions to enter the pore in pairs.

## 8.6 Differential capacitance

Fine details of the charging process are captured by the differential capacitance $C = dQ/dU$ shown in Figure 8.15. Although $Q(U)$ does not seem to vary significantly with $c_{\mathrm{IL}}$ or $\delta E$ (see Fig. 8.11), $C(U)$ shows nevertheless a complex behavior, particularly for densely populated ionophilic pores (low $\delta E$ or high $c_{\mathrm{IL}}$ respectively). For such pores,

the capacitance exhibits a first maximum corresponding to co-ion/counterion swapping and a second maximum associated with the co-ion desorption, before it finally decreases as the pore becomes more and more occupied by counterions and charges by adsorption at high voltages. For weakly ionophobic pores there is only one maximum in $C(U)$ at low pore occupancies, while at high potentials the charging proceeds similarly for all pores.

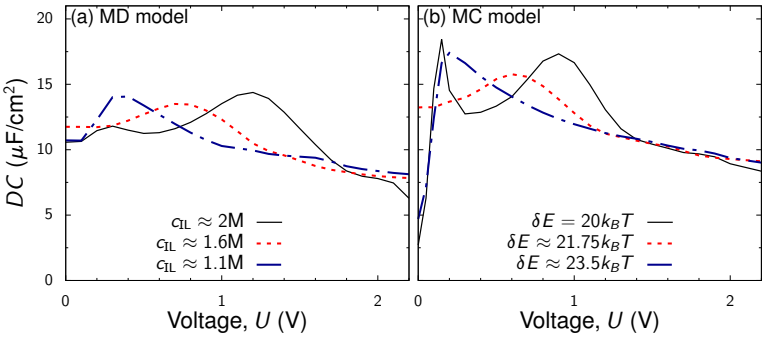


Figure 8.15: Differential capacitance as a function of voltage from (a) MD and (b) MC simulations.

## 8.7 Conclusions

The main conclusion is that although the MC and MD models are *qualitatively* consistent with each other (Figures 8.14, 8.15 and 8.10), there are some important differences due to the finite pore length. In particular, the pore entrances and closings seem to have a vivid effect on the ion structure inside a pore. At high concentrations and/or high applied potentials, the ion density is not constant along the pore but varies roughly linearly between the pore entrance and the pore end, where it exhibit a strongly oscillatory structure (Fig. 8.8). This impedes a complete *quantitative* match of the two models. Further findings are summarized below:

- Interestingly, the accumulated charge seems to be only weekly dependent on the total ion density in a supercapacitor (Fig. 8.15). This observation provides an additional degree of freedom for optimizing the charging dynamics by varying the ion concentration without significantly compromising the energy density (note that the fine details of the charging process are resolved by the differential capacitance, which does depend on the total ion concentration/ion transfer energy (Fig. 8.15 (c)).

- Even though hard and soft pore walls lead to significant differences in the in-pore ion structure, they show practically the same charging behavior (Fig. 8.5). This is likely because the applied potential 'overrules' all fine details of the non-electrostatic wall-ion interactions and the resulting particle structure.

- At high voltages, charging proceeds exclusively via counter-ion adsorption, while at low voltages the charging process is dominated by either co-ion desorption or counter-ion adsorption, depending on the ion transfer energy or the total ion concentration (Fig. 8.14). Remarkably, at low ion concentrations and low voltages, both counter- and co-ions are adsorbed into the pore (Fig. 8.14 (c)).

# 9 Slitpore dynamics

Parts of the content in this chapter has been published in the following article: article. My contributions: Performed simulations, data analysis, figures, snapshots and parts of the writing.

> **K. Breitsprecher**, C. Holm and S. Kondrat
> "Charge Me Slowly, I Am in a Hurry: Optimizing Charge–Discharge Cycles in Nanoporous Supercapacitors
> *ACS Nano*, **2018**, 12 (10), pp 9733-9741
> URL: https://doi.org/10.1021/acsnano.8b04785

In the preceding Chapters 7 and 8, mostly static observables of the finite slitpore system have been analyzed. This chapter aims towards understanding the dynamical charge transport in subnanometer pores in greater detail. The focus lies on time scales reachable by coarse grained MD simulations, typically in the order of nanoseconds. Besides measuring the time evolution of the pore occupation, the simulation framework also allows to apply a time dependent voltage $U(t)$ between the electrodes to study the response and potentially improve the performance of the capacitor system by physically motivated voltage protocols for charging and discharging. Furthermore, the origin of the already mentioned non-equilibrium state of trapped co-ions and the effect of voltage protocol parameters are discussed in this chapter. Another central issue is rescaling the results to macroscopic systems. To this end, the pore length scaling of key results is analyzed, allowing to extrapolate the time dependence of length scales reachable with the MD simulation scheme of this work ($\sim$ nm) to macroscopic systems.

## 9.1 Models and Methods

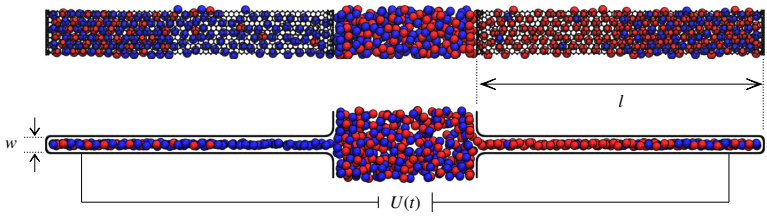


Figure 9.1: Overview sketch of a long slitpore with $l = 20\,\mathrm{nm}$ and indicated applied dynamic potential $U(t)$.

Two ionic liquid models have been used in this chapter. In most cases, the monovalent WCA model described in Section 7.1.2 with a diameter of $\sigma = 5\,\text{Å}$ was chosen, known to capture the essential physics of ionic liquids. [121, 122, 52, 51, 123]. Additionally, the more realistic four-site model of BMIM $PF_6$ [24, 25] was used (see Section 5.1.3). The carbon atoms were modeled with a 9-12 Lennard Jones potential with parameters $\sigma_c = 3.37\,\text{Å}$ and $\epsilon_c = 0.23\,\mathrm{kJ\,mol^{-1}}$. The same closed slit nanopore system described in detail in section 7.1.1 is used with a Langevin thermostat at temperature $T = 400\,\mathrm{K}$ and damping constant $\gamma = 10\,\mathrm{ps^{-1}}$ In all simulations, at least $4\,\mathrm{ns}$ of equilibration with no applied potential was performed before production runs. Again, the electrodes were kept at a constant potential using the ICC* algorithm [67] with a superimposed time-dependent external potential which has been precalculated by solving the Laplace equation [124] for all electrode geometries considered at a reference potential drop of $1\,\mathrm{V}$ and rescaled to the time-dependent potential during the simulations.

## 9.2 Step-voltage charging

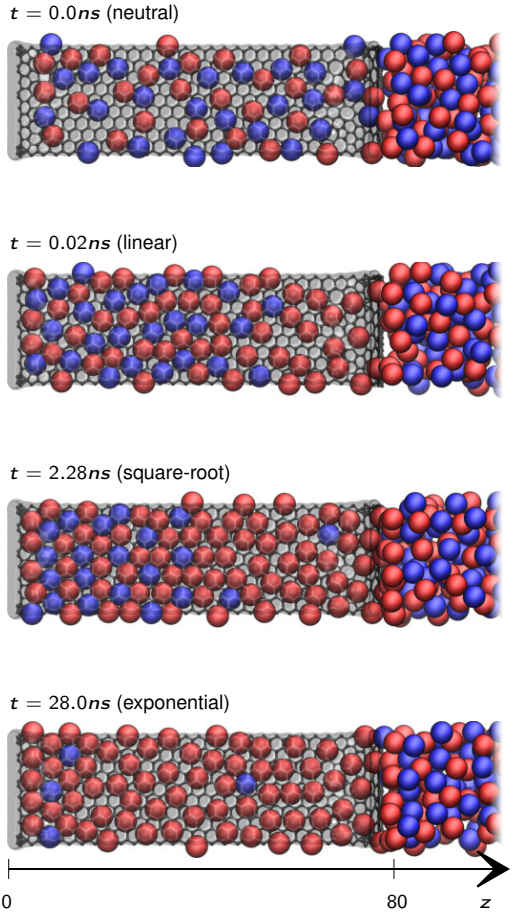


Figure 9.2: Simulation snapshots of step-voltage charging at selected times representative for the charging regimes.

Frequently, the voltage between the electrodes of a supercapacitor is applied in a step-like fashion. It is turned on abruptly and the system is allowed to complete charging and equilibrate. This is a particularly favorable method in MD simulation studies, which, with a few rare exceptions [125, 126, 123], use step-voltage to study charging dynamics [127, 70, 9, 6]. However, as illustrated in Figure 9.2, step-voltage charging can cause some co-ions to become (temporarily) trapped inside narrow pores on the time scales of a typical molecular dynamics simulation [126, 123]. Depending on the magnitude of the applied potential, the steady state configuration of the charged pore can consist of co- and counterions. However, in this parameter set with an applied potential of $3\,\mathrm{V}$, the in-pore co-ion density should vanish in equilibrium, known from long simulation runs and simulations with different voltage protocols that avoid co-ion trapping. The step-voltage simulations show a significant amount of co-ions in the pores even after $28\,\mathrm{ns}$ of simulation time. The scan-rate dependence of the capacitance obtained by cyclic voltammetry in experimental setups [128, 80] suggest that co-ion trapping may occur in experimental systems and commercially fabricated supercapacitors, reducing their power and energy densities, particularly in high frequency applications.

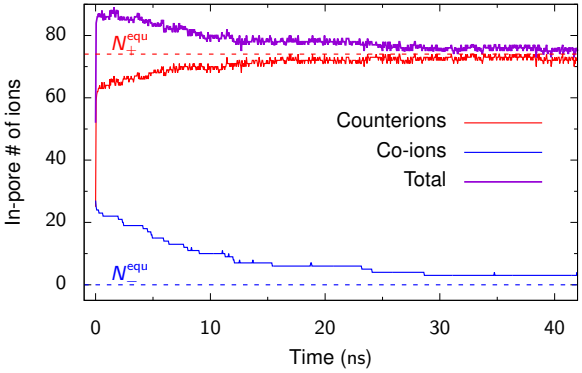


Figure 9.3: Time evolution of ion numbers in the pore. The dashed lines indicate the numbers of co- and counterions in the final charged state.

The co-ion trapping takes place because a sudden application of voltage causes a fast field-driven adsorption of counterions from the bulk electrolyte into the pores. It is important to recall that the electric field caused by the applied potential is very weak deep inside the pore, so field-driven effects are associated with the entrance region of the pore. This counterion adsorption process occurs on time scales of a fraction of a nanosecond (for the pore length considered), and leads to significant pore overfilling[129, 127]. This can be seen in Fig. 9.3, where the sum of all ions (purple data) clearly exceeds the equilibrium particle count given by $N_{tot}^{\mathrm{equ}} = N_{+}^{\mathrm{equ}}$. The adsorbed counterions compress the in-pore ionic liquid, leading to the formation of a crowded neutral phase and a dilute charged phase in the entrance region of the pore (Fig. 9.2 at $0.02\,\mathrm{ns}$). The co-ions become trapped in the crowded phase (Fig. 9.2 at $2.28\,\mathrm{ns}$), where they exhibit slow hopping-type motion before they can eventually diffuse out of the pore through the dilute, counterion rich phase (Fig. 9.2 at $28.0\,\mathrm{ns}$). As a consequence, the co-ion desorption occurs dramatically slowly and on much longer time scales.

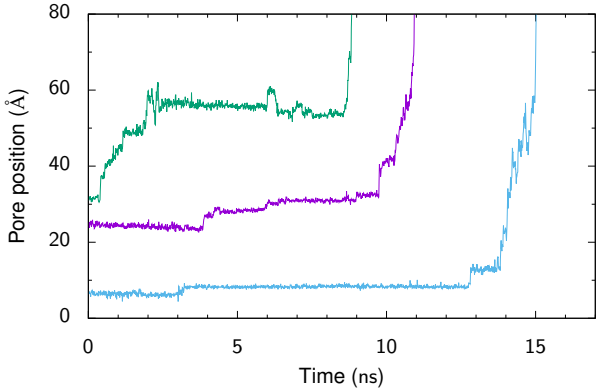


Figure 9.4: Three selected ion escape trajectories. The trapped particles deep in the pore rest in place much longer compared to the actual desorption time.

Three selected examples of ‘escape paths’ of trapped co-ions are shown in Figure

9.4. While trapped in the crowded phase, the co-ions only advance towards the pore entrance by abrupt hopping motion until they reach the front of the dilute phase where they diffuse out of the pore in a few nanoseconds. In order to analyze charging modes quantitatively, 20 independent simulations have been performed to obtain accurate averaged charging curves.

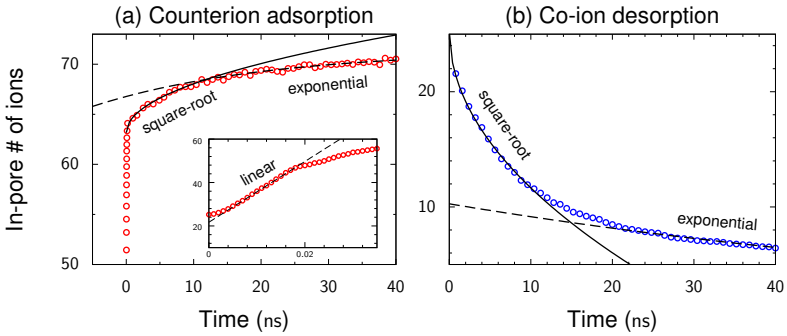


Figure 9.5: Charging regimes of the step-voltage charging process of counterions(a) and co-ions (b). The simulation data was averaged over several runs.

These charging curves, shown in Figure 9.5 separately for counterions (a) and co-ions (b), reveal four distinct charging regimes:

### Linear charging regime

Initially, at very short times, the counterion adsorption proceeds linearly in time, shown in the inset in Fig. 9.5 (a). This is due to the forces resulting from the applied potential and is similar to the charging of flat electrodes. The electric field of the applied potential depicted in Fig. 7.3 (b) rapidly decays in the first few nanometers of the pore, so only the field in the entrance region of the pore is actually driving the charging process.

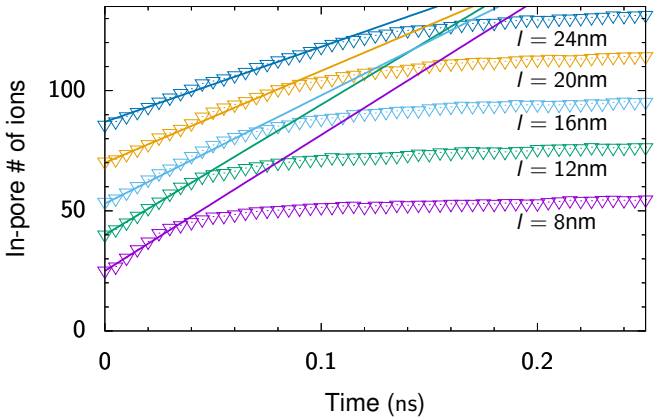


Figure 9.6: Zoom to the onset of the charging process for several pore lengths. The dashed lines are fitted to the linear charging regime.

The linear regime for several pore lengths is shown in Figure 9.6, the characteristic time scale depends on the pore length and hence must be determined by the compression rate of the in-pore ionic liquid. The linear counterion adsorption leads to a linear growth $Q \sim t$ of the accumulated charge at short times. This is consistent with the transmission-line model of charging CDC electrodes [70], but has not been seen in simulations of open slit pores [127].

### Square-root diffusive regime

After the initial linear regime, the charging becomes driven by collective inter-diffusion of co- and counter ions. Figure 9.5 shows that both co-ion desorption and counterion adsorption proceed diffusively, which implies that the accumulated charge grows as a square root of time, i.e. $Q \sim t^{1/2}$ at intermediate times, which has been shown previously [129, 127]. A similarity can be pointed out between this regime and the charging of wide pores, where the square-root behavior follows from the equivalent

circuit considerations [130, 2]. Note that the physical origin of this behavior is different for wide and narrow pores. While it is the resistivity of a *bulk* ionic liquid and the capacitance of the pore wall–ionic liquid interface that determine charging in wide pores, it is determined by the collective *in-pore* diffusivity of ions and by the screened ion-ion interactions in the superionic state for narrow pores [129, 127].

#### Two exponential regimes

Both counterion adsorption and co-ion desorption proceed exponentially at the later stage of charging, the charge behaves as $Q/Q_{equ} \sim 1 - e^{-t/\tau_1}$, where $Q_{equ}$ is the accumulated charge in equilibrium and $\tau_1$ the decay length. The characteristic times of the exponential regime for co- and counterions are different. In particular, the counterion adsorption is faster with the decay time $\tau_{ads} \approx 26\,\mathrm{ns}$, while the co-ion desorption time is $\tau_{des} \approx 87\,\mathrm{ns}$ (for the parameters of Fig. 9.5). This leads to two exponential charging regimes characterized by a mixture of adsorption and desorption. The slower desorption-dominated regime has been previously termed a super-slow regime [127].

## 9.3 Ramp-voltage charging

The remedy against co-ion trapping and the accompanying slow charging is to *slow down* the charging process itself by using a zero based linear voltage protocol $U(t) = k \cdot t$ with a certain slope $k$. In other words, instead of suddenly switching the voltage on, a linear *sweep* from zero volts to the desired potential is used. If the sweeping rate is chosen wisely, the system charges considerably faster as compared to the step-voltage charging.

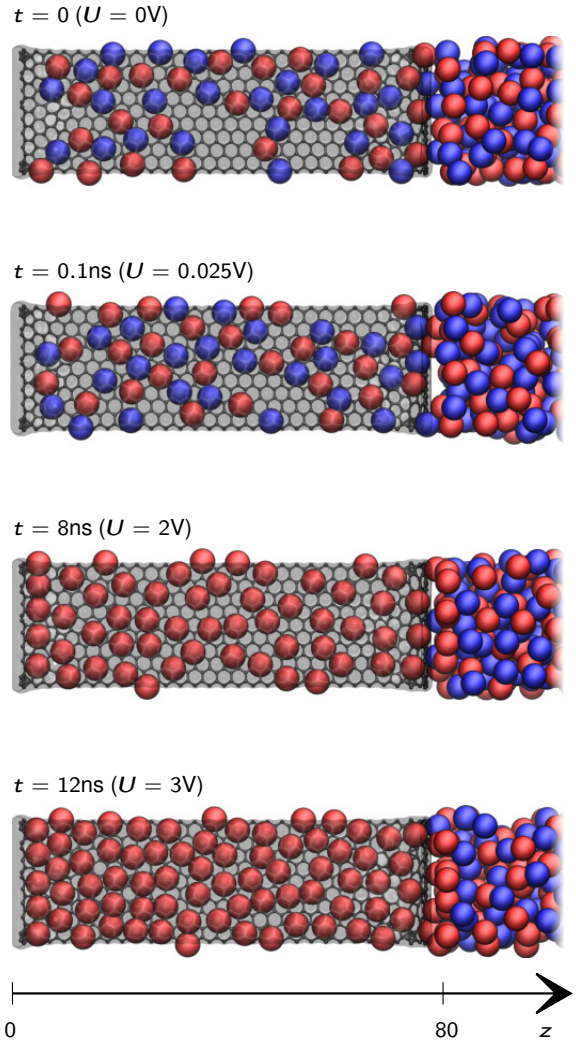


Figure 9.7: Simulation snapshots of ramp-voltage charging at selected times and voltages.

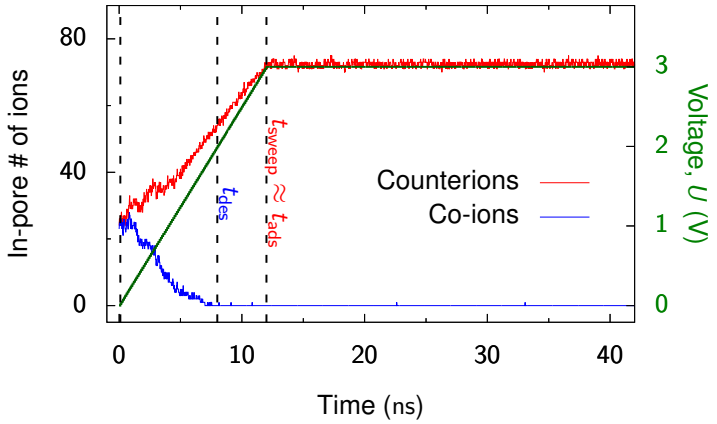


Figure 9.8: In-pore particle count for linear voltage sweep. The vertical dashed lines denote the times of the snapshots shown in Fig. 9.7.

For instance, for the sweep rate $k = 0.25\,\mathrm{V}$ (Figures 9.7 and 9.8), the system is fully charged after just $12\,\mathrm{ns}$ ($t_{\mathrm{ads}}$) and the pores are free of co-ions in less than $8\,\mathrm{ns}$ ($t_{\mathrm{des}}$). In the step-voltage charging of the same system, the co-ions were present in the pores even after $40\,\mathrm{ns}$ of the simulation time (Fig. 9.3). The reason why charging is faster with the linear voltage protocol is that the system can follow a quasi-equilibrium path, which helps to avoid pore overfilling and co-ion trapping. Figure 9.7 illustrated the evolution of the charging process: The initial crowded and counterion rich phases have vanished and the pore gradually proceeds towards the final configuration of a pure counterion population. Since at low voltages the charging is predominantly due to co-ion desorption [131, 123], a slowly increasing voltage gives the system enough time and reduces the pore occupancy, which enhances the ion diffusivity [127, 132] and hence speeds up the charging dynamics.

### 9.3.1 Optimal sweep rate

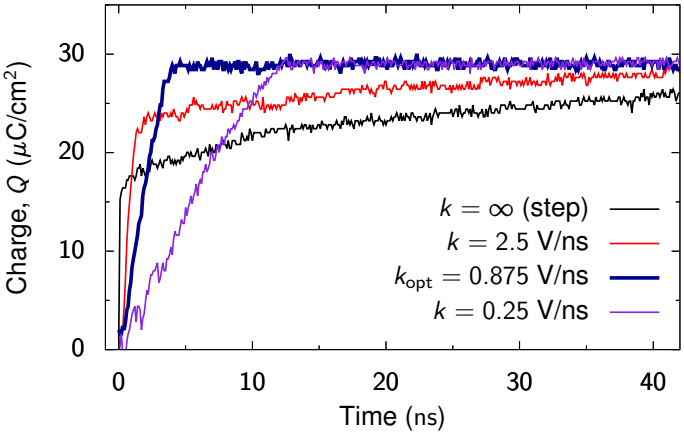


Figure 9.9: Dynamic charging curves for various sweep rates. For $k = 0.875\,\mathrm{V\,ns^{-1}}$, the charging time is minimal (bold blue line).

The quasi-equilibrium charging may also allow to benefit more from the electrode's charge-storage capabilities when there are limitations on charging times. Referring to Figure 9.8 as an example, if the voltage is linearly increased with slope $k = 0.25\,\mathrm{V\,ns^{-1}}$, the charging is complete by $t = 12\,\mathrm{ns}$, while the supercapacitor is about $30\%$ undercharged if the step-voltage charging is stopped at the same time. For shorter times this advantage decreases or may even vanish, but the sweep rate can be optimized to obtain the highest charging. This can be seen from the $Q(t)$ curves for various values of $k$ in Figure 9.9 showing that the charging time $t_{\mathrm{charge}}$ is sensitive to $k$. For fast sweeping (large values of $k$), the system may still experience co-ion trapping and overfilling, leading to a large $t_{\mathrm{charge}}$. For example, sweeping the voltage with the high rate $k = 2.5\,\mathrm{V\,ns^{-1}}$ leads to only a slightly faster charging than by step-voltage, but it is

much slower than when the voltage is swept with a lower rate $k = 0.25\,\mathrm{V\,ns^{-1}}$. At sufficiently low rates the system has enough time to respond to the changes in the applied potential, so that the charging follows closely the equilibrium path. Therefore, for small $k$, the charging time is $t_{\mathrm{charge}} = U/k$, which increases with decreasing $k$. Thus, for high $k$ the charging is slow due to co-ion trapping, while at low $k$ one loses time because the system could react faster than the imposed voltage sweep. This means that in between these two regimes there is an optimal sweep rate that minimizes the charging time. If $k$ is in the range of equilibrium charging where no trapping occurs (as in Fig. 9.8 with $k = 0.25\,\mathrm{V\,ns^{-1}}$), the co-ion desorption finishes earlier than the counterion adsorption. Since the adsorption time in that regime is $t_{\mathrm{ads}} = U/k$, it can be decreased by sweeping the voltage faster. The optimal rate $k_{\mathrm{opt}}$ is obtained when the adsorption time becomes equal to the desorption time $t_{\mathrm{des}}$.

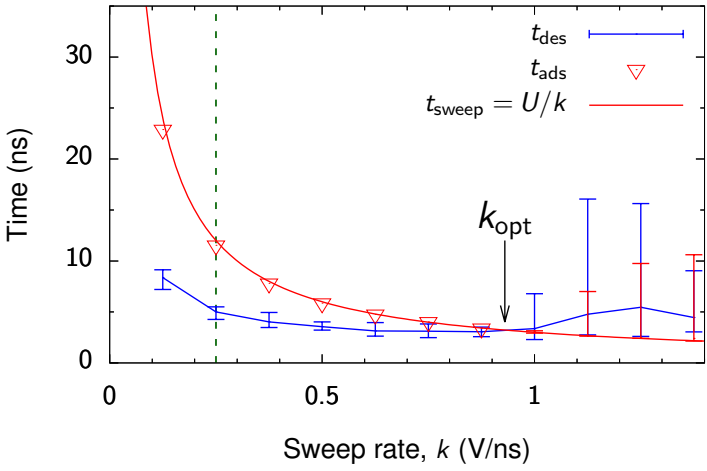


Figure 9.10: Adsorption and desorption times as functions of the sweep rate. The vertical dash line denotes $k = 0.25\,\mathrm{V}$ used in Figures 9.7 and 9.8. Beyond $k_{opt}$, the error in charging time increased due to co-ion trapping.

This is verified in Figure 9.10 which shows the charging times averaged over 5 independent simulations runs per value of $k$ in the range of $0.125\,\mathrm{V\,ns^{-1}}$ to $0.875\,\mathrm{V\,ns^{-1}}$. Indeed, for $k > k_{\mathrm{opt}}$, the desorption time $t_{\mathrm{des}}$ increases with increasing $k$ due to co-ion trapping and overfilling. In the plot, this results in large error bars (denoting the minimal and maximal charging times of the 5 independent simulations) for $k > k_{\mathrm{opt}}$, as trapping can vary in intensity for different runs. For $k$ below $k_{\mathrm{opt}}$, there is no trapping but sweeping as such is too slow. This leads to the simple equation $t_{\mathrm{des}}(k_{\mathrm{opt}}) = U/k_{\mathrm{opt}}$ for determining the optimal sweep rate $k_{\mathrm{opt}}$.

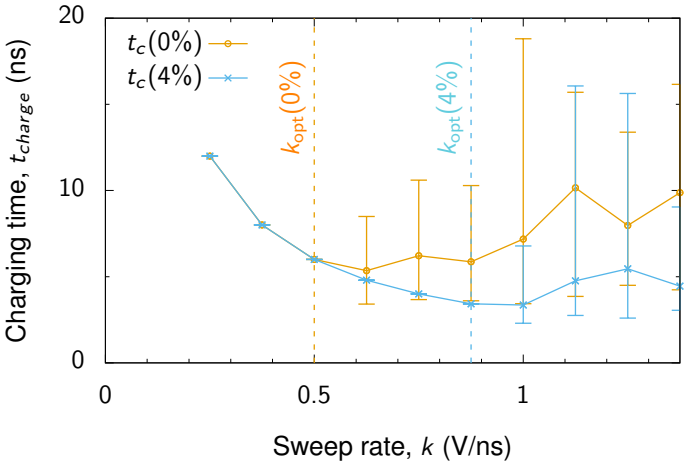


Figure 9.11: Total charging time as a function of sweep rate for $0\%$ and $4\%$ tolerance.

In the 'super-slow' regime of the desorption process with trapping (e.g. Fig. 9.3), the last few co-ions require a large amount of time to leave the pore and don't contribute much to the charge. Therefore, allowing a certain amount of trapping to occur in the system speeds up simulations but leads to a lower value of the 'optimal' sweep rate (and lower charging times) than when demanding a system with no trapping. This motivates to introduce a tolerance that allows a certain percentage of co-ions to remain

in the pore. The desorption is finished at the time the co-ion particle count drops below a certain threshold, expressed here in percentage of the number of co-ions at $t = 0\,\mathrm{ns}$. Figure 9.11 shows two curves for charging time $t_{charge}(k)$ with $0\%$ and $4\%$ tolerance, leading to different values of $k_{\mathrm{opt}}$, shown by vertical dashed lines. Allowing for $4\%$ tolerance in determining $t_{\mathrm{des}}$ for computational efficiency, an optimal sweep rate of $k_{\mathrm{opt}} \approx 0.875\,\mathrm{V\,ns^{-1}}$ and a charging time of about $3.3\,\mathrm{ns}$ is obtained.

### 9.3.2 Pore charge saturation

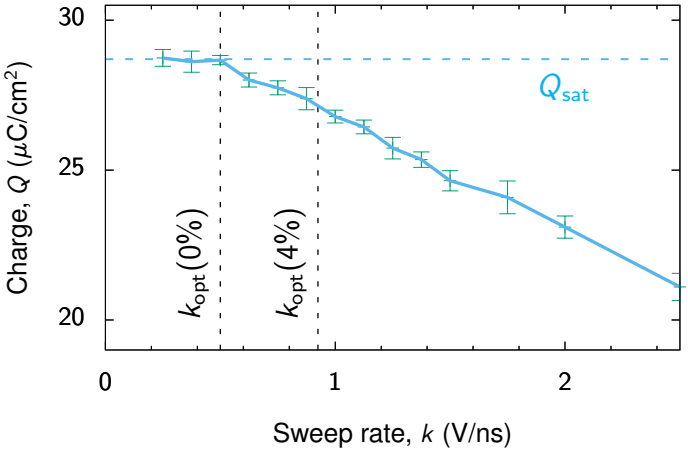


Figure 9.12: The accumulated pore charge as a function of sweep rate. $Q(k)$ levels off top $Q_{sat}$ at $k_{opt}(0\%)$. The dashed lines point to the sweep rates with $0\%$ and $4\%$ loss of the charge.

For a representative electrode and a given working voltage, the accumulated charge $Q$ can be measured as a function of the sweeping rate $k$ (note that $Q$ must be measured at the end of the sweeping process at time $t = U/k$). The so-measured $Q(k)$ obtained by simulations is illustrated in Figure 9.12. It saturates at $Q_{\mathrm{sat}} = 28.5\,\mu\mathrm{C\,cm^{-2}}$, the

optimal rate $k_{\mathrm{opt}}$ corresponds to the highest rate at which $Q \approx Q_{\mathrm{sat}}$ (here measured to $k_{\mathrm{opt}}(0\%) = 0.5\,\mathrm{V\,ns^{-1}}$). The $Q(k)$ dependence could be used to determine $k_{opt}$ in experiments. It also shows that there is a trade-off between charging time and accumulated charge.

### 9.3.3 Pore length dependence of the optimal sweep rate

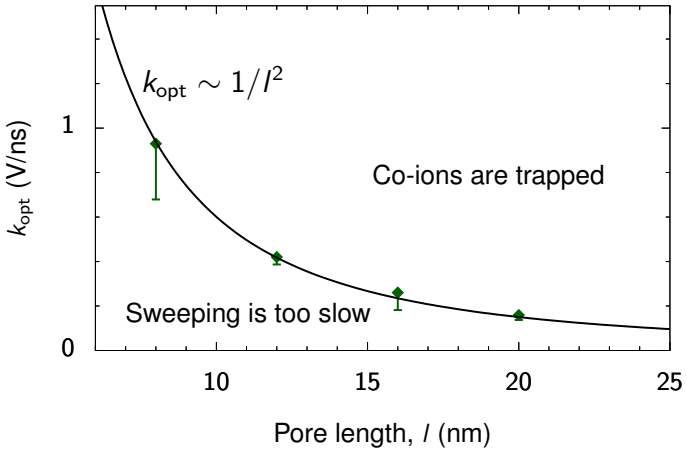


Figure 9.13: Optimal sweep rate $k_{opt}$ with simulation data points of four different pore lengths. The solid line shows the fitting curve $k_{opt}(l) = A/l^2$.

With the analysis routine described in Section 9.3.1, the optimal sweep rates for a pores with different lengths $l$ between $8\,\mathrm{nm}$ to $20\,\mathrm{nm}$ for $4\%$ tolerance have been obtained, the result is shown in Figure 9.13. It is found that the following equation describes the $k_{\mathrm{opt}}(l)$ dependence remarkably well:

$$k_{\mathrm{opt}} = \frac{1}{Al^2}, \tag{9.1}$$

where $A$ is a fitting parameter, which depends on the applied potential. For the data shown in Figure 9.13 at $3\,\mathrm{V}$, $A \approx 1.67 \times 10^{-4}\,\mathrm{ns\,V^{-1}\,\mathring{A}^2}$ was found. This behavior can be understood by assuming free two-dimensional diffusion as the physical origin of the desorption process: By increasing the voltage by $\Delta U$, one has to allow enough time for the co-ions to leave the pore. This time can be roughly estimated as

$$\Delta t_{\mathrm{opt}} \approx (l^2/D_{\mathrm{coion}}),$$

here $D_{\mathrm{coion}}$ is the co-ion diffusion coefficient, which depends on the current state of the system but does not depend on the pore length. This implies

$$l^2/\Delta t_{\mathrm{opt}} = const,$$

which gives the relation (Eq. 9.1) by using

$$\Delta t_{\mathrm{opt}} = \Delta U/k_{\mathrm{opt}}$$

and assuming the same $\Delta U$ for all steps. A particle-based interpretation of this result is that the desorption of co-ions buried deeply in the pores proceeds via diffusion and is the limiting factor of the total charging process. For adsorption, the counterions only have to enter the pore to contribute to the net charge.

## 9.4 Charging with BMIM $PF_6$

In order to determine accurately the optimal sweep rates, a large number of simulations for various rates and pore lengths including several independent runs to assure equilibrated charged states have to be performed. With the computationally inexpensive model of an ionic liquid consisting of charged soft spheres used so far in this chapter, these large parameter sets can be accessed in reasonable time. To test if the trapping effect persist for real ionic liquids, additional simulations are carried out with

the coarse-grained model of BMIM $PF_6$, which has proven to provide quantitatively reliable results when compared to experiments [24, 27, 133, 134, 28]. Figure 9.14 demonstrates that also for BMIM $PF_6$ the co-ions become trapped in the pores when the voltage is switched on between the electrodes in a step-like manner. As discussed, the reason is that the counterions are quickly adsorbed into the pore during the initial (linear) stage of charging, blocking the anions from diffusing out of the pore. Applying a slow voltage sweep slows down the cation adsorption and allows a faster anion desorption. Note that in this plot the sweep rate is not optimized. Interestingly, co-ion trapping appears weaker in the anode (see Fig. 9.15), which is likely because the smaller anions block the cations less efficiently. Similarly, as for the charged soft spheres, we observe a transient formation of two phases of BMIM $PF_6$ in the pores, with the co-ions exhibiting a hopping type of motion in the neutral crowded phase, and a diffusive behavior in the more dilute counterion rich phase.

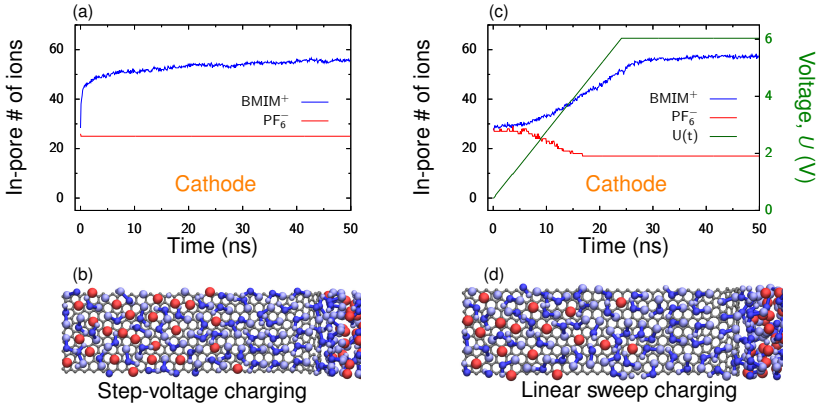


Figure 9.14: Comparison of step- and sweep voltage charging in the cathode with the coarse grained ion model BMIM $PF_6$ showing exemplary simulation snapshots and charging curves. For step-like charging, the $PF_6$ co-ions are trapped in the pore, whereas some co-ions can desorb when using a voltage ramp.

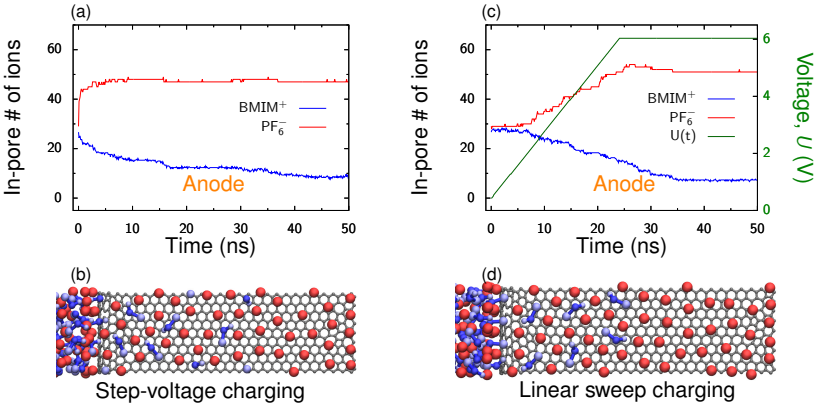


Figure 9.15: Comparison of step- and sweep voltage charging in the anode with the coarse grained ion model BMIM $PF_6$ showing exemplary simulation snapshots and charging curves. Due to the asymmetric ion model, trapping is weaker in the anode.

## 9.5 Discharging

With a few notable exceptions [135, 136], prior works have mainly focused on the process of charging [129, 127, 137, 70, 132]. However, discharging supercapacitors is often a critical step in many applications in which fast energy delivery is required, such as supplying energy to portable electronic equipment, camera flash lights or car starters. The dynamic pore charge of the capacitor when the voltage is abruptly switched to $0\,\mathrm{V}$ can be seen in Figure 9.16. In the plot, $Q_{\mathrm{equ}}$ is the accumulated charge in equilibrium for the fully charged supercapacitor at applied voltage $U = 3\,\mathrm{V}$. $\tau_{\mathrm{dis}}$ is the time needed by the supercapacitor to discharge to $5\%$ of $Q_{\mathrm{equ}}$. In the simulation, switching off the voltage means to disable the external field between the electrodes. The ICC* calculation remains active which preserves the induced charge on the carbon atoms due to the separated ion configuration. In a circuit, the potential difference of $0\,\mathrm{V}$ is attained by grounding both poles of the capacitor.

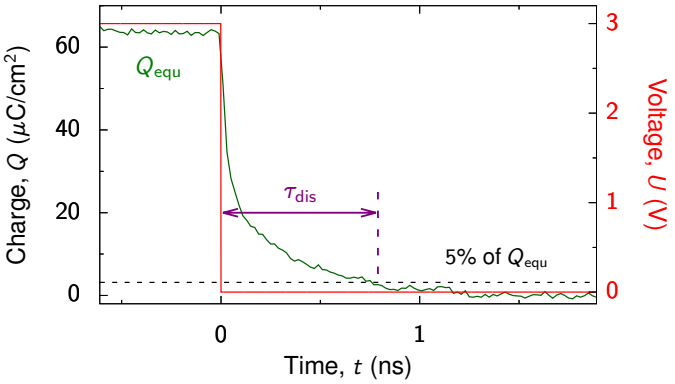


Figure 9.16: Time evolution of the accumulated charge $Q$ during step-discharging for a pore length of $l = 8\,\mathrm{nm}$.

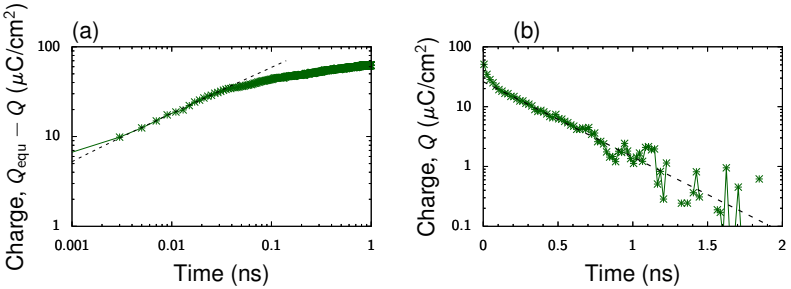


Figure 9.17: Time regimes of the average pore charge $Q(t)$ in the discharging process. Plot (a) is shown as $Q_{equ} - Q(t)$ to see the fit $a\sqrt{t}$ as a straight line in double logarithmic scale.

Similar to the charging regimes in Figure 9.5, the detailed discharge behavior is shown in Figure 9.17. At short times, a square-root regime (a) is observed followed by an exponential saturation at long times (b). Symbols show the results of averaged MD simulations, the dashed lines show the fitting results by functions $a\sqrt{t}$ in (a) and

$A\exp(-t/\tau)$ in (b). The square-root and exponential regimes again suggest that the discharge process is driven by diffusion. As the pore initially is filled with (former) counterions only, the diffusion is collective, meaning that the particles migrating out of the pore are coupled by the screened electrostatic repulsion.

### 9.5.1 Pore length dependence of the discharge time

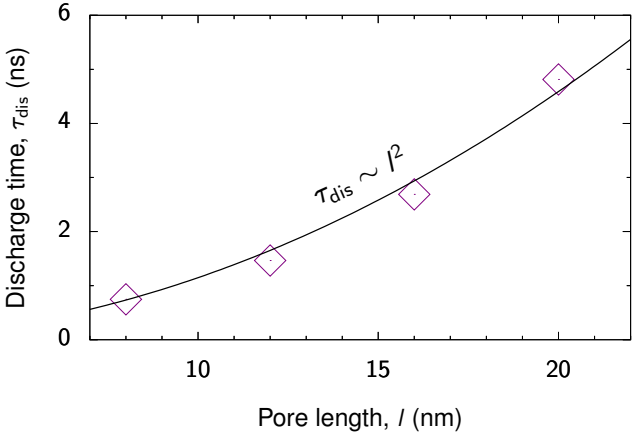


Figure 9.18: Discharging time $\tau_{\mathrm{dis}}$ as a function of pore length $l$. The diffusive character of discharging results in $\tau_{\mathrm{dis}} \propto l^2$.

The discharge time after switching off the applied voltage for pores with lengths between $8\,\mathrm{nm}$ to $20\,\mathrm{nm}$ is shown in Figure 9.18. Considering a collective diffusional process, the discharge time depends on the pore length as

$$\tau_{\mathrm{dis}} = Bl^2, \tag{9.2}$$

where $B$ is a constant reflecting ion diffusivity, whose value can be fixed by a single simulation. Note that $B$ depends on the accumulated charge and therefore on the

working voltage. The pore length dependence of Eq. 9.2 accurately fits the simulations results. By extrapolation, it allows to determine discharge times for long pores by calculating $\tau_{\mathrm{dis}}$ for shorter pores that are computationally more easily accessible.

### 9.5.2 Accelerated discharging

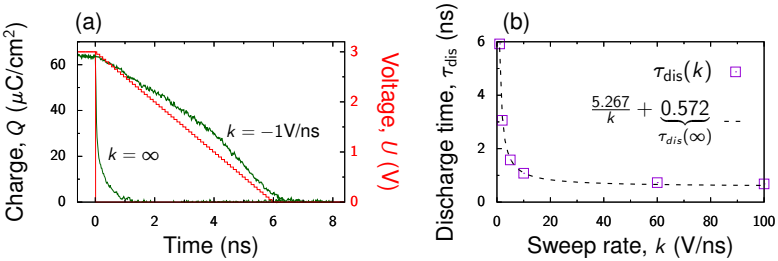


Figure 9.19: Discharging supercapacitor with different sweep rates. Plot (a) shows the charge as a function of time for step-voltage ($k = \infty$) and for linear sweep discharge with the sweep rate $k = -1\,\mathrm{V\,ns^{-1}}$. (b) shows discharge times $\tau_{\mathrm{dis}}$ versus sweep rate $k$ and a fit through the simulation data. $\tau_{\mathrm{dis}}$ increases inversely with with the sweep rate, showing that discharging is fastest when the voltage is turned off in a step-like fashion.

Motivated by the success of the sweep voltage charging, one might be tempted to apply a similar strategy to discharging. The comparison in Figure 9.19 (a) between a voltage step ($3\,\mathrm{V} \to 0\,\mathrm{V}$) and linear discharging (with $k = -1\,\mathrm{V\,ns^{-1}}$) suggests that discharging is fastest when the voltage is switched off in a step-like fashion. When probing the discharge behavior with different sweep rates in Figure 9.19 (b), the discharge time $\tau_{\mathrm{dis}}(k)$ can be fitted to

$$\tau_{\mathrm{dis}}(k) = \frac{5.267\,\mathrm{V}}{k} + 0.572\,\mathrm{ns}$$

and never deceeds the limit of $0.572\,\mathrm{ns}$ for $k \to \infty$. So compared to a linear discharge sweep, it is always faster to switch off the voltage and give the system enough time to discharge to an acceptable degree (e.g. to $5\%$ of the accumulated charge as in Fig.

9.16). This is understandable as discharging is driven essentially by collective ion diffusion out of the pore and there is no process that can lead to overfilling or any other effect hindering this diffusion, which could have been cured by a voltage sweep.

## 9.6 Optimal electrode thickness

Instead of optimizing supercapacitors by minimizing the charge-discharge times for a given electrode configuration, it is also possible to match the *pore length* (i.e. the thickness of a porous electrode) to a required working frequency, $w = 2\pi/T$, where $T = t_{\text{charge}} + \tau_{\text{dis}}$. In this case, the optimal pore length is found using Equations 9.2 and 9.1 with $t_{\text{charge}} = U/k_{\text{opt}}$, where $U$ is the working voltage:

$$l_{\text{opt}}(U, w) = \sqrt{\frac{2\pi/w}{A(U)U + B(U)}}. \tag{9.3}$$

With this strategy, supercapacitor optimization amounts to finding the charge and discharge parameters $A$ and $B$ by fitting the experimental or simulation data to Equations 9.1 and 9.2, respectively, and building electrodes with the pores of length $l_{\text{opt}}$. The pore length can also be optimized for charge or discharge alone, depending on what is the critical step in a specific application, which corresponds to setting $A$ or $B$ to zero in Equation 9.3. While porous electrodes with well-defined slit pores do exist [138, 139], many porous materials consist of interconnected networks of short pores [114], or may have a wide pore width and length polydispersity. In this case, however, since charging and discharging are still mainly diffusive processes, Equations 9.1 and 9.2 are expected to hold, but with some 'effective' (averaged) parameters $A$ and $B$ representing the whole electrode. If the electrode thickness (e.g. the size of a carbide-derived carbon particle) is known, the parameters $A$ and $B$ can be determined directly from Equations 9.1 and 9.2. This strategy and Equation 9.3 can be applied to find the optimal thickness of an electrode for a given voltage. Inversely, knowing the optimal frequency for a given electrode allows to determine its thickness through the knowledge of $A$ and $B$.

## 9.7 Charge cycles

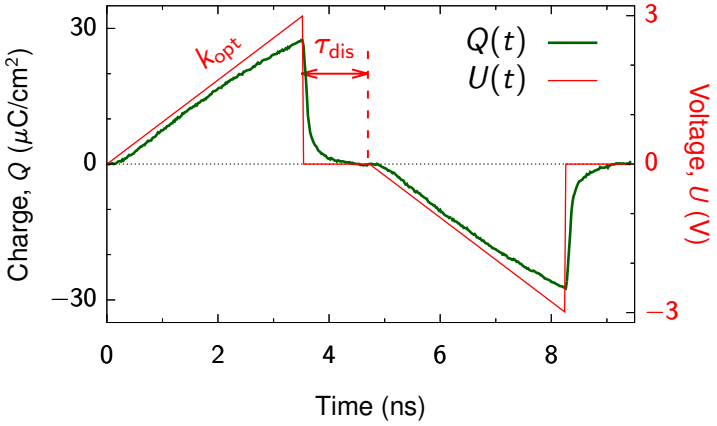


Figure 9.20: Pore charge of the fully optimized, bipolar cycle with a linear sweep $k = \pm 0.875\,\mathrm{V\,ns^{-1}}$ and step discharging.

Figure 9.20 summarizes the findings in the form of an optimal charge-discharge cycle. The cycle consists of a linear sweep to $U = 3\,\mathrm{V}$ with the rate $k_{\mathrm{opt}} = 0.875\,\mathrm{V\,ns^{-1}}$, followed by switching off the voltage in a step-like fashion. The next cycle (here to the negative potential $-3\,\mathrm{V}$) begins after waiting at $0\,\mathrm{V}$ for $\tau_{\mathrm{dis}} \approx 1.2\,\mathrm{ns}$, which allows the system to discharge to an acceptable degree. If the preferable cycle is $U \to -U \to U \cdots$ as in Figure 9.20 rather than $U \to 0 \to U \cdots$, it is nevertheless advantageous first to discharge a supercapacitor and only then to sweep the voltage to $-U$ with the same rate $k_{\mathrm{opt}}$. By switching the voltage directly from $U \to -U$, all in-pore counterions suddenly become co-ions trapped inside the pores. Such a 'trapping catastrophe', shown in Figure 9.21 leads to very slow charging rates.

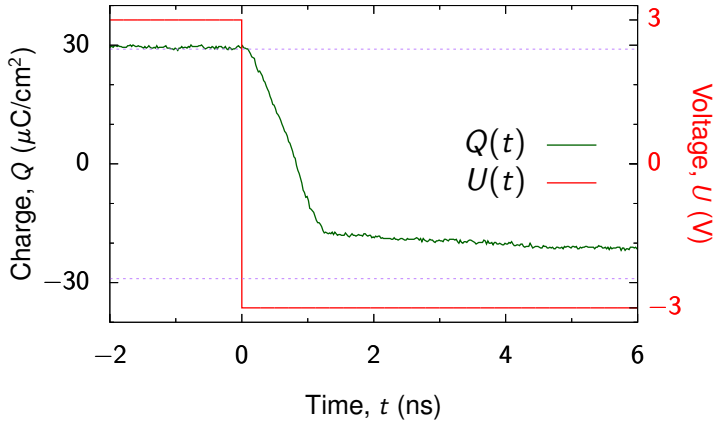


Figure 9.21: Pore charge of a bipolar cycle. Using a voltage step $U \rightarrow -U$ suddenly inverses the roles of co- and counterions and leads to a 'trapping catastrophe'.

## 9.8 Pore length extrapolation

It is instructive to estimate the parameters of the optimal circle for real electrodes and ionic liquids. As an example, the simulations are compared to experimental results using the ionic liquid OMIM TFSI and porous electrodes of thickness $120\,\mu\mathrm{m}$ [80]. Equation 9.1 would allow to directly calculate the optimal sweep rate with the simulation result $A \approx 1.67 \times 10^{-4}\,\mathrm{ns\,V^{-1}\,\AA^2}$ obtained by fitting $k_{opt}(l)$ for a number of pore lengths. However, since this value has been obtained for charged soft spheres (charged WCA particles), which are much less viscous than OMIM TFSI, $A$ is rescaled by the ratio of the *bulk* diffusion coefficients $D_{\mathrm{WCA}}/D_{\mathrm{OMIM\text{-}TFSI}} \approx 17333$, in order to get a rough estimate for the linear sweep parameter $A$ for OMIM TFSI. After straightforward transformations it is found that $k_{\mathrm{opt}} \approx 0.24\,\mathrm{mV\,s^{-1}}$ for the pore length $l = 120\,\mu\mathrm{m}$ and the applied potential $U = 3\,\mathrm{V}$. This value is in fairly good agreement with the experi-

mental results, showing the saturation of capacitance at comparable sweep rates [80]. For the discharge parameter in Equation 9.2 the simulations give $B \approx 0.0115\,\mathrm{ns\,nm^{-2}}$, which becomes $B \approx 198.9\,\mathrm{ns\,nm^{-2}}$ after rescaling for OMIM TFSI. This yields for the discharge time $\tau\mathrm{dis} \approx 47.7\,\mathrm{min}$ of the fully charged $120\,\mu\mathrm{m}$ thick electrode. Remarkably, the discharge time is approximately $4.36$ times shorter than the charging time $t_{\mathrm{charge}} \approx 208\,\mathrm{min}$ at optimal sweep rate $0.24\,\mathrm{mV\,s^{-1}}$. This strong asymmetry suggests that different strategies to optimization must be taken depending on what is the critical step in a particular application.

## 9.9 Conclusions

The kinetic behavior of step-voltage charging is governed by a potential-driven linear and a square-root diffusive charge accumulation, followed by two exponential regimes. During the fast linear stage, the adsorbed counterions compress the in-pore ionic liquid, creating a crowded neutral phase inside the pores, which leads to strong co-ion trapping and consequently slow charging. It has been suggested that reducing the affinity of pores towards ions can help avoid overfilling and thus accelerate charging [129, 127]. However, such ionophobic pores still remain a challenge for material scientists and engineers. Another possibility to speed up charging is to use electrodes with sufficiently wide pores to the detriment of capacitance and energy density [2, 1, 3, 4].

It is found that for the charging process, an 'acceleration by slowing-down' can be realized using linear sweep voltammetry. This prevents the formation of the crowded phase and avoids co-ion trapping. Dynamical MD simulations were used to determine the *optimal* sweep rates $k_{\mathrm{opt}}$ which minimize the charging times. Further simulations showed that $k_{\mathrm{opt}} \sim l^{-2}$, where $l$ is the pore length or electrode thickness. Conversely, the best *discharge* rates are obtained when the voltage is turned off in a step-like fashion, while the discharge times $\tau_{\mathrm{dis}} \sim l^2$. These scaling relations are consistent with the mainly diffusive character of charge-discharge dynamics and, importantly, they allow one to predict optimal cycles for arbitrary thick electrodes. Interestingly, the optimal charge-

discharge times are strikingly different, discharging is more than four times faster than charging. This time asymmetry suggests that separate Ragone plots for charging and discharging are needed to fully describe the energy-power relation for supercapacitors.

# 10 Cross-system conclusions

A cross-comparison of the three capacitor systems investigated in this work has to account for the different scenarios of flat (Chapter 5), CDC (Chapter 6) and slit-like (Chapters 7, 8 and 9) electrodes. Therefore, a suitable normalization of the capacitance is needed, either given per surface area, carbon mass or pore volume. Especially for the parallel plate capacitor, this is not straightforward to do and requires a mapping of the simulation domain to a macroscopic system. A minimal setup would consist of graphene sheets and space for the electrolyte. A separation layer is needed that prevents short circuits of opposing electrodes under mechanical stress, followed again by electrolyte space and the counter electrode. For a macroscopic device, this structure needs to be continued in a space-filling way, either by stacking or rolling of the basic layers. Both would result in direct contact of oppositely charged electrodes, so another isolation layer behind the electrodes is needed. These requirements create a large uncertainty of the final physical dimensions and aggravates the comparison of capacitance per volume or weight to other systems. A more reliable capacitance normalization in this setup therefore is by surface area of the graphene sheets. However, in nanoporous electrodes like the CDC setup, it is difficult to accurately specify the surface area or accessible volume because of the amourphous atomic carbon structure. Here, a definition of specific capacitance per electrode mass is a reliable measure. Lastly, in the slitpore setup, pore volume, surface area and electrode mass in principle all are available quantities. The uncertainty here is due to the usage of soft interaction potentials and the hexagonal carbon pattern, whose accessible surface area deviates from a flat wall. Note that similar to the flat electrodes, it is unclear how the slitpores could be assembled to a macroscopic capacitor device. Here, only the region inside the pore is

taken into account when analyzing the accumulated charge assuming a space-filling, macroscopic continuation of the slits.

| Electrode | Electrolyte | Voltage (V) | $C/M$ (F g$^{-1}$) | $C/A$ (µF cm$^{-2}$) | $C/V$ (F cm$^{-3}$) |
|---|---|---|---|---|---|
| Planar | BMIM $PF_6$ | 1.2 | 15.31 | 3.54 | 7.14 |
| CDC | EMIM $BF_4$ | 1.2 | 122.0 | 5.81 | 108.24 |
| Slitpore | BMIM $PF_6$ | 2.0 | 41.96 | 2.71 | 45.16 |
| Slitpore | Model IL | 2.0 | 171.46 | 11.07 | 184.57 |

Table 10.1: Specific capacitance normalized by weight, surface area and volume of the different simulation models.

A comparison of integral capacitance values normalized by weight, surface area and volume is shown in Table 10.1 for the three scenarios. The non-normalized capacitance at a given half-cell voltage $V$ is calculated via

$$C = \frac{\langle Q_L \rangle + \langle Q_R \rangle}{2V} \tag{10.1}$$

using the mean of accumulated charges on the two electrodes $\langle Q_L \rangle$ and $\langle Q_R \rangle$. For normalization by mass, the pure carbon weight of a single electrode is used neglecting the electrolyte. In case of the planar electrodes, all three graphene sheets used in the simulations are taken into account. The electrode area in this case is the lateral surface of the simulation box $A = 27.2\,\text{Å} \times 30.0\,\text{Å}$, the volume is chosen to be half the box $V = A \times 73.92\,\text{Å}$. In the CDC system, surface area and volume of the electrodes are obtained by binning the electrode region and probing the bins with hard particles of diameter $5.5\,\text{Å}$ for overlap with carbon atoms. For the slitpore, a system with pore length $80\,\text{Å}$ and width $6\,\text{Å}$ is chosen. Table 10.1 shows that the various geometries, electrolytes and normalizations lead to quite different capacitance values that have to be put into perspective:

- The planar electrode overall shows the worst performance. Taking into account only a single graphene sheet would lead to a threefold increase and a value of

$C/M = 45.93\,\mathrm{F\,g^{-1}}$ for the capacitance per electrode weight. Also $C/V$ is the lowest in the planar case due to the uncertainty in the accounted volume and poses a rather poor quantity for the cross-system comparison. Thus, the capacitance per area gives the most reliable comparison, a reduced capacitance here can is expected due to the fact that the electrolyte structure in the non-confined case doesn't benefit from screened electrostatics of the superionic state found in nanoporous systems.

- The CDC electrodes with EMIM $BF_4$ outperforms the slitpore electrode with BMIM $PF_6$, using the model IL for the slitpore however reverses this trend.

- Comparing the two electrolytes of the slitpore simulations shows a consistent increase in capacitance by a factor of 4 for all specific capacitance values. The last two points highlight that the size of the ions has a large impact on the capacitance.

- Another fundamental difference between slitpore and CDC system is that in the latter case, the carbon walls can be approached by the ions from front and back, whereas the region outside the pore is considered metallic and particle free in the slitpore setup. This gets important for the capacitance per weight and surface area, as the slitpore needs double the amount of carbon atoms to construct the pore.

- Finally, the model IL expectedly overestimate the capacitance, again attributed to the reduced size of the model compared to the coarse grained ILs.

Considering the voltage dependence of various observables throughout the systems, it becomes apparent that certain effects vanish or lose importance for increasing applied potential. This can be found in the comparison the systems with smooth and atomically structured electrodes, showing similar values for the differential capacitance at higher potentials in Figure 5.4. It is also visible in the slitpore system, where the in-pore packing fraction (Fig. 8.13), the charging mechanism (Fig. 8.14) and differential

capacitance (Fig. 8.15) match at higher voltage for systems with a large range of IL concentrations. The general physical picture here is that the energy gain of charged species given by a electric potential difference overrules entropic contributions due to structural features of the electrode. A similar theme can be found concerning the initial electrolyte density (discussed in Chapters 7 and 8) or solvent concentration (discussed in Chapter 6): Both have only little influence on the stored charge and capacitance in case of an applied voltage. This suggests that a reduction of ionic liquid concentration can be advantageous for supercapacitors.

# Bibliography


[1] E. Raymundo-Piñero, K. Kierczek, J. Machnikowski, and F. Béguin. "Relationship between the nanoporous texture of activated carbons and their capacitance properties in different electrolytes." *Carbon* 44 (2006), pp. 2498–2507.

[2] J. Chmiola, G. Yushin, Y. Gogotsi, C. Portet, P. Simon, and P. L. Taberna. "Anomalous Increase in Carbon Capacitance at Pore Sizes Less Than 1 Nanometer." *Science* 313 (2006), p. 1760.

[3] C. Largeot, C. Portet, J. Chmiola, P.-L. Taberna, Y. Gogotsi, and P. Simon. "Relation between the Ion Size and Pore Size for an Electric Double-Layer Capacitor." *Journal of the American Chemical Society* 130.9 (2008), pp. 2730–2731.

[4] S. Kondrat, C. R. Pérez, V. Presser, Y. Gogotsi, and A. A. Kornyshev. "Effect of pore size and its dispersity on the energy storage in nanoporous supercapacitors." *Energy & Environmental Science* 5 (2012), p. 6474.

[5] P. Simon and Y. Gogotsi. "Materials for electrochemical capacitors." *Nature materials* 7.11 (2008), pp. 845–854.

[6] P. Wu, J. Huang, V. Meunier, B. Sumpter, and R. Qiao. "Voltage Dependent Charge Storage Modes and Capacity in Sub-nanometer Pores." *Journal of Physical Chemistry Letters* 3 (2012), pp. 1732–1737.

[7] J. Vatamanu, Z. Hu, D. Bedrov, C. Perez, and Y. Gogotsi. "Increasing Energy Storage in Electrochemical Capacitors with Ionic Liquid Electrolytes and

Nanostructured Carbon Electrodes." *Journal of Physical Chemistry Letters* 4 (2013), p. 2829.

[8] M. Beidaghi and Y. Gogotsi. "Capacitive Energy Storage in Micro-scale Devices: Recent Advances in Design and Fabrication of Micro-supercapacitors." *Energy & Environmental Science* 7 (3 2014), pp. 867–884.

[9] J. Vatamanu, M. Vatamanu, and D. Bedrov. "Non-Faradic Energy Storage by Room Temperature Ionic Liquids in Nanoporous Electrodes." *ACS Nano* 9 (2015), p. 5999.

[10] R. Burt, K. Breitsprecher, B. Daffos, P.-L. Taberna, P. Simon, G. Birkett, X. S. Zhao, C. Holm, and M. Salanne. "Capacitance of Nanoporous Carbon-Based Supercapacitors Is a Trade-Off between the Concentration and the Separability of the Ions." *The Journal of Physical Chemistry Letters* 7.19 (2016), pp. 4015–4021.

[11] M. Salanne, B. Rotenberg, K. Naoi, K. Kaneko, P.-L. Taberna, C. P. Grey, B. Dunn, and P. Simon. "Efficient Storage Mechanisms for Building Better Supercapacitors." *Nature Energy* 1 (2016), p. 16070.

[12] A. C. Forse, C. Merlet, J. M. Griffin, and C. P. Grey. "New Perspectives on the Charging Mechanisms of Supercapacitors." *Journal of the American Chemical Society* 138 (2016), pp. 5731–5744.

[13] P. Simon and Y. Gogotsi. "Capacitive Energy Storage in Nanostructured Carbon-Electrolyte Systems." *Accounts of Chemical Research* 46 (2013), pp. 1094–1103.

[14] J. R. Miller and P. Simon. "Materials Science ? Electrochemical Capacitors for Energy Management." *Science* 321 (2008), pp. 651–652.

[15] B. E. Conway. *Electrochemical supercapacitors: scientific fundamentals and technological applications*. Springer Science & Business Media, 2013.

[16] K. R. Seddon. "A taste of the future." *Nature Materials* 2 (2003), p. 363.

[17] J. M. S. S. Esperança, J. N. Canongia Lopes, M. Tariq, L. M. N. B. F. Santos, J. W. Magee, and L. P. N. Rebelo. "Volatility of aprotic ionic liquids - a review." *Journal of Chemical and Engineering Data* 55.1 (2009), pp. 3–12.

[18] M. J. Earle, J. M. Esperança, M. A. Gilea, J. N. C. Lopes, L. P. Rebelo, J. W. Magee, K. R. Seddon, and J. A. Widegren. "The distillation and volatility of ionic liquids." *Nature* 439.7078 (2006), p. 831.

[19] W. Zhao, H. Eslami, W. L. Cavalcanti, and F. Müller-Plathe. "A Refined All-Atom Model for the Ionic Liquid 1-n-Butyl 3-Methylimidazolium bis(Trifluoromethylsulfonyl)imide [bmim][$Tf_2N$]." *Zeitschrift für physikalische Chemie* 221 (2007), pp. 1647–1662.

[20] R. P. Swatloski, S. K. Spear, J. D. Holbrey, and R. D. Rogers. "Dissolution of Cellose with Ionic Liquids." *Journal of the American Chemical Society* 124.18 (2002), pp. 4974–4975.

[21] J. N. Canongia Lopes and A. A. H. Pádua. "Molecular Force Field for Ionic Liquids III: Imidazolium, Pyridinium, and Phosphonium Cations; Chloride, Bromide, and Dicyanamide Anions." *Journal of Physical Chemistry B* 110.39 (2006), pp. 19586–19592.

[22] V. V. Chaban, I. V. Voroshylova, O. N. Kalugin, and O. V. Prezhdo. "Acetonitrile Boosts Conductivity of Imidazolium Ionic Liquids." *The Journal of Physical Chemistry* (2012).

[23] J. Zhang, W. Wu, T. Jiang, H. Gao, Z. Liu, J. He, and B. Han. "Conductivities and Viscosities of the Ionic Liquid [bmim][PF6] + Water + Ethanol and [bmim][PF6] + Water + Acetone Ternary Mixtures." *Journal of Chemical and Engineering Data* 48.5 (2003), pp. 1315–1317.

[24] D. Roy and M. Maroncelli. "An Improved Four-Site Ionic Liquid Model." *Journal of Physical Chemistry B* 114.39 (2010), pp. 12629–12631.

[25] K. Breitsprecher, K. Szuttor, and C. Holm. “Electrode Models for Ionic Liquid-Based Capacitors.” *The Journal of Chemical Physics C* 119 (2015), pp. 22445–22451.

[26] C. Pean, B. Daffos, B. Rotenberg, P. Levitz, M. Haefele, P. L. Taberna, P. Simon, and M. Salanne. “Confinement, Desolvation, and Electrosorption Effects on the Diffusion of Ions in Nanoporous Carbon Electrodes.” *Journal of the American Chemical Society* 137.39 (2015), pp. 12627–12632.

[27] C. Merlet, M. Salanne, B. Rotenberg, and P. A. Madden. “Imidazolium Ionic Liquid Interfaces with Vapor and Graphite: Interfacial Tension and Capacitance from Coarse-Grained Molecular Simulations.” *The Journal of Physical Chemistry C* 115.33 (2011), pp. 16613–16618.

[28] A. David, O. Y. Fajardo, A. A. Kornyshev, M. Urbakh, and F. Bresme. “Electrotunable Lubricity with Ionic Liquids: the Influence of Nanoscale Roughness.” *Faraday Discussions* 199 (0 2017), pp. 279–297.

[29] C. Liu, Z. Yu, D. Neff, A. Zhamu, and B. Z. Jang. “Graphene-Based Supercapacitor with an Ultrahigh Energy Density.” *Nano Letters* 12 (2010), pp. 4863–4868.

[30] R. Kühne. “Electric buses–An energy efficient urban transportation means.” *Energy* 35.12 (2010), pp. 4510–4513.

[31] A. Rufer, D. Hotellier, and P. Barrade. “A supercapacitor-based energy storage substation for voltage compensation in weak transportation networks.” *IEEE Transactions on power delivery* 19.2 (2004), pp. 629–636.

[32] P. Simon, Y. Gogotsi, and B. Dunn. “Where do batteries end and supercapacitors begin?” *Science* 343.6176 (2014), pp. 1210–1211.

[33] A. González-Gil, R. Palacin, and P. Batty. “Sustainable urban rail systems: Strategies and technologies for optimal management of regenerative braking energy.” *Energy conversion and management* 75 (2013), pp. 374–388.

[34] M. Notarianni, J. Liu, F. Mirri, M. Pasquali, and N. Motta. “Graphene-based supercapacitor with carbon nanotube film as highly efficient current collector.” *Nanotechnology* 25.43 (2014), p. 435405.

[35] J. Liu, F. Mirri, M. Notarianni, M. Pasquali, and N. Motta. “High performance all-carbon thin film supercapacitors.” *Journal of Power Sources* 274 (2015), pp. 823–830.

[36] Z.-l. Yang, H. Wang, Y.-c. Peng, and H.-h. Xu. “Design of solar street lamp system with supercapacitors as energy storage device [J].” *Renewable Energy Resources* 2 (2009), p. 018.

[37] T. Chen and L. Dai. “Carbon nanomaterials for high-performance supercapacitors.” *Materials Today* 16.7-8 (2013), pp. 272–280.

[38] X. Lu, T. Zhai, X. Zhang, Y. Shen, L. Yuan, B. Hu, L. Gong, J. Chen, Y. Gao, J. Zhou, et al. “WO3–x@ Au@ MnO2 Core–Shell Nanowires on Carbon Fabric for High-Performance Flexible Supercapacitors.” *Advanced materials* 24.7 (2012), pp. 938–944.

[39] J. Bae, M. K. Song, Y. J. Park, J. M. Kim, M. Liu, and Z. L. Wang. “Fiber supercapacitors made of nanowire-fiber hybrid structures for wearable/flexible energy storage.” *Angewandte Chemie International Edition* 50.7 (2011), pp. 1683–1687.

[40] H. Helmholtz. “Ueber einige Gesetze der Vertheilung elektrischer Ströme in körperlichen Leitern mit Anwendung auf die thierisch-elektrischen Versuche.” *Annalen der Physik* 165 (1853), pp. 211–233.

[41] P. Debye and E. Hückel. “Zur Theorie der Elektrolyte. I. Gefrierpunktserniedrigung und verwandte Erscheinungen.” *Physikalische Zeitschrift* 24.9 (1923), p. 185.

[42] G. L. Gouy. “Sur la constitution de la charge électrique à la surface d’un électrolyte.” *Journal de Physique* 9 (1910), p. 457.

[43] V. S. Bagotsky. *Fundamentals of Electrochemistry*. 2nd ed. Wiley, 2005.

[44] J. Bikerman. "XXXIX. Structure and capacity of electrical double layer." *The London, Edinburgh, and Dublin Philosophical Magazine and Journal of Science* 33.220 (1942), pp. 384–397.

[45] V. Freise. "Zur theorie der diffusen doppelschicht." *Zeitschrift für Elektrochemie, Berichte der Bunsengesellschaft für physikalische Chemie* 56.8 (1952), pp. 822–827.

[46] M. Eigen and E. Wicke. "The thermodynamics of electrolytes at higher concentration." *The Journal of Physical Chemistry* 58.9 (1954), pp. 702–714.

[47] M.-J. Huang, J. Schofield, and R. Kapral. "A microscopic model for chemically-powered Janus motors." *Soft Matter* (2016).

[48] V. Lockett, R. Sedev, J. Ralston, M. Horne, and T. A.Rodopoulos. "Differential Capacitance of the Electrical Double Layer in Imidazolium-Based Ionic Liquids: Influence of Potential, Cation Size, and Temperature." *Journal of Physical Chemistry C* 112 (2008), pp. 7486–7495.

[49] J. Vatamanu, O. Borodin, and G. D. Smith. "Molecular Insights into the Potential and Temperature Dependences of the Differential Capacitance of a Room-Temperature Ionic Liquid at Graphite Electrodes." *Journal of the American Chemical Society* 132.42 (2010), pp. 14825–14833.

[50] A. A. Kornyshev, D. J. Lee, S. Leikin, and A. Wynveen. "Structure and interactions of biological helices." *Reviews of Modern Physics* 79.3, 943 (2007), p. 943.

[51] K. Breitsprecher, P. Košovan, and C. Holm. "Coarse grained simulations of an ionic liquid-based capacitor II: asymmetry in ion shape and charge localization." *Journal of Physics: Condensed Matter* 26 (2014), p. 284114.

[52] K. Breitsprecher, P. Košovan, and C. Holm. "Coarse grained simulations of an ionic liquid-based capacitor I: density, ion size, and valency effects." *Journal of Physics: Condensed Matter* 26 (2014), p. 284108.

[53] R. Atkin, S. Z. El Abedin, R. Hayes, L. H. S. Gasparotto, N. Borisenko, and F. Endres. "AFM and STM Studies on the Surface Interaction of [BMP]TFSA and (EMIm]TFSA Ionic Liquids with Au(111)." *Journal of Physical Chemistry C* 113.30 (2009), pp. 13266–13272.

[54] D. E. Jiang, Z. H. Jin, and J. Z. Wu. "Oscillation of Capacitance inside Nanopores." *Nano Letters* 11 (2011), pp. 5373–5377.

[55] G. Feng and P. T. Cummings. "Supercapacitor Capacitance Exhibits Oscillatory Behavior as a Function of Nanopore Size." *Journal of Physical Chemistry Letters* 2 (2011), pp. 2859–2864.

[56] P. Wu, J. Huang, V. Meunier, B. G. Sumpter, and R. Qiao. "Complex Capacitance Scaling in Ionic Liquids-Filled Nanopores." *ACS Nano* 5 (2011), pp. 9044–9051.

[57] L. Xing, J. Vatamanu, O. Borodin, and D. Bedrov. "On the Atomistic Nature of Capacitance Enhancement Generated by Ionic Liquid Electrolyte Confined in Subnanometer Pores." *Journal of Physical Chemistry Letters* 4 (2013), p. 132.

[58] C. C. Rochester, A. A. Lee, G. Pruessner, and A. A. Kornyshev. "Interionic Interactions in Electronically Conducting Confinement." *ChemPhysChem* 16.14 (2013), p. 4121.

[59] A. Goduljan, F. Juarez, L. Mohammadzadeh, P. Quaino, E. Santos, and W. Schmickler. "Screening of ions in carbon and gold nanotubes – A theoretical study." *Electrochemistry Communications* 45 (2014), pp. 48–51.

[60] L. Mohammadzadeh, A. Goduljan, F. Juarez, P. Quaino, E. Santos, and W. Schmickler. "Nanotubes for charge storage ? towards an atomistic model." *Electrochimica Acta* 162 (2015), pp. 11–16.

[61] S. Kondrat and A. Kornyshev. “Superionic state in double-layer capacitors with nanoporous electrodes.” *Journal of Physics: Condensed Matter* 23.2 (2011), p. 022201.

[62] S. Kondrat, N. Georgi, M. V. Fedorov, and A. A. Kornyshev. “A superionic state in nano-porous double-layer capacitors: insights from Monte Carlo simulations.” *Physical Chemistry Chemical Physics* 13 (2011), pp. 11359–11366.

[63] A. Arnold, J. de Joannis, and C. Holm. “Electrostatics in Periodic Slab Geometries I.” *Journal of Chemical Physics* 117 (2002), pp. 2496–2502.

[64] J. de Joannis, A. Arnold, and C. Holm. “Electrostatics in Periodic Slab Geometries II.” *Journal of Chemical Physics* 117 (2002), pp. 2503–2512.

[65] S. Tyagi, A. Arnold, and C. Holm. “Electrostatic layer correction with image charges: A linear scaling method to treat slab 2D + h systems with dielectric interfaces.” *Journal of Chemical Physics* 129.20, 204102 (2008), p. 204102.

[66] A. Arnold, K. Breitsprecher, F. Fahrenberger, S. Kesselheim, O. Lenz, and C. Holm. “Efficient Algorithms for Electrostatic Interactions Including Dielectric Contrasts.” *Entropy* 15.11 (2013), pp. 4569–4588.

[67] C. Tyagi, M. Süzen, M. Sega, M. Barbosa, S. S. Kantorovich, and C. Holm. “An iterative, fast, linear-scaling method for computing induced charges on arbitrary dielectric boundaries.” *The Journal of Chemical Physics* 132 (2010), p. 154112.

[68] H. J. Limbach, A. Arnold, B. A. Mann, and C. Holm. “ESPResSo – An Extensible Simulation Package for Research on Soft Matter Systems.” *Computer Physics Communications* 174.9 (2006), pp. 704–727.

[69] A. Arnold, O. Lenz, S. Kesselheim, R. Weeber, F. Fahrenberger, D. Röhm, P. Košovan, and C. Holm. “ESPResSo 3.1 — Molecular Dynamics Software for Coarse-Grained Models.” *Meshfree Methods for Partial Differential Equations VI*. Ed. by M. Griebel and M. A. Schweitzer. Vol. 89. Lecture Notes in Com-

putational Science and Engineering. Springer Berlin Heidelberg, 2013, pp. 1–23.

[70] C. Péan, C. Merlet, B. Rotenberg, P. A. Madden, P.-L. Taberna, B. Daffos, M. Salanne, and P. Simon. "On the dynamics of charging in nanoporous carbon-based supercapacitors." *ACS Nano* 8.2 (2014), pp. 1576–1583.

[71] M. Cole and J. Klein. "The interaction between noble gases and the basal plane surface of graphite." *Surface Science* (1983).

[72] F. F. Abraham and Y. Singh. "The structure of a hard-sphere fluid in contact with a soft repulsive wall." *The Journal of Chemical Physics* (1977).

[73] W. A. Steele. "The physical interaction of gases with crystalline solids: I. Gas-solid energies and properties of isolated adsorbed atoms." *Surface Science* 36.1 (1973), pp. 317–352.

[74] W. A. Steele. "The interaction of rare gas atoms with graphitized carbon black." *Journal of Physical Chemistry* 82.7 (1978), pp. 817–821.

[75] D. Roy, N. Patel, S. Conte, and M. Maroncelli. "Dynamics in an Idealized Ionic Liquid Model." *Journal of Physical Chemistry B* 114.25 (2010), pp. 8410–8424.

[76] R. Hayes, G. G. Warr, and R. Atkin. "Structure and Nanostructure in Ionic Liquids." *Chemical Reviews* 115.13 (2015), pp. 6357–6426.

[77] P. Holoborodko. *Smooth Noise Robust Differentiators*. http://www.holoborodko.com/pavel/numerical-methods/numerical-derivative/smooth-low-noise-differentiators. 2008.

[78] C. Merlet, C. Péan, B. Rotenberg, P. A. Madden, P. Simon, and M. Salanne. "Simulating Supercapacitors: Can We Model Electrodes As Constant Charge Surfaces?" *The Journal of Physical Chemistry Letters* 4.2 (2013), pp. 264–268.

[79] Z. Wang, Y. Yang, D. L. Olmsted, M. Asta, and B. B. Laird. “Evaluation of the constant potential method in simulating electric double-layer capacitors.” *The Journal of Chemical Physics* 141.18, 184102 (2014), p. 184102.

[80] B. Dyatkin, N. C. Osti, Y. Zhang, H.-W. Wang, E. Mamontov, W. T. Heller, P. Zhang, G. Rother, P. T. Cummings, D. J. Wesolowski, and Y. Gogotsi. “Ionic Liquid Structure, Dynamics, and Electrosorption in Carbon Electrodes with Bimodal Pores and Heterogeneous Surfaces.” *Carbon* 129 (2018), pp. 104–118.

[81] C. Merlet, B. Rotenberg, P. A. Madden, P.-L. Taberna, P. Simon, Y. Gogotsi, and M. Salanne. “On the molecular origin of supercapacitance in nanoporous carbon electrodes.” English. *Nature Materials* 11.4 (2012), pp. 306–310.

[82] C. Merlet, C. Péan, B. Rotenberg, P. A. Madden, B. Daffos, P.-L. Taberna, P. Simon, and M. Salanne. “Highly confined ions store charge more efficiently in supercapacitors.” *Nature communications* 4 (2013).

[83] C. Péan, B. Daffos, C. Merlet, B. Rotenberg, P.-L. Taberna, P. Simon, and M. Salanne. “Single Electrode Capacitances of Porous Carbons in Neat Ionic Liquid Electrolyte at 100[degree] C: A Combined Experimental and Modeling Approach.” *Journal of The Electrochemical Society* 162.5 (2015), A5091–A5095.

[84] J. Palmer, A. Llobet, S.-H. Yeon, J. Fischer, Y. Shi, Y. Gogotsi, and K. Gubbins. “Modeling the structural evolution of carbide-derived carbons using quenched molecular dynamics.” *Carbon* 48.4 (2010), pp. 1116–1123.

[85] C. Merlet, M. Salanne, and B. Rotenberg. “New Coarse-Grained Models of Imidazolium Ionic Liquids for Bulk and Interfacial Molecular Simulations.” *The Journal of Physical Chemistry C* 116.14 (2012), pp. 7687–7693.

[86] C. Merlet, M. Salanne, B. Rotenberg, and P. A. Madden. “Influence of solvation on the structural and capacitive properties of electrical double layer capacitors.” *Electrochimica Acta* 101 (2013), pp. 262–271.

[87] H. C. Andersen. “Rattle: A ”Velocity” Version of the Shake Algorithm for Molecular Dynamics Calculations.” *Journal of Computational Physics* 51 (1983), pp. 24–34.

[88] J. I. Siepmann and M. Sprik. “Influence of surface topology and electrostatic potential on water/electrode systems.” *The Journal of Chemical Physics* 102.1 (1995), pp. 511–524.

[89] S. K. Reed, O. J. Lanning, and P. A. Madden. “Electrochemical interface between an ionic liquid and a model metallic electrode.” *The Journal of Chemical Physics* 126.8 (2007), p. 084704.

[90] J. Reed, B. Mishra, B. Pittenger, S. Magonov, J. Troke, M. A. Teitell, and J. K. Gimzewski. “Single molecule transcription profiling with AFM.” *Nanotechnology* 18.044032 (2007), p. 044032.

[91] T. R. Gingrich and M. Wilson. “On the Ewald summation of Gaussian charges for the simulation of metallic surfaces.” *Chemical Physics Letters* 500.1-3 (2010), pp. 178–183.

[92] C. Portet, P. L. Taberna, P. Simon, E. Flahaut, and C. Laberty-Robert. “High power density electrodes for Carbon supercapacitor applications.” *Electrochimica Acta* 50.20 (2005), pp. 4174–4181.

[93] J. Vatamanu, L. Xing, W. Li, and D. Bedrov. “Influence of temperature on the capacitance of ionic liquid electrolytes on charged surfaces.” *Physical Chemistry Chemical Physics : PCCP* 16 (2014), pp. 5174–82.

[94] L. Feng, J. Yang, J. Zhao, D. Wang, K. Koynov, and H.-J. Butt. “Fluorescence correlation spectroscopy of repulsive systems: Theory, simulation, and experiment.” *The Journal of Chemical Physics* 138.21, 214902 (2013).

[95] A. A. K. R. Qiao. “Three-Dimensional Double Layers.” *The Journal of Physical Chemistry C* 118.32 (2014), pp. 18285–18290.

[96] G.-H. Min, T. Yim, H. Yeong Lee, D. Huh, E. Lee, J. Mun, S. M. Oh, and Y. Kim. *Synthesis and Properties of Ionic Liquids: Imidazolium Tetrafluoroborates with Unsaturated Side Chains*. Vol. 37. 2006.

[97] V. Ruiz, C. Blanco, E. Raymundo-Piñero, V. Khomenko, F. Béguin, and R. Santamaría. "Effects of thermal treatment of activated carbon on the electrochemical behaviour in supercapacitors." *Electrochimica Acta* 52.15 (2007), pp. 4969–4973.

[98] J. Gamby, P. L. Taberna, P. Simon, J. F. Fauvarque, and M. Chesneau. "Studies and characterisations of various activated carbons used for carbon/carbon supercapacitors." *Journal of Power Sources* 101 (2001), pp. 109–116.

[99] M. Armand, F. Endres, D. R. MacFarlane, H. Ohno, and B. Scrosati. "Ionic-liquid materials for the electrochemical challenges of the future." *Nature Materials* 8 (2009), pp. 621–629.

[100] A. Krause and A. Balducci. "High voltage electrochemical double layer capacitor containing mixtures of ionic liquids and organic carbonate as electrolytes." *Electrochemistry Communications* 13.8 (2011), pp. 814–817.

[101] S. Pohlmann, T. Olyschläger, P. Goodrich, J. A. Vicente, J. Jacquemin, and A. Balducci. "Mixtures of azepanium based ionic liquids and propylene carbonate as high voltage electrolytes for supercapacitors." *Electrochimica Acta* 153 (2015), pp. 426–432.

[102] J. Li, X. Gong, H. Lu, D. Li, H. Fang, and R. Zhou. "Electrostatic gating of a nanometer water channel." *Proceedings of the National Academy of Sciences* 104.10 (2007), p. 3687.

[103] B. Dyatkin, O. G. B. Malinovskiy, YuliyaZozulya, P. Simon, and Y. Gogotsi. "High capacitance of coarse-grained carbide derived carbon electrodes." *Journal of Power Sources* 306 (2016), pp. 32–41.

[104] T.-C. Lee, M. Alarcòn-Correa, C. Miksch, K. Hahn, J. G. Gibbs, and P. Fischer. "Self-propelling nanomotors in the presence of strong Brownian forces." *Nano Letters* 14.5 (2014), pp. 2407–2412.

[105] W. Schmickler. "A simple model for charge storage in a nanotube." *Electrochimica Acta* 173 (2015), pp. 91–95.

[106] C. C. Rochester, S. Kondrat, G. Pruessner, and A. A. Kornyshev. "Charging ultra-nanoporous electrodes with size-asymmetric ions assisted by apolar solvent." *Journal of Physical Chemistry C* 120 (2016), p. 16042.

[107] K. Kiyohara and K. Asaka. "Monte Carlo Simulation of Porous Electrodes in the Constant Voltage Ensemble." *Journal of Physical Chemistry C* 111 (2007), pp. 15903–15909.

[108] K. Kiyohara, T. Sugino, and K. Asaka. "Electrolytes in porous electrodes: Effects of the pore size and the dielectric constant of the medium." *Journal of Chemical Physics* 132 (2010), p. 144705.

[109] K. Kiyohara, T. Sugino, and K. Asaka. "Phase transition in porous electrodes." *Journal of Chemical Physics* 134 (2011), p. 154710.

[110] M. Dudka, S. Kondrat, A. Kornyshev, and G. Oshanin. "Phase behaviour and structure of a superionic liquid in nonpolarized nanoconfinement." *Journal of Physics: Condensed Matter* 28 (2016), p. 464007.

[111] C. Geuzaine and J.-F. Remacle. "Gmsh: A 3-D finite element mesh generator with built-in pre- and post-processing facilities." *International Journal for Numerical Methods in Engineering* 79.11 (2009), pp. 1309–1331.

[112] S. Rebay. "Efficient Unstructured Mesh Generation by Means of Delaunay Triangulation and Bowyer-Watson Algorithm." *Journal of Computational Physics* 106.1 (1993), pp. 125–138.

[113] S. Fuhrmann. "Volume data generation from triangle meshes using the signed distance function." MA thesis. Darmstadt University of Technology, 2007.

[114] M. Oschatz, P. Pre, S. Doröfler, W. Nickel, P. Beaunier, J.-N. Rouzaud, C. Fischer, E. Brunner, and S. Kaskel. "Nanostructure characterization of carbide-derived carbons by morphological analysis of transmission electron microscopy images combined with physisorption and Raman spectroscopy." *Carbon* 105 (2016), pp. 314–322.

[115] M. G. Martin. "MCCCS Towhee: a tool for Monte Carlo molecular simulation." *Molecular Simulation* 39.14-15 (2013), pp. 1212–1222.

[116] B. Widom. "Some topics in the theory of fluids." *Journal of Chemical Physics* 39 (1963), pp. 2802–2812.

[117] J. Jiang, D. Cao, D. Henderson, and J. Wu. "Revisiting density functionals for the primitive model of electric double layers." *The Journal of Chemical Physics* 140.4 (2014), p. 044714.

[118] S. Tyagi, A. Arnold, and C. Holm. "ICMMM2D: An accurate method to include planar dielectric interfaces via image charge summation." *Journal of Chemical Physics* 127 (2007), p. 154723.

[119] S. Kondrat and A. Kornyshev. "Pressing a spring: What does it take to maximize the energy storage in nanoporous supercapacitors?" *Nanoscale Horizons* 1 (2016), pp. 45–52.

[120] A. A. Lee, D. Vella, A. Goriely, and S. Kondrat. "Capacitance-Power-Hysteresis Trilemma in Nanoporous Supercapacitors." *Physical Review X* 6 (2016), p. 021034.

[121] M. V. Fedorov and A. A. Kornyshev. "Ionic Liquid Near a Charged Wall: Structure and Capacitance of Electrical Double Layer." *The Journal of Physical Chemistry B* 112.38 (2008), pp. 11868–11872.

[122] M. V. Fedorov and A. Kornyshev. "Towards understanding the structure and capacitance of electrical double layer in ionic liquids." *Electrochimica Acta* 53 (2008), pp. 6835–6840.

[123] K. Breitsprecher, M. Abele, S. Kondrat, and C. Holm. "The effect of finite pore length on ion structure and charging." *The Journal of Chemical Physics* (2017).

[124] W. H. Press. *Numerical recipes: the art of scientific computing*. Cambridge Univ Pr, 2007.

[125] Y. He, J. Huang, B. G. Sumpter, A. A. Kornyshev, and R. Qiao. "Dynamic Charge Storage in Ionic Liquids-Filled Nanopores: Insight from a Computational Cyclic Voltammetry Study." *Journal of Physical Chemistry Letters* 6 (2015), p. 22.

[126] A. J. Pak and G. S. Hwang. "Charging Rate Dependence of Ion Migration and Stagnation in Ionic-Liquid-Filled Carbon Nanopores." *Journal of Physical Chemistry C* 120 (2016), p. 24560.

[127] S. Kondrat, P. Wu, R. Qiao, and A. A. Kornyshev. "Accelerating charging dynamics in subnanometre pores." *Nature materials* 13.4 (2014), pp. 387–393.

[128] R. Mysyk, E. Raymundo-Piñero, and F. Béguin. "Saturation of subnanometer pores in an electric double-layer capacitor." *Electrochemistry Communications* 11 (2009), pp. 554–556.

[129] S. Kondrat and A. Kornyshev. "Charging Dynamics and Optimization of Nanoporous Supercapacitors." *Journal of Physical Chemistry C* 117 (2013), pp. 12399–12406.

[130] P. L. Taberna, P. Simon, and J. F. Fauvarque. "Electrochemical Characteristics and Impedance Spectroscopy Studies of Carbon-Carbon Supercapacitors." *Journal of the Electrochemical Society* 150 (2003), A292–A300.

[131] S. Kondrat and A. A. Kornyshev. "Pressing a spring: what does it take to maximize the energy storage in nanoporous supercapacitors?" *Nanoscale Horizons* 1.1 (2016), pp. 45–52.

[132] Y. He, R. Qiao, J. Vatamanu, O. Borodin, D. Bedrov, J. Huang, and B. G. Sumpter. "Importance of Ion Packing on the Dynamics of Ionic Liquids during Micropore Charging." *The journal of physical chemistry letters* 7.1 (2015), pp. 36–42.

[133] O. Y. Fajardo, F. Bresme, A. A. Kornyshev, and M. Urbakh. "Electrotunable Friction with Ionic Liquid Lubricants: How Important Is the Molecular Structure of the Ions?" *The Journal of Physical Chemistry Letters* 6.20 (2015), pp. 3998–4004.

[134] D. Roy and M. Maroncelli. "Simulations of Solvation and Solvation Dynamics in an Idealized Ionic Liquid Model." *Journal of Physical Chemistry B* 116.20 (2012), pp. 5951–5970.

[135] C. Péan, B. Rotenberg, P. Simon, and M. Salanne. "Multi-scale modelling of supercapacitors: From molecular simulations to a transmission line model." *Journal of Power Sources* 326 (2016), pp. 680–685.

[136] S. E. Feicht, A. E. Frankel, and A. S. Khair. "Discharging Dynamics in an Electrolytic Cell." *Physical Review E* 94.1 (2016).

[137] A. A. Lee, S. Kondrat, and A. A. Kornyshev. "Charge Storage in Conducting Cylindrical Nanopores." *Physical Review Letters* 113 (2014), p. 048701.

[138] J. J. Yoo, K. Balakrishnan, J. S. Huang, V. Meunier, B. G. Sumpter, A. Srivastava, M. Conway, A. L. M. Reddy, J. Yu, R. Vajtai, and P. M. Ajayan. "Ultrathin Planar Graphene Supercapacitors." *Nano Letters* 11 (2011), pp. 1423–1427.

[139] M. R. Lukatskaya, O. Mashtalir, C. E. Ren, Y. Agnese, P. Rozier, P. L. Taberna, M. Naguib, P. Simon, M. W. Barsoum, and Y. Gogotsi. "Cation Intercalation and High Volumetric Capacitance of Two-Dimensional Titanium Carbide." *Science* 341 (2013), p. 1502.

# Appendix A: Acknowledgements

I thank all the institutions that supported this work, foremost the University of Stuttgart and the Institute of Computational Physics. Also, I acknowledge the cluster of excellence "Simulation Technology" and the SFB 716 for financial support. Further, I am grateful for the STSM grant via the EU COST action (CM1206), which partially funded my stay in Paris.

I'm thankful for all the wonderful people I've had the honor to get to know during my physics studies and my time as a PhD student. All the support, ideas, discussions and spent time really shaped me as a scientist and person. Thank you Damir, Thorsten, Valentin, Michael H., Tobi, Kai, Jonas, Tilmann, David, Frank U., Hannes, Flo W., Yacine, Clarisse, Patrick, Anand, Jens, Iris, Georg, Julian, Julia, Ashreyaj, Frank H., Maria, Ganesh, Ewa, Bibek, Henriette, Meike, Rudolf, Swantje, Stefan, Michael K., Maofeng and Kerstin.

Special thanks are given to my co-authors and project partners:
Thank you Slava, Ryan, Mathieu, Kai, Manuel and Peter for all your help!

My grateful thanks also go to Prof. Christian Holm for being the supervisor a PhD student could wish for!

Finally, my love goes to my family, Meinhard, Christine, Heinrich and Jenny. Thank you for your endless support and encouragement!

# Appendix B: Declaration

I hereby declare that I have independently created this dissertation. Any information, graphics and data taken from external sources are referenced.

Konrad Breitsprecher